THÈSE

Présentée à

Université Lille 1 - Sciences et Technologies
(Ecole Doctorale des Sciences de la Matière, du Rayonnement et de l'Environnement)
East China Normal University

pour l'obtention du

Docteur

(Discipline : Molécules et Matière Condensée)

par

Yixuan LI

Développement de nouvelles méthodes de RMN des solides : nouvelles séquences d'impulsion pour les expériences de corrélation hétéronucléaires et traitement par covariance des expériences homonucléaires
(New pulse sequences for heteronuclear experiments and covariance for homonuclear experiments in Solid-State NMR)

Soutenance prévue le 22 Août 2015

Composition du Jury :

Directeur de Thèse :
  Jean-Paul Amoureux, Professeur, Université Lille 1
  Qun Chen, Professeur, East China Normal University
  Olivier Lafon, Professeur, Université Lille 1
  Bingwen Hu, Professeur, East China Normal University

Rapporteurs :
  Charlotte Martineau, Maître de Conférences, Université de Versailles, St Quentin en Yvelines
  Ping Zhou, Professeur, Fudan University
Examinateur :
  Francis Taulelle, Directeur de Recherche CNRS, Université de Versailles, St Quentin en Yvelines

Acknowledgements

Contents

ABSTRACT

The focus of this thesis is on the development of Solid-State Nuclear Magnetic Resonance (SS-NMR), including new pulse sequences for heteronuclear experiments and new data processing methods for homonuclear experiments.

In chapter 1, we briefly review the history of NMR. The first exploration has been done by Bloch and Purcell in 1945. Within several years, many techniques have been introduced. Recently, the high magnetic fields, fast spinning speeds and advanced pulse sequences are all widely developed and used. SS-NMR has been a powerful tool for providing deep insights into the structure and dynamics of many systems in the area of chemistry, biology, geology, and materials science.

Second, we review the Hamiltonians and their manipulations of nuclear spins. The appearance of NMR spectra is determined by various interactions from the external apparatus and from the sample itself, called external spin interactions and internal spin interactions, respectively. The external spin interactions include static magnetic field, rf oscillating field and magnetic field gradient. The internal spin interactions include chemical shift, dipole-dipole couplings J-couplings and quadrupolar couplings (for spin> 1/2 nuclei). We show the explanation and equation for each interaction.

Next, a useful technique, population transfer (PT), is represented. Due to the fact that a large proportion of NMR-active nuclei are quadrupolar nuclei (spin> 1/2), the sensitivity remains one of the central problems in NMR spectroscopy. We introduce three different methods, WURST (Wideband, Uniform rate, Smooth Truncation), DFS (double frequency sweep) and HS (Hyperbolic secant), which have already been designed to transfer magnetization from the STs (satellite transitions) to the CT (central transition) in order to enhance the polarization of the CT. There are two general mechanisms describing this process, one is ST saturation which is easier to accomplish, equalizing the populations of two adjacent energy levels. By saturating

the STs, a maximum theoretical enhancement of the CT of I+1/2 can be achieved, where I is the nuclear spin number. The other one is ST inversion, the magnetization from all transitions can be transferred to the CT by a series of ST inversions. For half-integer quadrupoles with spin numbers of 5/2 or greater, this ST inversion should start from the outer STs to the inner STs, to achieve the maximum 2I enhancement.

At last, we review two NMR spectra: fourier transformation two-dimensional (FT2D) spectroscopy and two-dimensional covariance (COV2D) spectroscopy. FT2D spectrum transforms signal $s(t_1,t_2)$ in time domain to $S(\Omega_1,\Omega_2)$ in frequency domain using FT respect to t_2 first and t_1 next. COV2D spectrums transforms signal with FT respect to t_2 first, and then computing with covariance analysis.

In chapter 2, for heteronuclear SS-NMR correlation experiments, we propose a simple and robust strategy to accelerate the rate of coherence transfer by manipulating the population of STs, and enhance the sensitivity of HMQC (Heteronuclear Multiple-Quantum Correlation) experiments with indirect detection of the quadrupolar nucleus, called PT-HMQC (Population transfer HMQC). We analyze this simple and robust strategy in details by combining theory, simulations and experiments.

First, we derive the analytical expression of J-HMQC (J-midiated HMQC) signal when the S isotope is a half integer quadrupolar nucleus, for the sake of simplicity, the expression is derived for an isolated 1/2-3/2 (I-S) spin-pair. We can achieve $I_y E_C \cos(\pi J \tau_{mix}) - 2I_x C_z \sin(\pi J \tau_{mix}) + I_y E_T \cos(3\pi J \tau_{mix}) - 2I_x T_z \sin(3\pi J \tau_{mix})$ after the first τ_{mix} delay, in which C_z and T_z are the longitudinal fictitious operators associated with the CT and the triple-quantum coherence of $S = 3/2$ spin, respectively. In the case of CT-selective excitation, only the second term is converted into heteronuclear multiple-quantum coherences, with an optimal delay of $\tau_{mix} = 1/(2J)$. Our strategy is to make the fourth term also participates in the t_1 evolution to accelerate the magnetization transfer in the HMQC experiment. The simplest method is to convert

the I_xT_z operator into I_xC_z before the first CT-selective $\pi/2$ pulse on S spins by manipulating the populations of the STs during or just after the first delay τ_{mix}. Then, similar conversion can also occur during or just before the second τ_{mix} delay to convert I_xC_z back to I_xT_z after the second CT-selective $\pi/2$ pulse. This approach is referred to as PT-HMQC. After simulations, we find continuous saturation during t_{mix} delays is the best way. This process can in practice be achieved by applying a series of adjacent adiabatic pulses, such as DFS, HS or WURST. Since they follows the same principles used to enhance the CT signal of quadrupolar nuclei, we use WURST scheme to perform this saturation with PT-HMQC in this chapter.

Then we carry out numerical simulations for ^{23}Na-^{31}P (3/2-1/2) and ^{27}Al-^{31}P (5/2-1/2) spin-pair. The results show the optimal mixing time tends toward our analytical result of $1/[2(S+1/2)J]$, and when considering the PT-J-HMQC efficiency versus the offset of WURST, this curve exhibits a profile analogue to that of satellite transition MAS spectrum, except for the frequency region with small offset irradiation where there is a severe interference between the WURST irradiation and the CT population. And the efficiency is slightly smaller than with J-HMQC. But if we take into account the relaxation losses, PT-J-HMQC is more efficient than J-HMQC, and the gain increases with decreasing T_{2I}' value.

Next NMR experiments are performed: ^{31}P-$\{^{27}$Al$\}$ PT-J-HMQC experiments on AlPO$_4$-HDA sample, ^{27}Al-$\{^{17}$O$\}$ PT-J-HMQC for two half-integer quadrupolar species on Al$_2$O$_3$ sample and ^{31}P-$\{^{27}$Al$\}$ PT-D-HMQC on AlPO4-14 sample. All the experiments prove that the PT-HMQC method can accelerate the rate of coherence transfer by manipulating the population of STs, and enhance the sensitivity.

However, the limitation of PT-J-HMQC using WURST shape pulse is the dependence of offset. So we try double sweeps pulse DFS and DWURST (Double WURST). The simulation results show a small offset needs small rf-amplitude, and a large offset needs large rf-amplitude. Hence, we introduce new methods using

quadruple sweeps: QFS (quadruple frequency sweep) and QWURST (quadruple WURST). Simulation results show the efficiencies of quadruple sweeps pulses are more stable, with slightly dependence on offset than those of double sweeps pulse (DFS, DWURST). The ^{31}P-{^{27}Al} PT-J-HMQC experiments on Berlinite and $AlPO_4$-14 samples show the quadruple sweeps are more robust for small C_Q, and above all, QFS is the most stable and efficient pulse. We believe that these new approaches will be very beneficial for a wide range of organic, inorganic and even biological materials containing half-integer quadrupolar nuclei, and will provide detailed insight into their structure-property relationship.

In chapter 3, we introduce new data processing methods for homonuclear experiments. We combine COV2D spectroscopy with non-uniform continuous acquisition (NUCA) scheme. We use two schemes linear profile (L_k) and Gaussian profile (G_k). With numerical NMR experiments, we observe Gaussian-FT2D profile introduces larger increments in both signals and linewidths than the linear-FT2D. But the increase in S/N of NUCA-FT2D is lower than that in signals. On the other hand, NUCA-COV2D (covariance processing with a non-uniform continuous acquisition scheme) is beneficial for producing ^{13}C-^{13}C correlation spectra with both good resolution and S/N. UCA-COV2D (covariance processing with uniform continuous acquisition scheme) scheme will generate the spectra with lower S/N, and NUCA-FT2D scheme will produce those with lower resolution. With the Gaussian profile and COV2D method, we were able to reduce the number of increments in t_1 by a factor of 1.5~3. The S/N was also increased by another factor of 1.5, which further saves experimental time by a factor of 2, without sacrificing any resolution in the indirect dimension. Furthermore, for amplitude-modulated spectra, the total experimental time of COV2D is also reduced by an additional factor of 2, since COV2D data treatment does not require States or TPPI acquisition to obtain the correct resonance frequencies along F_1 dimension. Covariance NMR has been shown

to work for 4D spectra for resolution enhancement. As solid state NMR is nowadays applied to biomolecules of ever-increasing size, such advances might become especially vital to analyze higher-dimensional NMR spectra.

Next we combine COV2D spectroscopy with various sampling schemes, such as NUS (non-uniform sampling) and CUO (t_1 cut-off), and Gaussian accumulation and constant square profile can also be used together.

The experimental results show, as a general rule, reduced CUO sampling scheme always provides identical or better $S/N_{\text{peak-ridge}}$ and $S/N_{\text{peak-free}}$ ratios than NUS, this observation demonstrates that the data points for short t_1 values are the most informative for covariance processing, without loss of resolution. CUO sampling makes the covariance easy to use in practice, since the number of t_1 points can easily be optimized to obtain the desired resolution along F_1. This resolution must be the best in the case of very crowded 1D spectrum (e.g. proteins), whereas it can be decreased to maximize the S/N ratio in the case of resolved 1D spectrum.

We demonstrate that these two restricted sampling schemes can also be combined in covariance spectroscopy with weighted acquisition strategy with different accumulation profiles to further enhance the S/N of NMR spectra. We show that, with respect to the constant accumulation profile, a better S/N ratio is obtained with the Gaussian accumulation profile.

We also demonstrate that the CUO sampling with sampling-saving factor of $\xi \approx$ 0.3, simultaneously with the Gaussian-50 accumulation profile, leads to good S/N, enhanced by a factor of 2.3 with respect to the conventional FT2D method, together with good resolution. Therefore, with the Gaussian profile and CUO-COV2D method, we were able to reduce the number of increments in t_1 by a factor of ca. 6~12. Here we should emphasize that this argument is only valid with exponentially decaying 2D signals, and not in the case of sine/cosine modulated or constant-time signals. Overall, this combination of Gaussian accumulation profile and CUO sampling in covariance

spectroscopy should become valuable in applications for the sensitivity-limited solid state NMR experiments.

Chapter 1: Introduction

1.1. History of Solid State NMR

In 1945, Purcell detected weak radio-frequency signals generated by the nuclei of atoms in ordinary matter. Almost at the same time, Bloch performed a different experiment in which they observed radio signals from the atomic nuclei in water. These two experiments were the first exploration of the field we now know as nuclear magnetic resonance (NMR)[1].

In 1966, the first one-dimensional (1D) spectra using pulse excitation and data processing with Fourier transform (FT) was obtained by Ernst and Anderson[2]. In 1975 Jeener and Ernst introduced multidimensional FT NMR spectroscopy[3]. These developments allowed obtaining well resolved and structurally informative ^{1}H and ^{13}C spectra from solutions at modest magnetic field strengths.

However, in 1950s and 1960s, the use of NMR spectroscopy for solids was limited by the poor resolution of NMR spectra, since the anisotropic nuclear interactions are strongly depend on the molecular orientations. These anisotropic interactions can be averaged by the fast Brownian motions of the molecules in solution, but not in solids, and then the various anisotropic interactions makes the spectra too broad to provide useful information. Furthermore, numerous isotopes are half-integer spin quadrupolar nuclei. The second-order quadrupolar broadening is inversely proportional to the strength of the magnetic fields and hence high-resolution solid-state NMR spectra of quadrupolar nuclei need high magnetic field. But for a long time, the magnetic field was produced by resistive coils, and limited to about 2T. The requirement of high field strengths has lead to the development of superconducting magnets. Now, the magnetic field arrives at 23.5 T. However, these fields are very difficult to sweep, and the pulse excitation techniques have thus to be used mandatory. Recently, the superconducting magnetic field is kept constant and a

radio-frequency (rf) irradiation at the Larmor frequency of the observed nuclei is applied as a sequence of rf pulses.

The most important improvement for SS-NMR is in 1959. Andrew[4] and Lowe[5] advised that some factors in solids leading to linewidths broadening could be minimized using rapidly rotating for the sample at a particular angle. In 1960, Gorter suggested "Magic Angle Spinning" as the name of this new method. The MAS technique rotates the nucleus rapidly in the real space and imposes an average axial symmetry in an otherwise asymmetric environment. To average some interactions, such as chemical shift anisotropy and dipole-dipole coupling, we don't need to move the sample over a whole sphere, we can just impose a cubic symmetry, and this is what MAS does.

In 1970s, MAS spinning speed rates could arrive at 2 kHz and be successfully applied to inorganic substances[6,7]. At the same time, Multiple-Pulse (MP) NMR pulse sequence[8] came, and it can enhance the resolution. These MP methods are used for both heteronuclear and homonuclear decoupling. They can provide effective suppressions on dipolar and quadrupolar broadening, but not on chemical shift anisotropic broadening. Presently, these heteronuclear decoupling methods combined with MAS, are usually able to eliminates most part of anisotropic broadening and leads to the highly resolved solid-state NMR spectra.

There is still a very important limitation for SS-NMR: the weak sensitivity. And then Cross-Polarization (CP) came in 1962, by Hartman and Hahn[9]. This technique is used to make the nuclear polarization transfer from the abundant spins with large gyromagnetic ratio γ_I and short longitudinal relaxation time T_{1I} to the dilute spins with small γ_s and long T_{1s}, leading to the enhancement of the magnetization of the dilute spins and the reduction of the experimental time. The ^{1}H-^{13}C CP has been widely used.

With these developments, the high-resolution SS-NMR spectra could be acquired.

The NMR observation of other nuclei, such as quadrupolar nuclei: ^{27}Al, ^{23}Na and ^{11}B, was also very attractive. But MAS is usually not sufficient since the 2nd-order quadrupolar interaction couldn't be averaged to zero. New strategies were developed to increase the resolution of quadrupolar NMR spectra including: satellite transition spectroscopy determining the quadrupole and chemical shift parameters[10], and quadrupolar phase alternated sideband suppression (QPASS) suppressing the overlapping spinning sidebands[11]. Dipolar interactions between spin 1/2 and quadrupolar nuclei have been measured under MAS using CP, Rotational Echo DOuble Resonance (REDOR)[12], Transferred Echo DOuble Resonance (TEDOR)[13], TRAnsfer of Populations DOuble Resonance (TRAPDOR)[14], Rotational Echo Adiabatic Passage DOuble Resonance (REAPDOR)[15] and Resonance Echo Saturation Pulse DOuble Resonance (RESPDOR)[16]. Methods to eliminate the second-order quadrupolar broadening also have been developed, including Double Rotation (DOR)[17], Dynamic Angle Spining (DAS)[18], Multiple-Quantum MAS (MQMAS) and satellite transition MAS (STMAS)[19].

In recent years, the high magnetic fields, fast spinning speeds and advanced pulse sequences are all been widely developed and used. But the sensitivity is still lower by two or three orders magnitude than that of solution-state NMR.

1.2. Hamiltonians and their manipulations

The nuclear spins are not alone. A real sample contains an astronomical number of nuclei and electrons. In principle, the Schrodinger equation should involve the motions of all the nuclei and electrons, and the Hamiltonian operator involves the interactions between all of them. However, since the electronic motions are very rapid, the nuclear spins only affect by a time average of the fields, and the nuclear spin energies are also too small to affect the motions of electrons in the molecules or the motions of the molecule themselves. Then the equation can be much simpler:

$$\frac{d}{dt}\left|\psi_{spin}(t)\right\rangle = -i\widehat{H}_{spin}\left|\psi_{spin}(t)\right\rangle \tag{1}$$

in which $\left|\psi_{spin}(t)\right\rangle$ is the spin state of the nuclei, $\hat{H}_{spin}$ is the nuclear spin Hamiltonian. The nuclear spin Hamiltonian contains only the terms that depend on the directions of the nuclear spin polarizations. The magnetic and electrical influences of the rapidly moving electrons are blurred out, so one can only obtain the average. And the spin Hamiltonian $\hat{H}_{spin}$ contains these 'blurred-out' electronic influences. From now on, the Hamiltonian operator $\hat{H}$ is taken into the following discussions of the nuclear spin interactions.

The appearance of NMR spectra is determined by various interactions from the external apparatus and from the sample itself. The first case is the external spin interactions. For the second case, the term internal spin interactions are used. So the Hamiltonian of all spin interactions can be written as:

$$\widehat{H} = \widehat{H}_{Ext} + \widehat{H}_{Int} \tag{2}$$

in which $\hat{H}_{Ext}$ and $\hat{H}_{Int}$ are the spin Hamiltonians for the external and internal interactions, respectively. These Hamiltonians has the form:

$$\widehat{H}_{Ext} = \widehat{H}_{stat} + \widehat{H}_{RF}(t) + \widehat{H}_{RF}(r,t) \tag{3}$$

$$\widehat{H}_{Int} = \widehat{H}_{CS} + \widehat{H}_{D}(t) + \widehat{H}_{J}(t) + \widehat{H}_{Q} \tag{4}$$

1.2.1 The external spin interactions

The external spin interactions are purely magnetic, except in exotic circumstances. For almost all cases, the applied magnetic fields of various types are used to manipulate the nuclear spins. The main superconducting solenoid provides a very strong, homogeneous and static magnetic field, called B^0. The radio-frequency coil in the probe generates a rf oscillating field, $B_{RF}(t)$. The gradient coils provide a magnetic field gradient, called $B_{grad}(r,t)$. This filed is much weaker than B^0, which is dependent on the position coordinate r, and may also have controlled time dependence.

In the laboratory frame, the spin halmitonian of the nuclear Zeeman interaction of spin I is written as:

$$\hat{H}_{stat,I} = -\gamma_I B^0 \hat{I}_z \tag{5}$$

γ_I is the gyromagnetic ratio and $-\gamma_I B^0$ is identified as the Larmor frequency of spin I. The expression of $\hat{H}_{RF}(t)$ is given by:

$$\hat{H}_{RF,I}(t) = -\frac{1}{2}\gamma_I B_{RF} \sin\theta_{RF} \left\{\cos(\omega_{ref}t + \phi)\hat{I}_x + \sin(\omega_{ref}t + \phi)\hat{I}_y\right\} \tag{6}$$

θ_{RF} is the tilt angle between B^0 and $B_{RF}(t)$. The interaction with the field gradients is written as:

$$\hat{H}_{grad,I}(r,t) = -\gamma_I B_{grad}(r,t)\frac{r}{r_{max}}\hat{I}_z \tag{7}$$

r is the spatial position (x, y, z) of spin I , r_{max} is the maximum value of r along the direction of B_{grad}.

1.2.2 The internal spin interactions

The nuclei experience magnetic and electric fields originating from the sample itself. The internal spin Hamiltonian, $\hat{H}_{Int}$, includes these interactions.

Chemical shift terms represent the indirect magnetic interaction of the external magnetic field and the nuclear spins, through the involvement of the electrons, under 1st-order approximation, the Hamiltonian of chemical shift interactions is:

$$\hat{H}_{CS,I}^{(1)} = -\gamma_I B^0 \hat{I}_z \left\{\sigma_{iso} + \frac{1}{2}\sigma_{CSA}[3\cos^2\beta^{CSA} - 1] + \eta_{CSA}\sin^2\beta^{CSA}\cos 2\gamma^{CSA}]\right\} \tag{8}$$

where the β_{CSA} and γ_{CSA} are the polar angles specifying the orientation of the principal axis system of the chemical shift tensor in the laboratory frame. Similar definitions (β^D, γ^D; β^J, γ^J; β^Q, γ^Q) are also used in dipolar and quadurpolar cases (Fig.1).

Dipole-dipole couplings represent the direct magnetic interactions of nuclear spins with each other. The magnitude of the dipolar interaction between two spins i and j is the dipole-dipole coupling constant, b_{ij} in rad.s-1:

$$b_{ij} = -\frac{\mu_0}{4\pi}\frac{\gamma_i\gamma_j\hbar}{d_{ij}^3} \tag{8}$$

in whici d_{ij} is the distance between two spins. This dipole-dipole coupling term is usually

used for molecular structral studies and to probe the through-space heteronuclear proximities, because it just depends on the known physical constants and the inverse cube of the internuclear distance. Since NMR is often performed in high magnetic field, the approximation will lead to:

$$(9)$$

for homonuclear spins, and

$$\widehat{H}_D^{(1)}(hetero) = -\frac{\mu_0}{4\pi}\frac{\gamma_i\gamma_j\hbar}{d_{ij}^3}(3\cos^2\beta_{ij}^D - 1)\hat{I}_{z,i}\hat{S}_{z,i} \tag{10}$$

for heteronuclear spins.
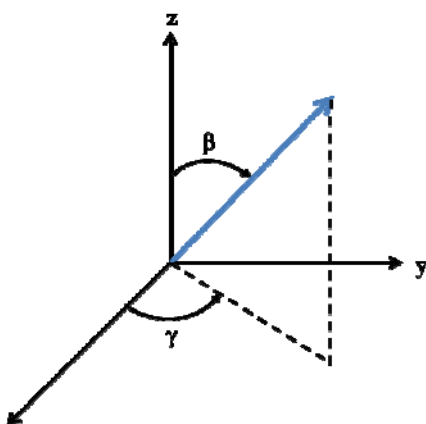
Fig.1 Definition of the Euler angles β and γ in terms of polar angles specifying the orientation of principal axis system in the laboratory frame.

J-couplings represent the indirect magnetic interactions of nuclear spins with each other, through the involvement of the electrons. J-coupling occurs between nuclei connected via a small number of chemical bonds. This information is quite useful for the assignment of the molecular structure. The Hamiltonian of can be given by:

$$\widehat{H}_J^{(1)}(homo) = J_{iso}\hat{I}_i \cdot \hat{I}_j + \frac{1}{4}J_{aniso,ij}(3\cos^2\beta_{ij}^J - 1)(3\hat{I}_{z,i}\hat{I}_{z,i} - \hat{I}_i\hat{I}_j) \tag{11}$$

for homonuclear spins, and

$$\widehat{H}_J^{(1)}(hetero) = J_{iso,ij} + \frac{1}{2}J_{aniso,ij}(3\cos^2\beta_{ij}^J - 1)\hat{I}_{z,i}\hat{I}_{z,j}) \tag{12}$$

for heteronuclear spins.

Quadrupolar couplings represent the electric interactions of spin> 1/2 nuclei

with the surrounding electric fields. The electric quadrupole moment interacts with the electric field gradients generated by the non-spherical electron distribution. In SS-NMR, the quadrupolar coupling constant C_Q is defined as:

$$C_Q = \frac{e^2 q}{h} Q \tag{13}$$

If the quadrupolar interaction is much smaller than Zeeman interaction, under 1st-order approximation, the Hamiltonian can be written as:

$$\widehat{H}_Q^{(1)} = \frac{1}{3} \omega_Q (3\hat{I}_z^2 - \hat{I}) \tag{14}$$

in which,

$$\omega_Q = \frac{1}{3} \omega_Q^{(1)} [(3\cos^2 \beta^Q - 1] + \eta_Q \sin^2 \beta^Q \cos 2\gamma^Q] \tag{15}$$

$$\omega_Q^{(1)} = \frac{3\pi C_Q}{2I(2I-1)} \tag{16}$$

η_Q is the asymmetry parameter, ω_Q is the 1st-order quadrupolar coupling. However, in most real samples, the strength of this quadrupolar interaction is in the order of 0.01-10 MHz. So it is necessary to include more than one term in the quadrupolar Hamiltonian expression (Fig.2).

$$\widehat{H}_Q = \widehat{H}_Q^{(1)} + \widehat{H}_Q^{(2)} + ... \tag{17}$$

Fig.2 Energy level diagram of a spin-3/2 system showing the Zeeman interaction and the 1st- and 2nd-order quadrupolar perturbation of energy levels.

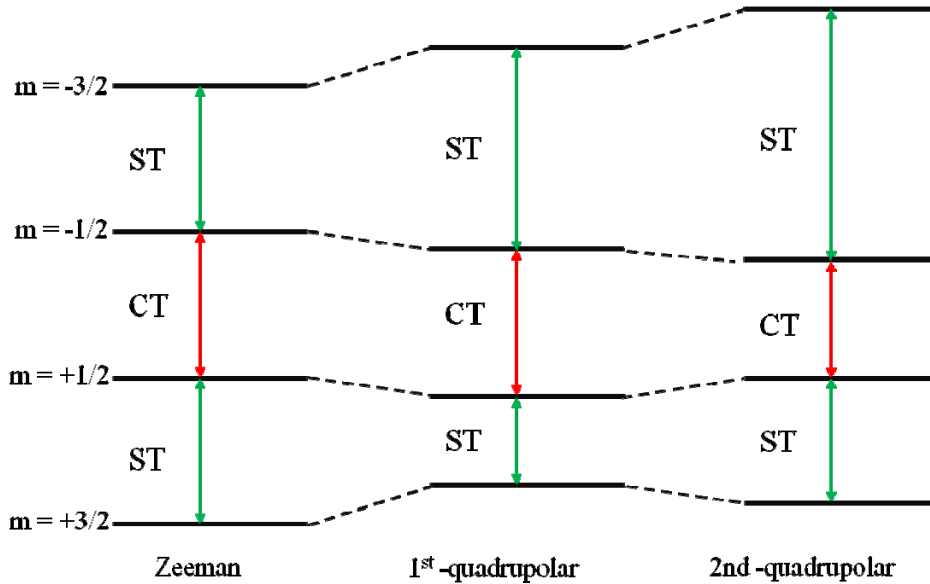If we calculate the second-order shifts in energy levels which decreases at a higher magnetic field, in particular, for the central transition (CT), when η_Q is 0, the frequency splitting is:

$$\omega_Q^{(2)} = \frac{1}{16\omega_0}(\omega_Q^{(1)})(\hat{I}^2 - \frac{3}{4})(\cos^2 \beta^Q - 1](9\cos^2 \beta^Q - 1)] \qquad (18)$$

The 1st-order interaction is proportional to C_Q, while the 2nd-order interaction is proportional to C_Q^2/ω_0, so it is usually smaller than the 1st-order quadrupolar interaction. And the 1st-order interaction does not affect the central transition.

1.3 Population transfer from satellite transitions

In the recent year, Solid-State Nuclear Magnetic Resonance (SS-NMR) spectroscopy has been a powerful tool for providing impressive insights into the structure and dynamics of many systems in the area of chemistry, biology, geology, and materials science. Traditionally, NMR is offered for nuclei with spin I = 1/2 (such as ^{1}H, ^{13}C, ^{15}N), allowing convenient spectroscopic access to organic and biological matter. However, if we characterise inorganic materials with NMR spectroscopy, more than 70% of the nuclei are with a spin number larger than one half, e.g. ^{14}N (I = 1), ^{11}B (I = 3/2), ^{27}Al (I = 5/2), or ^{45}Sc (I = 7/2). A nucleus with spin I > 1/2 exhibits more than one NMR transition, and also possesses a quadrupole moment. This interaction of quadrupole moment with the electronic surroundings of the nucleus, the second largest interaction only smaller than the fundamental Zeeman interaction, will dominate the appearance of the NMR spectrum. The presence of the quadrupolar interaction also has an effect on how nuclei with $I > 1/2$ interact with radio frequency (RF) in NMR experiments. At the same time, we can obtain the information about the symmetry of the electronic surroundings of the observed nucleus from the quadrupolar coupling tensor, which may be very useful[20].

For a powder sample, the presence of the quadrupolar interaction will lead to severe broadening of the NMR resonance linewidths. Quadrupolar nuclei also suffer

from low natural abundance and/or small gyromagnetic ratios, and result in poor sensitiity. Hence, to acquire a solid-state NMR spectra of quadrupolar nuclei can be a task full of challenge[20].

In this section, we will introduce three different methods which have already been designed to transfer magnetization from the STs to the CT in order to improve the polarization of the CT. There are two general mechanisms describing this process, one is ST saturation which is easier to accomplish, equalizing the populations of two adjacent energy levels. By saturating the STs, a maximum theoretical enhancement of the CT of I+1/2 can be achieved, where I is the nuclear spin number, corresponding to enhancements of 2, 3, 4, and 5 for nuclei with spins of 3/2, 5/2, 7/2, and 9/2, respectively. The other one is ST inversion, the magnetization from all transitions can be transferred to the CT by a series of ST inversions. Note that for half-integer quadrupoles with spin numbers of 5/2 or greater, this ST inversion should start from the outer STs to the inner STs, to achieve the maximum 2I enhancement. This corresponds to enhancements of 3, 5, 7, and 9 for nuclei with spins of 3/2, 5/2, 7/2, and 9/2[21]. These concepts are represented in Fig. 3.
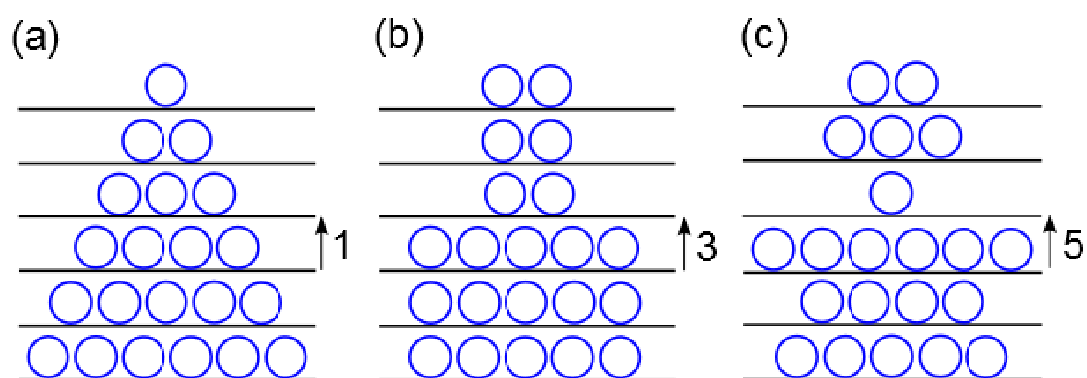

Fig.3 Energy level diagram for a spin 5/2 nucleus with exaggerated population differences represented by 'littleballs'. The populations of the states at thermal equilibrium are shown in (a), those after saturation of the STs are shown in (b), and after a ST inversion starting from the outer STs (d). A vertical arrow indicates the enhancement of a given CT signal

1.3.1 WURST

WURST stands for Wideband, Uniform rate, Smooth Truncation. This shape pulse is used for adiabatic inversion to induce population transfer (PT) between different energy levels of quadrupolar nuclei, thereby leading to a significant gain in intensity for the central transition (CT). The amplitude, $\omega_1(t)$, and phase variation, $\phi(t)$, are given by:

$$\omega_1(t) = \omega_1(\max)\left\{1 - \left|\cos(\frac{\pi t}{\tau_w})\right|^N\right\} \tag{19}$$

$$\phi(t) = \pm 2\pi\left\{(\upsilon_{off} + \frac{\Delta}{2})t - (\frac{\Delta}{2\tau_w})t^2\right\} \tag{20}$$

and shown in Fig.4 $\omega_1(\max)$ is the maximum RF amplitude and τ_w is the pulse duration. N determines the extent to which the edges of the pulse are rounded off. Δ is the total sweep range (in Hz) and ν_{off} is the offset frequency for the centre of the sweep (also in Hz)[22].

WURST only needs a low peak Radio frequency field level and inverts uniformly on a wide frequency range. If a single WURST inversion pulse is applied to a single satellite transition spinning sideband, it can invert the full manifold of satellite spinning sidebands. Furthermore selective inversion of resolved satellite spinning sidebands can also be used to perform spectral editing of overlapping sites in a central transition spectrum[23].

1.3.2 DFS

DFS stands for double frequency sweep, consisting of two sidebands generated by a time-dependent amplitude modulation of the rf-carrier frequency. The amplitude, $\omega_1(t)$, is given by:

$$\omega_1(t) = \omega_1 \cos(\omega_s t - (\omega_s - \omega_f)\frac{t^2}{2\tau}) \tag{21}$$

and shown in Fig.4 This leads to two sidebands that are swept from the start frequency ω_s to the final frequency ω_f during the duration τ of the sweep[24].

This can be used to manipulate the satellite transitions of the spin systems. An

adiabatic pulse of the satellites to invert their populations prior to a selective excitation of the central transition can result in signal enhancement in both static and magic-angle spinning spectra.

In this scheme, the population of the nuclear spin states associated with the satellite transitions (STs) are manipulated, the population difference between the central $m_I = 1/2$ and $m_I = -1/2$ energy states is increased, so when observe the CT, the sensitivity is enhanced. The strategy behind using the DFS as an enhancement technique for single crystals is to manipulate adiabatically all the satellite transitions to invert their population and maximizing the population difference between the $m_I = 1/2$ and $m_I = -1/2$ states before excitation of the CT[25]. This pulse sequence ensures the maximum theoretical enhancements. This pulse also has been extended to stationary powder samples with success, in which DFS with large sweep widths are used to cover all the STs resulting from the orientation dependence of the quadrupolar interaction in powder. However for powder samples under MAS condition, it is difficult to invert all the STs consistently, because of the combined frequency sweeping and time dependent resonance position of the STs due to the reorientation of the powder particles with respect to the external magnetic field. As a result the satellite transitions are swept at different effective rates and in different order depending on the frequency trajectory of the satellite transitions of a particular powder orientation. The final effect is that the spin system is in a different state at the end of the frequency sweep for each crystallite, resulting in different effective enhancements for every crystallite[26]. This can be improved by applying a much narrower adiabatic sweep covering only one single set of ST spinning sidebands (ssb). Recently it is proved that a narrow band adiabatic sweep over a single ST ssb performs much better than a wide band adiabatic sweep over the whole ssb manifold under MAS conditions[27].

1.3.3 HS

Hyperbolic secant, HS, pulses, first used in laser spectroscopy in 1969[28], were used to provide highly selective, low-power π-pulses for MRI applications[29,30]. The HS pulse inversion profile is independent of the applied rf field, provided that it is above a certain power level. The HS pulse is created using both amplitude, $\omega_1(t)$, and phase variation, $\phi(t)$, which are given by[31] :

$$\omega_1(t) = \omega_1(\max)\sec h(\beta(\frac{2t}{T_p}-1)) \tag{21}$$

$$\phi(t) = (\frac{\lambda}{\beta})(\frac{T_p}{2})\ln[\cosh(\beta(\frac{2t}{T_p}-1))] + \Delta\omega_0 t \tag{22}$$

and shown in Fig.4 $\omega_1(\max)$ is the maximum amplitude of the pulse, T_P is the pulse length, β is a truncation factor which limits the sech function at an amplitude of 1%, λ is equal to one half of the inversion bandwidth, and $\Delta\omega_0$ is the offset of the HS pulse from the carrier frequency. The phase variation, $\phi(t)$, generates an effective frequency sweep (i.e., the derivative of the phase), $\Delta\omega(t)$, over the bandwidth centered at a particular offset, $\Delta\omega_0$, given by[32]:

$$\Delta\omega(t) = \lambda\tanh(\beta(\frac{2t}{T_p}-1)) + \Delta\omega_0 \tag{23}$$

Population inversion only occurs if the frequency sweep is adiabatic, and the sweep must be fast enough so that longitudinal spin relaxation during the sweep is negligible. To obtain an adiabatic HS shape pulse, we should optimize the rf field at a given pulse duration or optimize the pulse duration at a given rf field. The maximum enhancements are realized when the HS offsets are equal to the frequency corresponding to the maximum probability of crystallites within the sample, i.e., the position of the 'horns' of ST1, and only one spinning sideband generated from the satellite transitions need be inverted for maximum enhancement. So the bandwidth of the HS pulses should be set to the spinning frequency to ensure inversion of a complete satellite sideband. A lower enhancement is found when the bandwidth is equal to twice the spinning speed and a smaller secondary maximum is found at three times the spinning speed. However, the duration of the HS pulse is not very critical

provided, it is above a threshold value[31].

Due to the fact that a large proportion of NMR-active nuclides are quadrupolar nuclei, and that sensitivity remains one of the central problems in NMR spectroscopy, this is an important area of ongoing research. Several methods for enhancing the central transition in NMR spectra of half integer spin quadrupolar nuclei have been discussed. Application of these techniques will almost always result in significant enhancements of the CT, particularly for spin-3/2 and spin-5/2 systems contained in MAS samples[20,21].
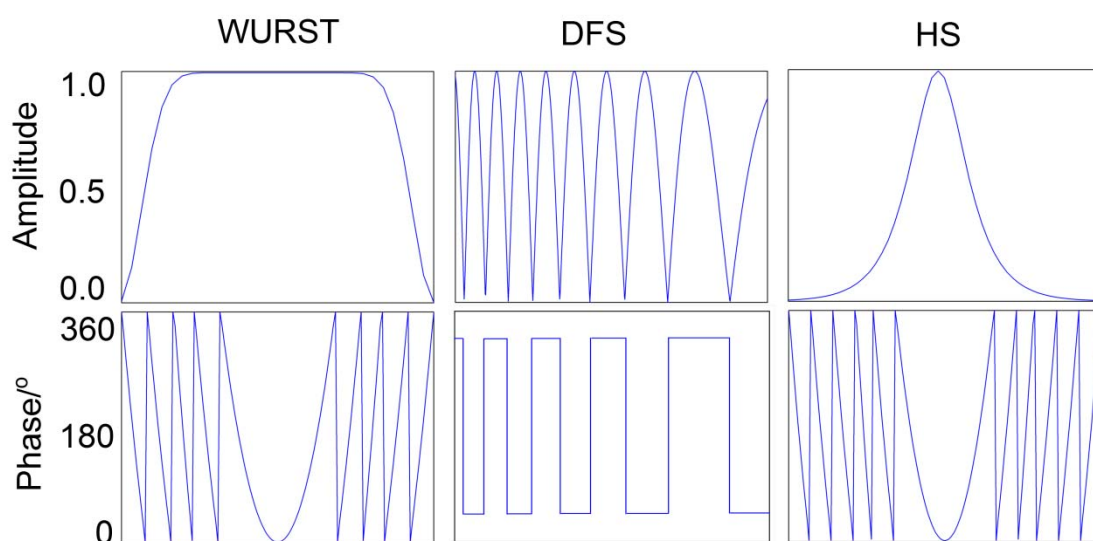
Fig.4 The amplitude and phase modulation for all of the population transfer schemes

1.4. NMR Spectrum

1.4.1 Fourier transformation two-dimensional (FT2D) spectroscopy

The NMR quadrature-detected signal (FID) has the form:

$$s(t) = \sum_l s_l(t) \tag{24}$$

$$s_l(t) = a_l \exp\{(i\Omega_l - \lambda_l)t\} \tag{25}$$

It describes a superposition of many different signal components s_l, each component s_l has a different frequency Ω_l, a different damping rate constant λ_l, and a different amplitude a_l.

Fourier transformation (FT) is a mathematical technique which converts a

function of time into a function of frequency. The effect is to make the individual components of the signal visible and plot their frequencies in a visually accessible form. FT does not enhance the theoretical information content, but makes the information in the signal more accessible.

The mathematical definition of FT is

$$S(\Omega) = \int_0^\infty s(t) \exp\{i\Omega_l t\} dt \tag{26}$$

the 'input' s is a function of time t; the 'output' S is a function of a frequency variable Ω, and is called the spectrum.

If Equation.26 is applied to Equation.24, we obtain

$$S(\Omega) = \sum_l S_l(\Omega) \tag{27}$$

In which each spectral component $S_l(\Omega)$ is the Fourier transform of the corresponding signal component:

$$S_l(\Omega) = \int_0^\infty s_l(t) \exp\{-i\Omega_l t\} dt \tag{28}$$

from Equation 25, it can be written as

$$S_l(\Omega) = a_l \int_0^\infty \exp\{-(i(\Omega - \Omega_l) + \lambda_l)t\} dt \tag{29}$$

Suppose that an arrayed experiment is conducted, the result is a two-dimensional data matrix as a function of two time variables, in many important cases, the signal has the following form:

$$s(t_1, t_2) = \sum_l s_l(t_1, t_2) \tag{30}$$

$$s_l(t_1, t_2) = a_l \exp\{(i\Omega_l^{(1)} - \lambda_l^{(1)})t_1 + (i\Omega_l^{(2)} - \lambda_l^{(2)})t_2\} \tag{31}$$

the two-dimensional signal is a sum of individual contributions l ; each contribution has a complex amplitude a_l, with frequency $\Omega_l^{(1)}$ in the t_1 dimension and frequency $\Omega_l^{(2)}$ in the t_2 dimension, and peakwidth parameters $\lambda_l^{(1)}$ λ and $\lambda_l^{(2)}$ in the two dimensions.

The two-dimensional signal needs two-dimensional FT, which is defined through the double integral:

$$S(\Omega_1, \Omega_2) = \int_0^\infty dt_1 \int_0^\infty dt_2 s(t_1, t_2) \exp\{-(i(\Omega_1 t_1 + \Omega_2 t_2))\} \tag{32}$$

It is a function of two frequency variables. The function $S(\Omega_1, \Omega_2)$ is called the two-dimensional spectrum[1].

1.4.2 Covariance Spectroscopy

The covariance analysis was first applied to liquid-state 2D HOMCOR NMR experiments by Bruschweiler et al.[33,34]. Covariance spectroscopy had also been deduced independently by Hu et al.[35] from the theory of generalized 2D (GEN2D) spectroscopy, which was developed in the optical field[36-39], such as infrared, Raman, near-infrared and ultraviolet spectroscopy, and then applied to diffusion NMR[40] experiments and solid-state NMR[41-47] .

In the case of two-dimensional covariance spectroscopy (COV2D), it is convenient to call t_1 and t_2 the evolution and detection times of a homo-nuclear signal $S(t_1, t_2)$, respectively. After Fourier transform with respect to t_2, this signal is converted into a mixed 2D matrix $S(t_1, \omega_2)$, from which only the real part is kept after phasing and apodization with respect to ω_2. The fact that the same phasing is mathematically used in COV2D along the indirect dimension is a significant advantage in case of broad resonances where it is often difficult to perform with FT2D. From this initial matrix, two lightly different homo-nuclear matrices can be computed by covariance analysis:

$$C(\omega_1, \omega_2) = C(\omega_2, \omega_2) = S(t_1, \omega_2)^T S(t_1, \omega_2) \tag{33}$$

$$F(\omega_1, \omega_2) = \sqrt{C(\omega_1, \omega_2)} \tag{34}$$

These HOMCOR spectra are real and symmetric, and they are called covariance (C) and cross-correlation (F) spectra, respectively. The correlation information in these two spectra is identical. It must be noted that Eq.34 corresponds to the square-root of a matrix, not of a scalar number, whose computation can be speeded up by singular value decomposition (SVD) method[48]. The cross-correlation spectrum $F(\omega_1, \omega_2)$ is similar to that obtained with FT2D and the covariance spectrum $C(\omega_1, \omega_2)$ similar to the power spectrum deduced from FT2D. In this paper, only the cross-correlation spectrum

F(ω_1, ω_2) will be produced.

C(ω_1, ω_2) was proved to cover all the correlation information in FT2D spectrum S(ω_1, ω_2), however, C(ω_1, ω_2) was shown to contain some correlation information which are not existed in FT2D spectrum S(ω_1, ω_2). For example, a cross peak between C_1 and C_2 might be present in COV2D spectrum if C_3 correlated with C_1 as well as C_2 but C_1 did not correlate with C_2 in FT2D spectrum. The theory for the occurrence of this kind of "relayed" peaks in COV2D spectrum has been demonstrated in the supporting information. Thus, this behavior may impose some limitations on the applications of COV2D. In practice, COV2D is useful for the NOESY, ROESY and TOCSY in liquid-state NMR[49] and DARR[50,51], PARISxy[52-55], SHANGHAI[56] and some other SQ–SQ (single quantum–single quantum) and DQ–SQ (double quantum–single quantum) experiments in solid-state NMR.

1.5. New strategy

1.5.1 PT-HMQC

We will propose a simple and robust strategy to accelerate the rate of coherence transfer by manipulating the population of STs, and enhance the sensitivity of *J*-HMQC experiments with indirect detection of the quadrupolar nucleus. We analyze this simple and robust strategy in details by combining theory, simulations and experiments. We find that for half-integer quadrupolar nuclei the rate of coherence transfers can be increased with different types of processes when the PT-HMQC (Population Transfer HMQC) method is employed. Compared with the conventional HMQC method, PT-HMQC utilizes an additional adiabatic pulse for satellites manipulation, which can be optimized separately via one-pulse CT experiments. We further demonstrate that this strategy is an efficient technique, which allows enhancing the sensitivity of *J*-HETCOR experiments between two half-integer quadrupolar isotopes (e.g. ^{27}Al-^{17}O). Moreover, this concept of population transfer

can also be applied to dipolar-mediated D-HMQC experiments, in which the dipolar recoupling time is short compared to T_2' values. We also improve the population transfer method, and find the most stable and efficient sequence.

1.5.2 COV2D combined with various sampling schemes and accumulation profiles

We will show that the covariance method can be effectively applied to the data acquired by NUCA-FT2D (fourier transformation 2D with non-uniform and consecutive acquisition scheme), inducing up to 100% increase in the cross-peak intensities and 50% enhancement of signal to noise ratio (S/N) in both dimensions in the NUCA-COV2D (covariance processing with a non-uniform continuous acquisition scheme) spectra compared to those in UCA-COV2D (covariance processing with uniform continuous acquisition scheme) spectra, without deteriorating the cross-peak resolutions. Meanwhile, NUCA-COV2D can save considerable experimental time while increasing the spectral resolution compared with corresponding NUCA-FT2D.

Furthermore the COV2D approach can be applied with at least two different reduced sampling schemes along t_1 to decrease the protracted experimental time. It can either be combined with NUS[57-59] (non-uniform sampling) t_1 sampling, or simply use a limited number of t_1 points with CUO (t_1 cut-off) sampling. Both sampling methods have the benefit of saving time, while keeping the quality of NMR spectra. We will show that for the same experimental time, COV2D with CUO sampling (CUO-COV2D) is always more sensitive than NUS-COV2D. In addition, we demonstrate that with COV2D, Gaussian accumulation profile presents better performance than constant square profile.

References

[1] M.H. Levitt, F.H. Forsterling, Spin dynamics: Basics of Nuclear Magnetic Resonance, Second Edition, Jonh Wiley & Sons (2010).

[2] R.R. Ernst, W.A. Anderson, *Rev. Sci. Inst.*, **37**, 93 (1966).

[3] L. Müller, A. Kumar, R.R. Ernst, *J. Chem. Phys.*, **63**, 5490 (1975).

[4] E.R. Andrew, A. Bradbury, R.G. Eades, *Nature*, **183**, 1802 (1959).

[5] I.J. Lowe, *Phys. Rev. Lett.*, **2**, 285 (1959).

[6] K. Schmidt-Rohr, H.W. Spiess, Multidimensional solid-state NMR and polymers, Academic Press, 1994, London.

[7] P. Mansfield, *Prog. Nucl. Mag. Res. Sp.*, **8**, 41 (1970).

[8] U. Haeberlen, High resolution NMR in solids, Supplement 1 to Advances in magnetic resonance, Academic Press, 1976, New York.

[9] S. R. Hartmann, E. L. Hahn, *Phys. Rev.*, **128**, 2042 (1962).

[10] H.J. Jakobsen, J. Skibsted, H. Bildsøe, N.C. Nielsen, *J. Magn. Reson.*, **85**, 173 (1989).

[11] D. Massiot, V. Montouillout, F. Fayon, P. Florian, C. Bessada, *Chem. Phys. Lett.*, **272**, 295 (1997).

[12] T. Gullion, J. Schaefer, *J. Magn. Reson.*, **81**, 196 (1989).

[13] C.A. Fyfe, K.T. Mueller, K.C. Wong-Moon, *Chem. Phys. Lett.*, **199**, 198 (1992).

[14] T. Gullion, *Chem. Phys. Lett.*, **246**, 325 (1995).

[15] T. Gullion, *J. Magn. Reson.* A, **117**, 326 (1995).

[16] Z. Gan, *Chem. Commun.*, 4712-4714 (2006).

[17] B.F. Chmelka, A. Pines, *Science*, **246**, 71 (1989).

[18] B.F. Chmelka, K.T. Mueller, A. Pines, J. Stebbins,Y. Wu, J.W. Zwanziger, *Nature*, **339**, 42 (1989).

[19] L. Frydman, J.S. Harwood, *J. Am. Chem. Soc.*, **117**, 5367 (1995).

[20] Bräuniger, T.; Jansen, M. *Zeitschrift für anorganische und allgemeine Chemie*, **639**, 857-879 (2013).

[21] Perras, F. A.; Viger-Gravel, J.; Burgess, K. M. N.; Bryce, D. L. *Solid State Nuclear Magnetic Resonance*, **51-52**, 1-15 (2013).

[22] O'Dell, L. A. *Solid State Nucl Magn Reson*, **55-56**, 28-41 (2013).

[23] Dey, K. K.; Prasad, S.; Ash, J. T.; Deschamps, M.; Grandinetti, P. J. *J Magn Reson*, **185**, 326-330 (2007).

[24] A.P.M. Kentgens, R. V., *Chem. Phys. Lett.*, **300**, 435–443 (1999)

[25] D. Iuga, H. Schafer, R. Verhagen, A.P.M. Kentgens, *J. Magn. Reson.* **147**, 192–209 (2000).

[26] D. Iuga, A.P.M. Kentgens, *J.Magn. Reson.* **158**, 65–72 (2002).

[27] Goswami, M.; van Bentum, P. J.; Kentgens, A. P. *J Magn Reson*, **219**, 25-32 (2012).

[28] S.L. McCall, E.L. Hahn, Self-induced transparency, *Phys. Rev.* **183**, 457–485   (1969).

[29] M.S. Silver, R.I. Joseph, D.I. Hoult, *J. Magn. Reson*, **59**, 347–351 (1984).

[30] M.S. Silver, R.I. Joseph, D.I. Hoult, *Magn. Reson. Med.*, **1**, 294 (1984).

[31] Siegel, R.; Nakashima, T. T.; Wasylishen, R. E. *J Magn Reson*, **184**, 85-100 (2007)

[32] E. Kupcˇe, R. Freeman, *J. Magn. Reson. A*, **117**, 246–256 (1995).

[33] R. Bruschweiler and F. Zhang, *Journal of Chemical Physics*, **120**, 5253-5260 (2004)

[34] R. Bruschweiler, *Journal of Chemical Physics*, **121**, 409 (2004).

[35] B. W. Hu, P. Zhou, I. Noda and G. Z. Zhao, *Analytical Chemistry*, **77**, 7534 (2005).

[36] I. Noda, *J. Am. Chem. Soc.*, **111**, 8116-8118 (1989)

[37] I. Noda, *Appl. Spectrosc.*, **47**, 1329-1336 (1992).

[38] I. Noda, *Appl. Spectrosc.*, **54**, 994-999 (2000).

[39] I. Noda, A. E. Dowrey, C. Marcott, G. M. Story and Y. Ozaki, *Appl. Spectrosc.*, **54**, 236A-248A (2000).

[40] C. D. Eads and I. Noda, *J. Am. Chem. Soc.*, **124**, 1111-1118 (2002).

[41] B. Hu, J. P. Amoureux, J. Trébosc, M. Deschamps and G. Tricot, *Journal of Chemical Physics*, **128**, 134502 (2008).

[42] M. Weingarth, P. Tekely, R. Brüschweiler and G. Bodenhausen, *Chem. Commun.*, **46**, 952-954 (2010).

[43] R. Aspers, P. Geutjes, M. Honing and M. Jaeger, *Magnetic Resonance in Chemistry*, **49**, 425-436 (2011).

[44] F. L. Zhang, L. Bruschweiler-Li and R. Bruschweiler, *Journal of the American Chemical Society*, **132**, 16922-16927 (2010).

[45] B. Hu, J. P. Amoureux and J. Trébosc, *Solid State Nuclear Magnetic Resonance*, **31**, 163 (2007).

[46] K. Takeda, Y. Kusakabe, Y. Noda, M. Fukuchi and K. Takegoshi, *Phys. Chem. Chem. Phys.*, **14**, 9715-9721 (2012).

[47] G. E. Martin, B. D. Hilton, M. R. W. III and K. A. Blinov, *Magn. Reson. Chem.*, **49** 641-647 (2011).

[48] B. Hu, O. Lafon, J. Trébos, Q. Chen, J.-P. Amoureux, *J. Magn. Reson.*, **212**, 320–329 (2011).

[49] B.M. Fung, A.K. Khitrin, K. Ermolaev, *J. Magn. Reson.*, **142**, 97–101 (2000).

[50] K. Takegoshi, S. Nakamura, T. Terao, *Chem. Phys. Lett.*, **344**, 631–637 (2000).

[51] K. Takegoshi, S. Nakamura, T. Terao , *J. Chem. Phys.*, 118, 2325–2341 (2003).

[52] L. Duma, D. Abergel, F. Ferrage, P. Pelupessy, P. Tekely, G. Bodenhausen, *Chem. Phys. Chem.*, **9**, 1104–1106 (2008).

[53] M. Weingarth, G. Bodenhausen, P. Tekely, *Chem. Phys. Lett.*, **488**, 10–16 (2010).

[54] M. Weingarth, D.E. Demco, G. Bodenhausen, P. Tekely, *Chem. Phys. Lett.* , **469**, 342–348 (2009).

[55] M. Weingarth, G. Bodenhausen, P. Tekely, *J. Am. Chem. Soc.*, **131**, 13937–13939 (2009).

[56] B. Hu, J.P. Amoureux, J. Trébosc, M. Deschamps, G. Tricot, *J. Chem. Phys*, **128**, 134502 (2008).

[57] D. Rovnyak, M. Sarcone, Z. Jiang, *Magn. Reson. Chem.*, 49, 483–491 (2011).

[58] J.C.J. Barna, E.D. Laue, M.R. Mayger, J. Skilling, S.J.P. Worrall, *J. Magn. Reson.*, **73**, 69–77 (1987) (1969).

[59] K. Kazimierczuk, A. Zawadzka, W. Koz′min′ ski, I. Zhukov, *J. Magn. Reson.*, **188**, 344–356 (2007).

Chapter 2: New pulse sequences for heteronuclear experiments

Solid-State Nuclear Magnetic Resonance (SS-NMR) spectroscopy is a powerful tool for providing impressive insights into the structure and dynamics of many systems in the area of chemistry, biology, geology, and materials science. In the recent years, the design of SSNMR experiments to probe homo- or hetero-nuclear proximities or connectivities for resolution purpose under magic-angle-spinning (MAS) has been a fascinating topic. In these experiments, the dipolar (D)- or J-couplings are favorable medias for magnetization transfers, since they contain useful structural information about the space proximity and bond connectivity, respectively. Further exploitation of D/J couplings in solids resulted in the development of 2D homo- and hetero-nuclear correlation spectroscopies.

In heteronuclear SS-NMR correlation experiments, the coherence transfer between two different isotopes is usually achieved through space via dipolar-mediated methods, such as Cross-Polarization (CP)[1], Transferred-Echo Double-Resonance (TEDOR)[2], Dipolar-coupling mediated Insensitive Nuclei Enhanced by Polarization Transfer (D-INEPT)[3,4], and D-HMQC (Dipolar-coupling mediated Heteronuclear Multiple Quantum Coherence)[4-6]. However, in most cases the dipolar interactions are quasi-averaged at fast MAS, and thus various dipolar recoupling schemes, which reintroduce these heteronuclear dipolar interactions during the periods of coherence transfer, have been proposed for structural elucidation, e.g. Rotational Echo Double Resonance (REDOR)[7], Rotary Resonance Recoupling (R^3)[8], Simultaneous Frequency and Amplitude Modulation (SFAM)[9] and CN^{ν}_n/RN^{ν}_n symmetry-based sequences[10]. On the other hand, the J couplings are also widely used for the investigation of the chemical-bond map between spins in the solid state, although they are relative small. Many J-mediated SSNMR methods have been reported recently[11-16], and most of them including J-INEPT or J-HMQC schemes are derived

from liquid-state NMR.

A major limitation of these J-mediated HETeronuclear CORrelation (J-HETCOR) experiments involving quadrupolar nuclei is their lack of sensitivity, since the heteronuclear J couplings are often smaller than the rate, $1/T_2$'(transverse relaxation time constant), of transverse losses. For instance, for alumino-phosphates, typical J_{Al-P} values are about 20 Hz, whereas the $1/T_2$' values are usually larger than 100 Hz. Meanwhile, fast transverse losses might also be a problem for D-HETCOR (Dipolar coupling mediated HETeronuclear CORrelation) experiments for the observation of long-range distances or the study of paramagnetic materials.

In particular, in the presence of quadrupolar nuclei, the complex interference between the radio-frequency (rf) field and the large quadrupolar interactions, and the broadening of the resonances caused by second-order quadrupolar dephasings, lead to additional difficulties for these heteronuclear experiments[17,18]. Many approaches have been developed to overcome the lack of sensitivity of J- and D-HETCOR experiments involving half-integer spin quadrupolar nucleus. So far, most of the successful experiments to probe the proximities and connectivities between spin-1/2 (^1H, ^{13}C, ^{31}P, ...) and half-integer quadrupolar (^{23}Na, ^{17}O, ^{27}Al...) nuclei have been based on the HMQC indirect detection[19-21]. These methods use rf pulses with low power on the quadrupolar nucleus to only selectively irradiate its Central Transition (CT: ½ ↔ -½). Due to the second-order quadrupolar broadenings, the sensitivity of HMQC experiments then always remains small. One way to increase it is by recycling the signal at the end with a Quadrupolar Carr-Purcell-Meiboon-Gill (QCPMG) accumulation[22] when the T_2' time of the detected nucleus is longer than its apparent transverse dephasing time constant, T_2*. When the quadrupolar nucleus is directly observed, its CT signal can be further enhanced by adiabatically manipulating the populations of the satellite transitions (ST) at the beginning of the sequence prior to the excitation of CT transverse magnetization. On the contrary, no method has been

reported hitherto to further improve the experimental sensitivity when half-integer quadrupolar nuclei are indirectly detected with HMQC experiments. However, this type of method can be advantageous since (i) it benefits from higher sensitivity for correlation between low-quadrupolar isotopes (e.g. ^{17}O, ^{43}Ca) and high-nuclei (e.g. ^{1}H or ^{19}F); (ii) it requires a small number of t_1 increments owing to second-order quadrupolar broadening in the indirect dimension and hence shorter acquisition time in the sampling-limited data collection regime; (iii) it provides a strategy to identify the connectivity between two different quadrupolar isotopes (e.g. ^{27}Al-^{17}O).

In this chapter, we propose a simple and robust strategy to accelerate the rate of coherence transfer by manipulating the population of STs, and enhance the sensitivity of *J*-HMQC experiments with indirect detection of the quadrupolar nucleus. We analyze this simple and robust strategy in details by combining theory, simulations and experiments. We find that for half-integer quadrupolar nuclei the rate of coherence transfers can be increased with different types of processes when the PT-HMQC (Population Transfer HMQC) method is employed. Compared with the conventional HMQC method, PT-HMQC utilizes an additional adiabatic pulse for satellites manipulation, which can be optimized separately via one-pulse CT experiments. We further demonstrate that this strategy is an efficient technique, which allows enhancing the sensitivity of *J*-HETCOR experiments between two half-integer quadrupolar isotopes (e.g. ^{27}Al-^{17}O). Moreover, this concept of population transfer can also be applied to dipolar-mediated *D*-HMQC experiments, in which the dipolar recoupling time is short compared to T_2' values.

2.1 Theory

2.1.1 Indirect detection of quadrupolar nuclei using *J*-HMQC

The basic HMQC sequence is presented in Fig. 1a. This sequence allows correlating the signal of I nuclei with the CT of quadrupolar S nuclei. The CT

single-quantum coherences of S spins, which evolve during the indirect evolution period, are excited and reconverted using CT-selective π/2-pulses[23].

We derive the analytical expression of J-HMQC signal when the S isotope is a half integer quadrupolar nucleus. For the sake of simplicity, the expression is derived for an isolated 1/2-3/2 (I-S) spin-pair. The first pulse on the I channel in the scheme of Fig. 1a creates tranverse in-phase magnetization of the I nucleus, I_y. We assume that MAS average out the anisotropic NMR interactions and the evolution under the isotropic chemical shift of the I nucleus is refocused by the central 180° pulse on the S channel. Therefore, during the first τ_{mix} delay, we can only consider the evolution of I_y under the heteronuclear J-coupling.

$$I_y \xrightarrow{\quad 2\pi J I_z S_z \tau_{mix} \quad}$$

$$e^{-iH_J\tau_{mix}} I_y e^{iH_J\tau_{mix}} = e^{-iH_J\tau_{mix}}(I_y \otimes E)e^{iH_J\tau_{mix}} = e^{-iH_J\tau_{mix}}(I_y E_C)e^{iH_J\tau_{mix}} + e^{-iH_J\tau_{mix}}(I_y E_T)e^{iH_J\tau_{mix}} \quad (1)$$

In the above equation, the right member corresponds to the instant A in Fig. 1a. Here, $H_J = 2\pi J I_z S_z$ and according to commutation relations[12,23-25], the right member of Eq. 1 is equal to

$$e^{-iH_J\tau_{mix}} I_y e^{iH_J\tau_{mix}} = \quad (2)$$
$$I_y E_C \cos(\pi J\tau_{mix}) - 2I_x C_z \sin(\pi J\tau_{mix}) + I_y E_T \cos(3\pi J\tau_{mix}) - 2I_x T_z \sin(3\pi J\tau_{mix})$$

in which the anti-phase part is given by the second and fourth terms. C_z and T_z are the longitudinal fictitious operators associated with the CT and the triple-quantum coherence of $S = 3/2$ spin, respectively[23-25]. In the case of CT-selective excitation ($C_Q \gg \nu_{\pi/2}^{CT}$), only the second term in Eq.2 is converted into heteronuclear multiple-quantum coherences at the point B in Fig. 1a. The isotropic shift of S nucleus is encoded by the evolution of these multiple-quantum coherences during the t_1 period. Evolution of J-coupling during t_1 is cancelled by the π pulse in the middle of I channel. Hence, after the second τ_{mix} delay, the signal observed conventionally can be written as

$$s(t_1, t_2) \rightarrow -I_y \sin^2(\pi J\tau_{mix}) \cos(\Omega_S^{CT} t_1) e^{i\Omega_I t_2} \quad (3)$$

Where Ω_S^{CT} is the angular frequency corresponding to the isotropic shift of the central transition of S spin, i.e. the sum of the chemical shift and the quadrupolar induced one and Ω_I is the isotropic chemical shift of I spins.
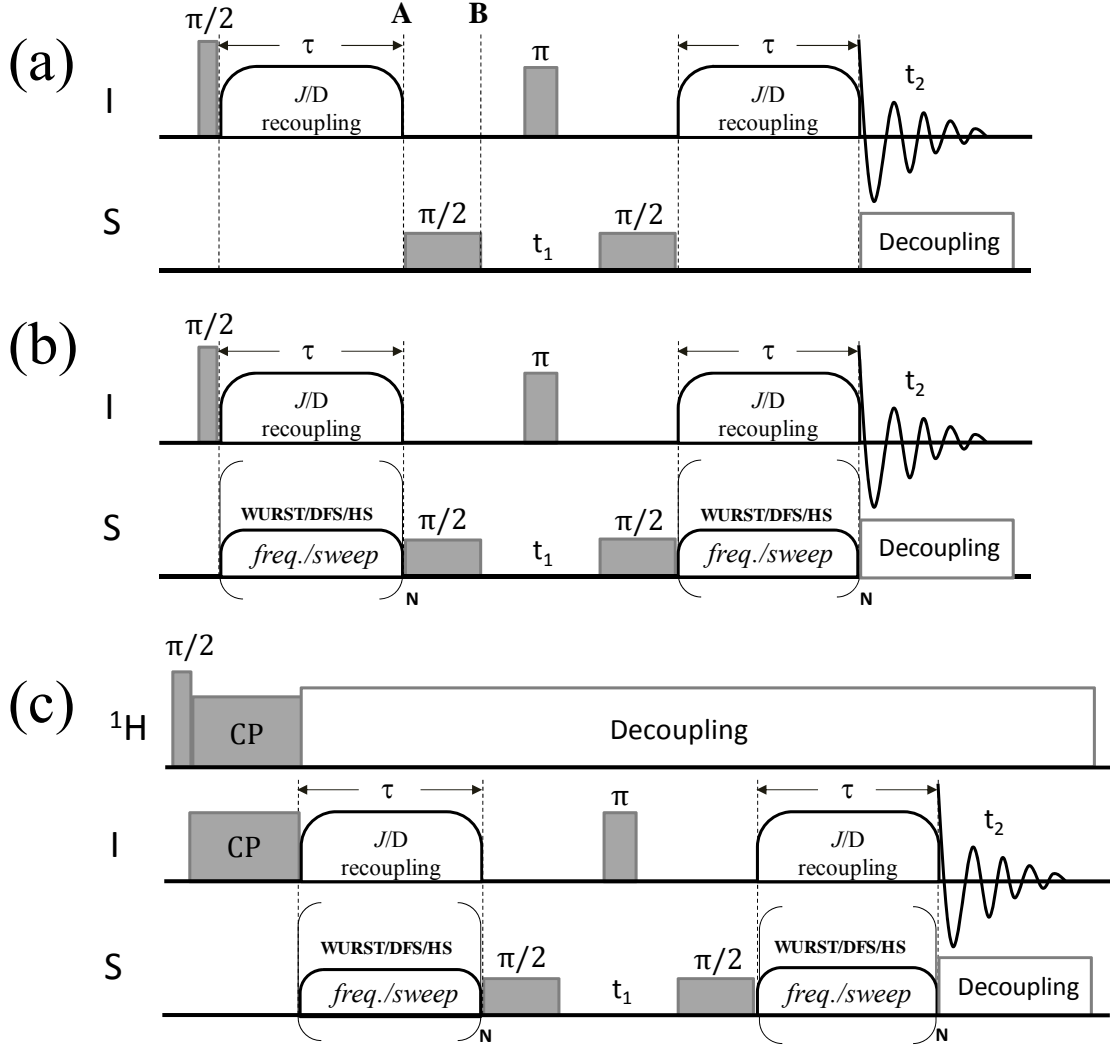

Fig.1 Pulse scheme for I-{S = n/2} HMQC-type experiments. (a) Conventional J/D-HMQC experiment; (b) PT-J/D-HMQC experiment with direct excitation of I spins; (c) PT-J/D-HMQC experiment with the initial magnetization of I spins generated by cross-polarization (CP) from protons. In the case of J-HMQC, there is no recoupling sequence on I channel, whereas in the case of D-HMQC an heteronuclei dipolar recoupling sequence, such as R^3, $SFAM_1$, or $SR4^2_1$, is sent on the I channel.

According to Eq.3, the maximal transfer efficiency of basic J-HMQC is achieved for an optimal delay of $\tau_{mix} = 1/(2J)$. Eq.2 also shows that the build-up of I magnetization, $I_x T_z$, antiphase with respect to the heteronuclear J coupling with the ST

of S nuclei is three-fold faster than that of I_xC_z. Our strategy is to make the latter term in Eq. 2 also participates in the t_1 evolution to accelerate the magnetization transfer in the HMQC experiment.

2.1.2 Indirect detection of quadrupolar nuclei using PT-J-HMQC

The simplest method is to convert the I_xT_z operator into I_xC_z before the first CT-selective $\pi/2$ pulse on S spins by manipulating the populations of the STs during or just after the first delay τ_{mix}. Then, similar conversion can also occur during or just before the second τ_{mix} delay to convert I_xC_z back to I_xT_z after the second CT-selective $\pi/2$ pulse. This approach is referred to as PT-HMQC (Population Transfer-HMQC). Fig.2 gives pictorial representations of three possible mechanisms to achieve such population transfers in J-HMQC experiments: instant inversion, instant saturation and continuous saturation during t_{mix} delays. One observes that according to the type of population transfer, the manipulations are performed either just after and just before (Fig. 2a,b) or during (Fig. 2c) the two delays τ_{mix}.

Analytical plots assuming perfect inversion or saturation transfers are shown in Fig.3 for quadrupolar nuclei with different half-integer spin numbers. Theoretically, compared with conventional J-HMQC, these three ways can lead to faster build-up rates and reduce the optimal delays significantly. Instant inversion could get the shortest optimum recoupling time with τ_{mix} divided by 2S, but an efficient inversion of magnetization is hardly achievable under MAS. Although instant saturation results in faster heteronuclear transfer than continuous saturation, the higher maximal efficiency of the later suggests that continuous saturation is the best way to be employed in PT-HMQC MAS experiments. It must be emphasized that the maximum PT-J-HMQC signal with continuous saturation is identical to that of regular J-HMQC (Fig. 3). As a result, the perfect saturation process only speeds up by a factor of S + ½ the coherence transfer when losses are not taken into account. As shown below, the continuous

saturation process can in practice be achieved by applying a series of adjacent adiabatic pulses, such as Double Frequency Sweeps (DFS)[26], Hyper-Secant (HS)[27] or Wideband, Uniform Rate, and Smooth Truncation (WURST)[28], during the τ_{mix} delay. These pulses last approximately the same time as the mixing time τ_{mix}, and the number N of these pulses must be adapted depending on the τ_{mix} delay (Fig. 1b, c).
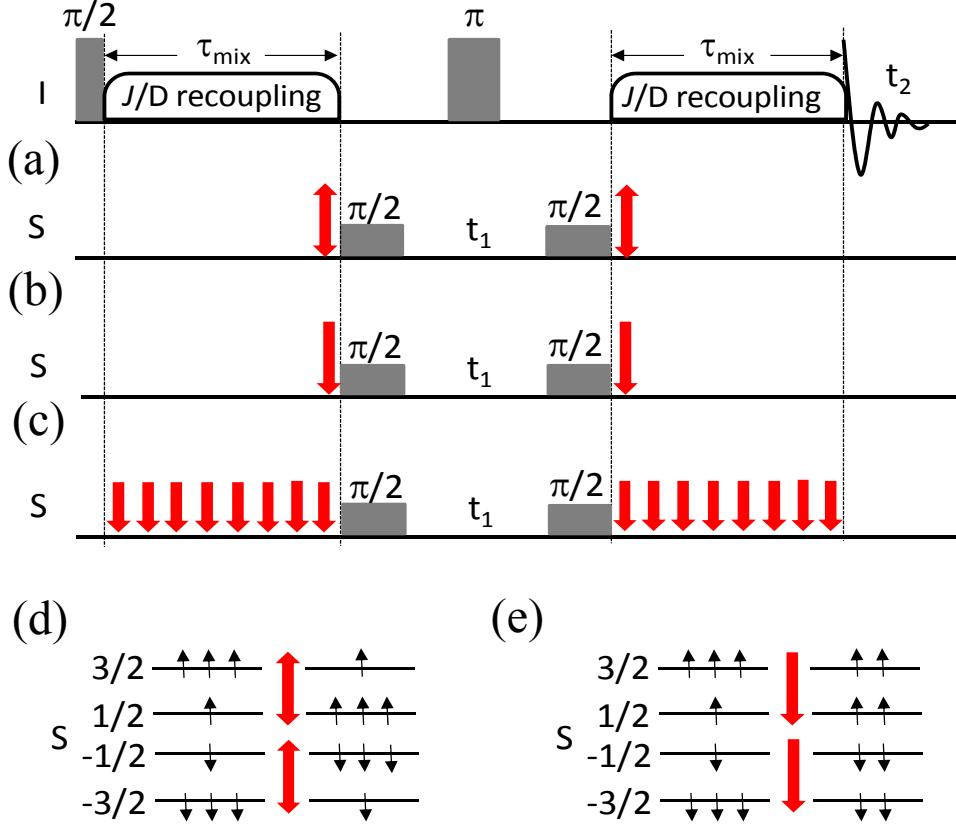

Fig.2 Pictorial representation of three hypothetic ways to achieve population transfer of satellite transitions in *J*-HMQC experiments. Two mechanisms are considered: population inversion (red double-headed arrow) and population saturation (red single-headed arrow). In (a) to (c), the red arrows indicate when the population transfers occurs. (a) instant inversion; (b) instant saturation, and (c) continuous saturation. In (c), the continuous saturation process occurs continuously throughout the whole τ_{mix} delays. The effects of population inversion (d) and saturation (e) are also depicted in the case where S=3/2. Note that depicted populations are not representative of actual spin states at the time of transfers.

As previously mentioned, the irreversible transverse relaxation time of spin I, T_{2I}', is an unavoidable factor leading experimentally to signal losses, and thus the conventional *J*-HMQC signal, described with Eq. 3, must be re-written as

$$s(t_1, t_2) \rightarrow -I_y \sin^2(\pi J \tau_{mix}) \cos(\Omega_S^{CT} t_1) e^{i\Omega_I t_2} e^{(-2\tau_{mix}/T_{2I}')} \qquad (4)$$

When the attenuation rate is much slower than the coherence transfer speed ($T_{2I}' \gg 1/J$), the maximum signal is observed for the theoretical optimum delay of $\tau_{mix} = 1/(2J)$. On the contrary, when $T_{2I}' \leq 1/J$, the maximum signal and optimum delay of J-HMQC are largely reduced. Therefore, the key advantage of shortening the theoretical optimal delay is to reduce the signal losses during the coherence transfer and thus to improve the practical transfer efficiency of J-HMQC experiments in the case of $T_{2I}' \leq 1/J$.
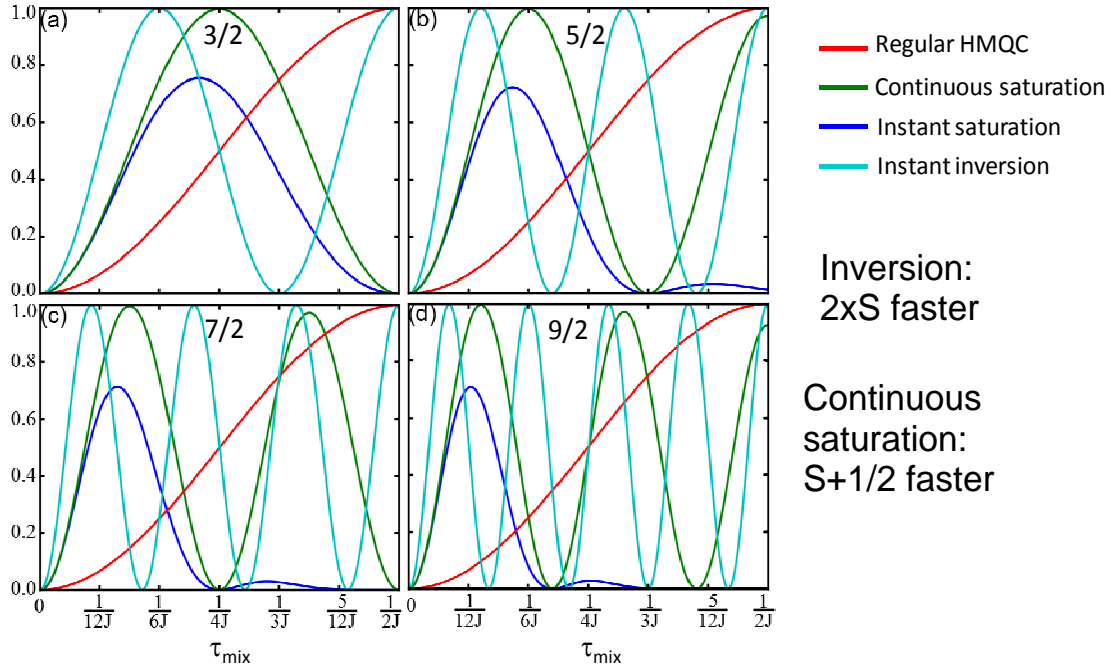

Fig.3 Analytical plots describing the J-HMQC signal amplitude versus the mixing time, τ_{mix}, observed with: regular J-HMQC —, or PT-J-HMQC with: — continuous saturation, — instant saturation, and — instant inversion. The saturation or inversion processes have been assumed to be perfect for quadrupolar nuclei with different spin numbers: S = 3/2 (a); 5/2 (b); 7/2 (c) and 9/2 (d). With respect to regular J-HMQC, perfect instantaneous inversion and continuous saturation are respectively 2S and S + ½ faster, but instantaneous saturation decreases the maximum signal.

2.2 Simulations and Experiments of PT-HMQC

2.2.1 Simulations

Numerical simulations were carried out with SIMPSON software (version

1.1.1)[29]. The powder averaging was accomplished using 3520 Euler orientations to relate the Molecular and Rotor frames: 320 $\{\alpha_{MR},\beta_{MR}\}$-pairs and 11 γ_{MR}-angles. The 320 $\{\alpha_{MR},\beta_{MR}\}$-pairs were selected according to the REPULSION algorithm[30], whereas the γ_{MR} angle was regularly stepped from 0° to 360°. NMR parameters (rf field and spinning rate) and spin interactions (scalar, dipolar and quadrupolar couplings and shielding) of the spin systems are specified in the figure captions.

The population transfer process follows the same principles as DFS[26], Fast Amplitude Modulation (FAM)[31,32], HS[27], or WURST[28] schemes that are commonly used to enhance the CT signal of quadrupolar nuclei. In this study, we have used WURST scheme to perform the continuous saturation with PT-HMQC.
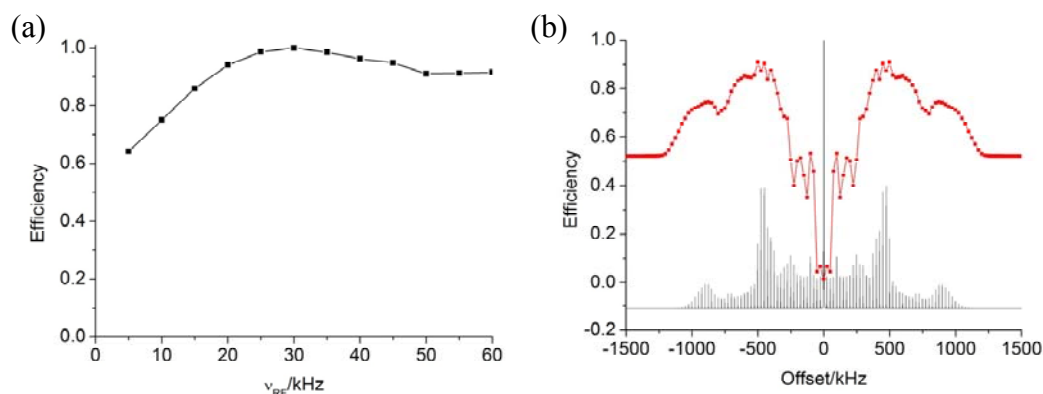

Fig.4 (a) Simulated PT-*J*-HMQC efficiency of $^{31}P \rightarrow {}^{23}Na \rightarrow {}^{31}P$ transfers obtained by applying several times the WURST pulse during $\tau_{mix} = 1/[2(S+1/2)J] = 1/4J = 2.5$ ms, versus ν_{RF} amplitude. Each WURST pulse had a duration of $2T_R$ and a frequency sweep of ν_R made about $\nu_{offset} = +473$ kHz. (b) Simulated efficiency for ^{31}P-$\{^{23}Na\}$ PT-*J*-HMQC versus ν_{offset}, with $\nu_{RF} = 30$ kHz (top), and the corresponding ^{23}Na satellite transitions MAS spectrum at the bottom. $C_Q = 2$ MHz, $\eta_Q = 0$, $B_0 = 9.4$ T, $\nu_R = 25$ kHz, $J = 100$ Hz. The efficiency has been normalized with respect to its maximum observed for $\nu_{RF} \approx 25$ kHz.

For all the simulations, we have fixed $B_0 = 9.4$ T and the spinning speed was $\nu_R = 25$ kHz. The first spin system was an isolated ^{23}Na-^{31}P (3/2-1/2) spin-pair with $J = 100$ Hz. The quadrupolar parameters of ^{23}Na were $(C_Q, \eta_Q) = (2$ MHz, 0) and this interaction was considered to the second order. The WURST basic element, with duration of $2T_R$, swept the frequency linearly over a range of ν_R about the frequency of $\nu_{offset} = +473$ kHz, which corresponds to the "horn" (the most intense region) of the

ST envelope (Fig.4b, bottom). The mixing time was fixed to its optimal value according to analytical results shown in Fig. 5: $\tau_{mix} = 1/[2(S+1/2)J] = 1/4J$. Fig. 4a displays the PT-J-HMQC efficiency of the $^{31}P \rightarrow {^{23}Na} \rightarrow {^{31}P}$ transfers obtained by applying during the periods of coherence transfer N $\approx \tau_{mix}/2T_R$ times (Fig. 1) the repetitive WURST pulse for various different rf amplitudes (ν_{RF}). Compared to conventional J-HMQC ($\nu_{RF} = 0$), we observed a nearly twice enhancement of the transfer efficiency when the rf-amplitude of WURST pulse is over 20 kHz. The simulated efficiency for ^{31}P-$\{^{23}Na\}$ PT-J-HMQC is displayed in Fig. 4b (red plot) versus the offset of WURST irradiation with $\nu_{RF} = 30$ kHz. Interestingly, this curve exhibits a profile analogue to that of ^{23}Na satellite transition MAS spectrum (Fig. 4b, bottom), except for the frequency region with small offset irradiation ($|\nu_{offset}| \leq 100kHz$) where there is a severe interference between the WURST irradiation and the CT population. Furthermore, the ^{31}P-$\{^{23}Na\}$ PT-J-HMQC efficiency with WURST manipulations has been calculated versus τ_{mix} and offset (Fig. 6a). In the case of $\nu_{offset} > 1$ MHz, the WURST pulses manipulate neither STs nor CT populations, and the optimal mixing time remains equal to its theoretical value of $\tau_{mix} \approx 1/2J = 5$ ms (Fig. 6a, square frame). This condition corresponds to the conventional J-HMQC experiment. When ν_{offset} is gradually decreased from 1000 to 450 kHz, only the STs are manipulated by the WURST irradiation, and the optimal mixing time tends toward our analytical result of $1/[2(S+1/2)J] = 1/4J = 2.5$ ms (Fig. 3). In particular, when $\nu_{offset} \approx 475$ kHz, which is the "horn" of the ST envelope, the WURST irradiation leads to the most efficient saturation for STs, thus resulting in a demonstrable effect for the acceleration of the polarization transfer in PT-J-HMQC. When $\nu_{offset} \leq 100$ kHz, the transfer efficiency of ^{31}P-$\{^{23}Na\}$ PT-J-HMQC decreases dramatically, since in this region the WURST pulses interfere with the CT of ^{23}Na, which impedes its coherence transfer. Therefore, and in the same way as with most CT enhancement experiments, an efficient manipulation of STs is associated for PT-J-HMQC
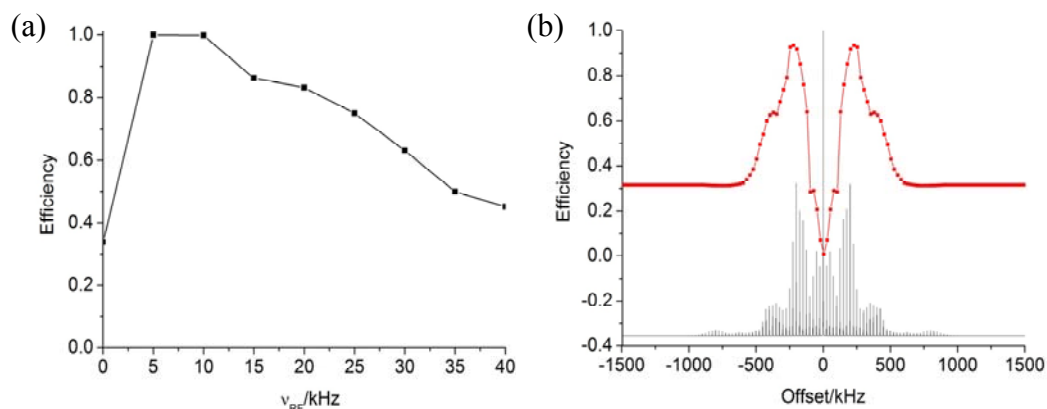
experiments with least disturbance of CT.

Fig.5 (a) Simulated PT-*J*-HMQC transfer efficiency of $^{31}P \rightarrow {}^{27}Al \rightarrow {}^{31}P$ obtained by applying several times the WURST pulse during $\tau_{mix} = 1/[2(S+1/2)J] = 1/6J = 1.67$ ms, versus ν_{RF} amplitude. Each WURST pulse had duration of $2T_R$ and a frequency sweep of ν_R made about the offset of +200 kHz. (b) Simulated efficiency for ^{31}P-$\{^{27}Al\}$ PT-*J*-HMQC versus the offset of WURST irradiation with $\nu_{RF} = 10$ kHz (top), and the corresponding ^{27}Al satellite transitions (ST1 + ST2) MAS spectrum at the bottom. $C_Q = 4$ MHz, $\eta_Q = 0$, $B_0 = 9.4$ T, $\nu_R = 25$ kHz, $J = 100$ Hz. The efficiency has been normalized with respect to its maximum observed for $\nu_{RF} \approx 7$ kHz.

The simulations were also performed for an isolated ^{27}Al-^{31}P (5/2-1/2) spin-pair with $J = 100$ Hz. The quadrupolar parameters of ^{27}Al were $(C_Q, \eta_Q) = (3$ MHz, 0) and this interaction was considered to the second order. As shown in Fig. 5a, when the rf-amplitude of WURST pulses is between 5 and 10 kHz ($\nu_{offset} = 200$ kHz and $\tau_{mix} = 1/6J$), there is almost a three-time enhancement of the transfer efficiency of PT-*J*-HMQC compared to that of conventional *J*-HMQC ($\nu_{RF} = 0$). Although the value of τ_{mix} was not $1/2J$, which is the optimal value for conventional *J*-HMQC, the significant enhancement implies that PT-*J*-HMQC must have a much faster $^{31}P \rightarrow {}^{27}Al \rightarrow {}^{31}P$ transfer rate than *J*-HMQC. However, and different from the 3/2-1/2 spin-pair, the PT-*J*-HMQC efficiency largely decreases when increasing the rf-amplitude of WURST pulses ($\nu_{RF} > 10$ kHz). In the same way as for the ^{23}Na-^{31}P spin-pair, we have also represented in Fig. 5b (red plot) the simulated efficiency for ^{31}P-$\{^{27}Al\}$ PT-*J*-HMQC versus the offset of the WURST irradiation ($\nu_{RF} = 10$ kHz). Since the WURST pulses sweep the frequency linearly over a range of ν_R, the

sidebands of the first (ST1) and the second (ST2) pairs of satellite transitions are both manipulated by the WURST irradiation. Furthermore, we observe that compared to conventional J-HMQC, the coherence transfer rate of PT-J-HMQC is accelerated by a factor of slightly less than three when $\nu_{offset} \approx \pm 200$ kHz (Fig. 6b), which is the "horn" region of the ST1 envelope. More generally, in the case of a real continuous saturation process, the optimum transfer is observed at a mixing time slightly larger than $1/[2(S+1/2)J]$, and the efficiency is slightly smaller than with J-HMQC (Fig. 6a,6b, 7b).
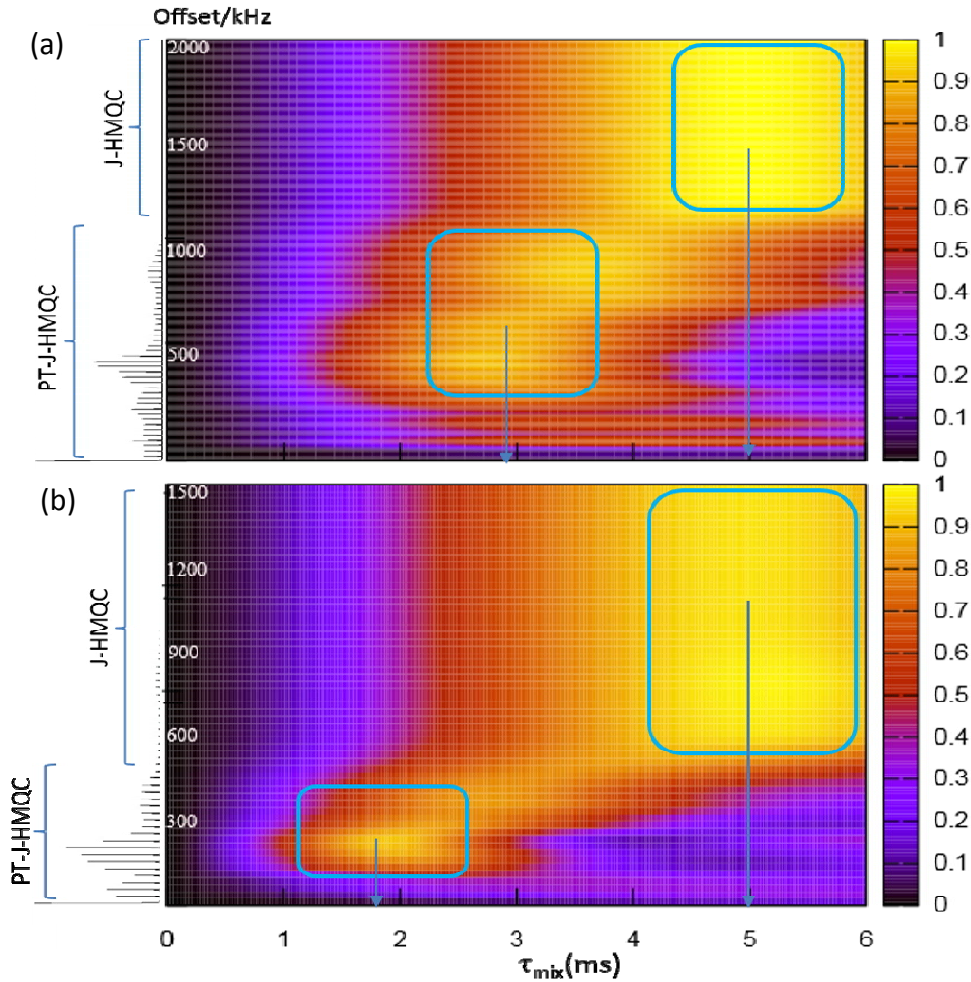
Fig.6 Simulated ^{31}P-{S} PT-J-HMQC efficiency with WURST pulses with duration of $2T_R$ each, versus τ_{mix} = 0 to 6 ms ($1/2J$ = 5 ms) and offset, with B_0 = 9.4 T, ν_R = 25 kHz, J = 100 Hz, and η_Q = 0. (a) ^{31}P-{^{23}Na} and ν_{offset} = 0 to $6\nu_Q$ = 2 MHz (C_Q = 2 MHz), ν_{RF} = 30 kHz; (b) ^{31}P-{^{27}Al} and ν_{offset} = 0 to $7.5\nu_Q$ = 1.5 MHz (C_Q = 3 MHz), ν_{RF} = 10 kHz, with ν_Q = $C_Q/2I(2I-1)$. The squares on the right sides represent the classical J-HMQC regime, whereas the squares on the left display the PT-J-HMQC regime.

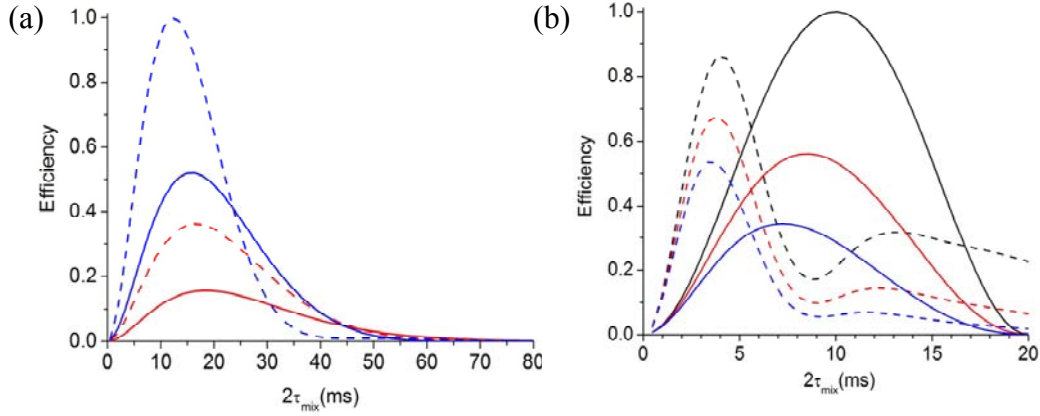Fig.7 PT-*J*-HMQC (dashed curves) and *J*-HMQC (continuous curves) built-up curves versus the total mixing time $2\tau_{mix}$, with $B_0 = 9.4$ T and $\eta_Q = 0$. (a) ^{31}P-{^{23}Na} with $C_Q = 2$ MHz, $T_{2I}' = 10$ ms, with $J = 15$ (red curves) or 30 Hz (blue curves). (b) ^{31}P-{^{27}Al} with $C_Q = 3$ MHz, J = 100 Hz, and $T_{2I}' = \infty$ (black), 16 (red), and 8 ms (blue).

However, we must emphasize that all the above simulations do not take into account the transverse relaxation time, T_{2I}'. Experimentally, one observes a signal gain, which results from a competition between the rate of transverse losses and the rate of coherence transfer. This effect is exemplified in Fig.7. In Fig. 7a, we have represented the ^{31}P-{^{23}Na} signal that can be observed versus the total mixing time, $2\tau_{mix}$. Without loss ($T_{2I}' = \infty$), its optimum value is approximately equal to 33 and 66 ms (J-HMQC) or 17 and 33 ms (PT-J-HMQC) for $J = 30$ and 15 Hz, respectively. In the case of PT-J-HMQC with $T_{2I}' = 10$ ms and $J = 30$ Hz, the attenuation remains small as the exponential term of Eq.4 remains close to 1 and equal to exp{-(S + 1/2)$J*T_{2I}'$} = 0.55. This is not the case with J-HMQC and/or smaller J coupling values (e.g. $J = 15$ Hz). In the two cases described in Fig. 7a, PT-*J*-HMQC leads to a larger signal than *J*-HMQC. In Fig. 7b, we have represented the ^{31}P-{^{27}Al} signal that can be observed with $J = 100$ Hz, versus the total mixing time. Without loss ($T_{2I}' = \infty$), the optimum time value is equal to $2\tau_{mix} \approx 10$ and 4 ms for *J*-HMQC and PT-*J*-HMQC, respectively, which correspond to our simulations. However, one observes a decrease (ca. 12%) of intensity related to the fact the saturation process is not perfect as in

Fig.3. With relaxation losses, PT-*J*-HMQC is more efficient than *J*-HMQC, and the gain increases with decreasing T_{2I}' value.

2.2.2 Experiments

NMR experiments were carried out either on a wide bore 9.4 T Bruker Avance-II spectrometer (^{31}P-{^{27}Al}), or on a narrow bore 18.8 T Bruker Avance-III spectrometer (^{27}Al-{^{17}O}). We used respectively a 4 or a 3.2 mm triple resonance MAS probe at the spinning speed of ν_R = 12.5 or 20 kHz. The saturation process was performed with a WURST-80 irradiation with a frequency bandwidth of ν_R. 2D spectra were recorded with States-TPPI mode.

In the case of ^{31}P-{^{27}Al} experiments on AlPO$_4$-HDA, Mu-4 and AlPO$_4$-14, an initial ^{1}H $\rightarrow$ ^{31}P CP transfer was used with a contact time of 3 ms and rf-fields of $\nu_{31P,CP} \approx$ 40 kHz and $\nu_{1H, CP} \approx$ 52.5 kHz (ramped). The π pulse of HMQC used an rf-field of $\nu_{31P, \pi} \approx$ 52 kHz, and the two CT selective $\pi/2$ pulse-lengths on ^{27}Al channel were of 7.5 μs ($\nu_{27Al, \pi/2} \approx$ 11 kHz). The ^{31}P resolution was enhanced by applying two simultaneous ^{1}H and ^{27}Al decoupling sequences. A SPINAL-64 ^{1}H decoupling[33], with an rf field of 75 kHz was applied at the end of the CP transfer, whereas during t$_2$ acquisition a ^{27}Al rotor-asynchronized multiple-pulse (RA-MP) decoupling[34], was also applied. RA-MP decoupling consisted of ^{27}Al pulses with rf-field strength of 40 kHz, lasting 5 μs each, and separated by windows of 83 μs. The conventional *J*-HMQC experiment was obtained by setting the WURST shape pulse amplitude to zero.

For ^{27}Al-{^{17}O} experiments, an initial WURST pulse was used on ^{27}Al channel with a length of 900 μs and an rf-field of ν_{27Al} = 16 kHz. The saturation process on ^{17}O channel was also performed with WURST with 2τ_{mix} = 7 ms. Each WURST pulse on ^{17}O channel had duration of 700 μs at rf-field of 9 kHz, and an offset of 180 kHz. The π pulse of HMQC used an rf-field of $\nu_{27Al, \pi}$ = 9 kHz, and the two CT selective

$\pi/2$ pulse-lengths on ^{17}O channel were of 10 µs ($\nu_{17O, \pi/2}$ = 8 kHz).

2.2.2.1 ^{31}P-{^{27}Al} PT-*J*-HMQC on AlPO$_4$-HDA and Mu-4 samples

^{31}P-{^{27}Al} PT-*J*-HMQC experiments were performed on AlPO$_4$-HDA[35]. This sample contains four main distinct ^{31}P crystallographic sites, which can all be well resolved with dual (^1H and ^{27}Al) decouplings (Fig. 8c). Table 1 summarizes the values of the irreversible time constant, T_{2I}', of the four ^{31}P sites. AlPO$_4$-HDA has also two different ^{27}Al sites, one tetra- (Al$_1$, δ_{iso} = 41 ppm) and one five-coordinated (Al$_2$, δ_{iso} = 14 ppm)[36].

Table 1. T_2' values of different ^{31}P sites of AlPO$_4$-HDA with ^1H decoupling

Site	P1	P2	P2	P4
T_2'(ms)	5.7	6.8	6.1	8.3

Fig. 8a shows the experimental signal intensities of ^{31}P dimension versus the total mixing time, $2\tau_{mix}$, for ^{31}P-{^{27}Al} *J*-HMQC (bottom) and PT-*J*-HMQC (top) experiments by using the pulse sequence in Fig. 1c. Each WURST pulse had a length of ca. $3T_R$ = 240 µs, and a maximal rf-field of $\nu_{RF} \approx$ 15 kHz. The offset was pre-optimized with the "(WURST)$_N$ – ($\pi/2$)$_{sel}$ – Acquire" experiment, by maximizing the CT signal, and its optimal value was of ν_{offset} = +300 kHz for our sample. In agreement with our simulations, in the presence of transverse relaxation for ^{31}P, the maximal efficiency of $^{31}P \rightarrow {}^{27}Al \rightarrow {}^{31}P$ transfer is significantly enhanced by PT-*J*-HMQC. Here the optimal mixing time remains almost the same compared to that of *J*-HMQC. Representative slices from these 2D spectra along the F$_1$ dimension are displayed in Fig. 8d. For the phosphorous impurity (star in Fig. 8c), the gain of PT-*J*-HMQC over conventional *J*-HMQC is of about 3.
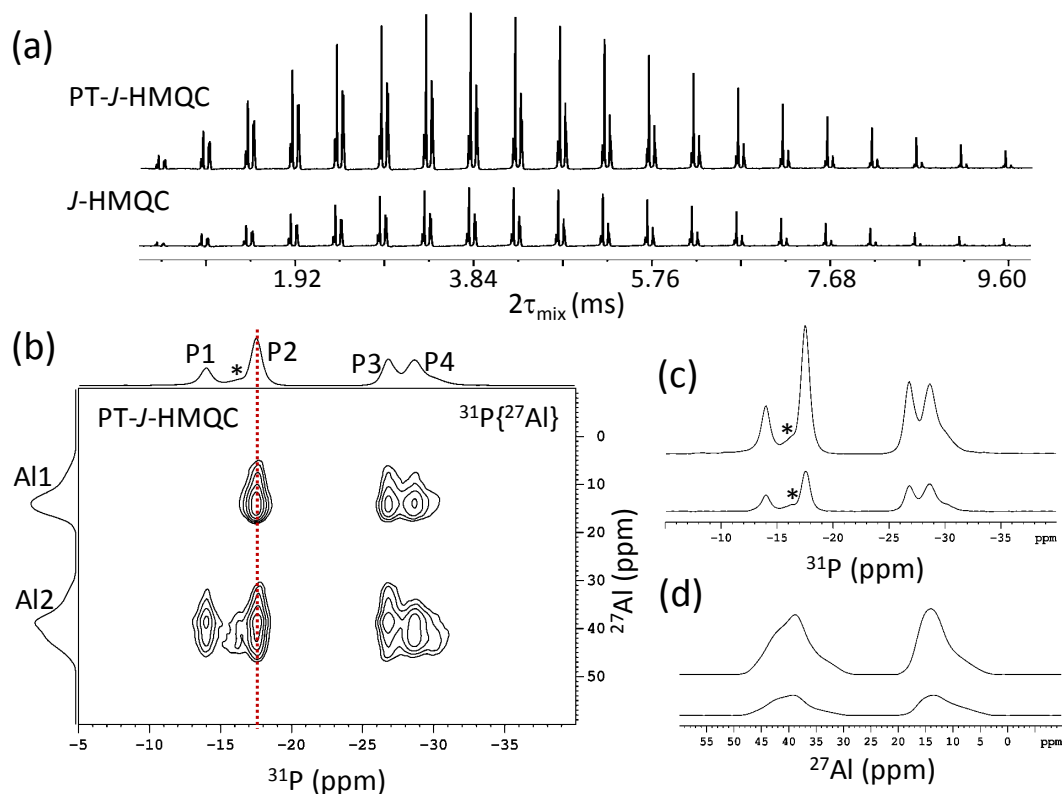
Fig.8 Experimental ^{31}P-$\{^{27}Al\}$ results on $AlPO_4$-HDA with $B_0 = 9.4$ T and $\nu_R = 12.5$ kHz. (a) ^{31}P signal intensity versus the total mixing time, $2\tau_{mix}$, for conventional J-HMQC (bottom) and PT-J-HMQC with WURST pulses of $3T_R$ each and $\nu_{RF} = 15$ kHz (top) experiments by using the pulse sequence in Fig. 1c. (b) 2D PT-J-HMQC TPPI spectrum with $2\tau_{mix} = 3.84$ ms and skyline projections along F1 and F2. TD (F1) = 100, $\Delta t_1 = 80$ μs, NS = 64, D1 = 3 s, experimental time = 5 h. (c) 1D ^{31}P spectra obtained with $^{31}P \rightarrow {}^{27}Al$ $\rightarrow {}^{31}P$ transfer obtained with conventional J-HMQC (bottom, $2\tau_{mix} = 4.32$ ms) and PT-J-HMQC (top, $2\tau_{mix} = 3.84$ ms) experiments, respectively. '*' denotes an impurity. (d) Representative slice along F1 dimension for P2 site obtained by conventional J-HMQC (bottom) and PT-J-HMQC (top) experiments.

^{31}P-$\{^{27}Al\}$ PT-J-HMQC experiments were also performed on a layered aluminophosphate, Mu-4[37,38]. This sample contains five distinct ^{31}P crystallographic sites, which can all be resolved with dual (^1H and ^{27}Al) decouplings[39] (Fig.10b). Table 2 summarizes the values of the irreversible time constant, T_2', of the five ^{31}P sites. Mu-4 has also four different ^{27}Al sites, three tetra- (Al1, Al2 and Al3) and one hexa-coordinated (Al4) sites (Fig.10c). The Al3 site at $\delta_{cs} \approx 42$ ppm possesses a very small quadrupole coupling constant ($C_Q < 0.1$ MHz), while the C_Q values of the other three Al sites are in the range of 3.3 to 4.1 MHz .

Table 2. T_2' value of different ^{31}P sites of Mu-4

Site	P1	P2	P3	P4	P5
T_2'(ms)	11.7	10.1	12.2	13.8	8.2

Fig.9 shows the experimental signal intensities of P5 and P3 sites versus 2τ for ^{31}P-$\{^{27}Al\}$ J-HMQC and PT-J-HMQC experiments. In agreement with numerical simulations, the maximal transfer efficiency is enhanced by PT, and the intensity enhancement, ξ, depends on the T_2' value: $(\xi, T_2'$ (ms)$) \approx (3, 8.2)$ and $(2, 12.2)$ for P5 and P3, respectively.
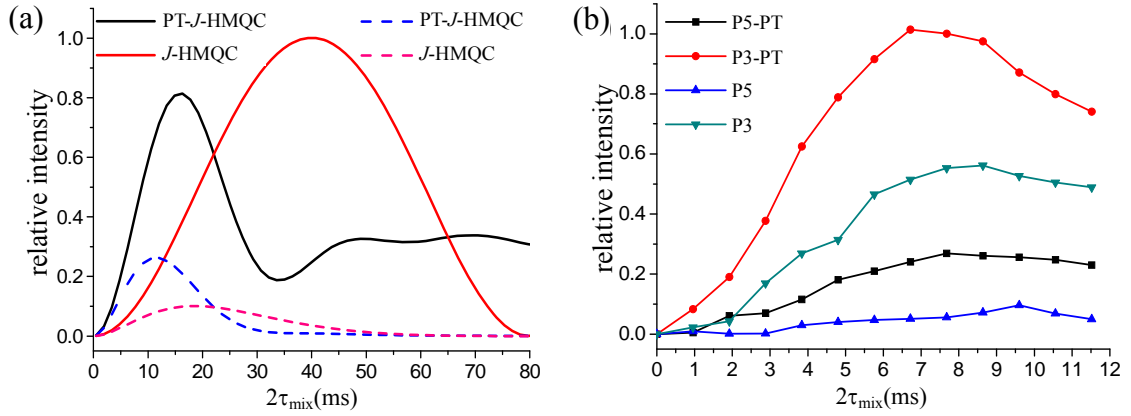

Fig.9 ^{31}P-$\{^{27}Al\}$ J-HMQC signals versus 2τ delay for $t_1 = 10$ μs at $B_0 = 9.4$ T and $\nu_R = 12.5$ kHz. (a) Transfer efficiency for an isolated ^{31}P-^{27}Al spin-pair simulated with SIMPSON software[29] for conventional J-HMQC (red lines) and PT-J-HMQC (black lines), with $J_{Al-P} = 25$ Hz, $C_Q = 4$ MHz (^{27}Al), and $T_2' \rightarrow +\infty$ (continuous lines) or $T_2' = 12$ ms (dash lines). (b) Relative experimental signal intensities for Mu-4 sample of conventional J-HMQC (P5: ▲; P3: ▼) and PT-J-HMQC (P5: ■; P3: ●). The experimental intensities are normalized with respect to the maximal one, obtained for P5 site in PT-J-HMQC experiment with $2\tau = 6.5$ ms.

Fig. 10 shows the conventional J-HMQC and PT-J-HMQC ^{31}P-$\{^{27}Al\}$ 2D spectra. The same cross-peaks are clearly observed in the two spectra. This agreement indicates that the PT-J-HMQC experiment provides reliable structural information. Representative slices from these 2D spectra along the F_1 dimension are displayed in

Fig.11. For the P5 slice (Fig.11a), the gain of PT-*J*-HMQC over conventional *J*-HMQC is about 5. For the P3 slice (Fig.11b), the enhancement is about 3, except for the Al3 site. The smaller enhancement for P3 slice compared to P5 one stems from a difference in T_2' values between these two sites (see Table 2). As a general rule, the enhancement increases inversely to the T_2' value. There is no gain for Al3 site owing to its quasi-symmetrical surrounding ($C_Q < 0.1$ MHz), and the STs of Al3 site remain unaffected by the WURST irradiation at large offset.
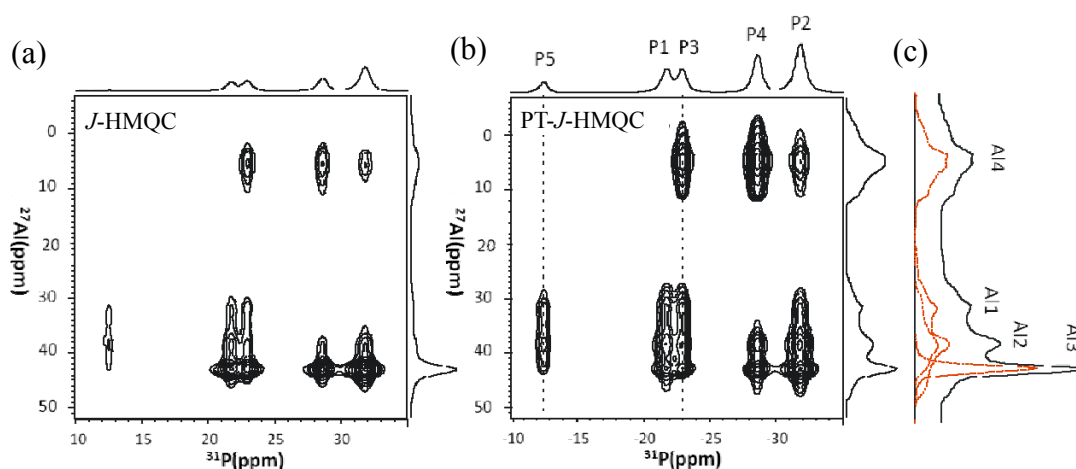
Fig.10 2D ^{31}P-{^{27}Al} *J*-HMQC spectra of Mu-4 sample recorded at B_0 = 9.4 T and ν_R = 12.5 kHz, with (a) conventional *J*-HMQC and 2τ = 5.12 ms, and (b) PT-*J*-HMQC and 2τ = 3.84 ms, and skyline projections along F_1 and F_2. (c) 1D ^{27}Al MAS spectrum of Mu-4 sample (right, black real line) and simulated four different ^{27}Al sites (left, red dash lines) derived from the 2D 3QMAS spectrum.
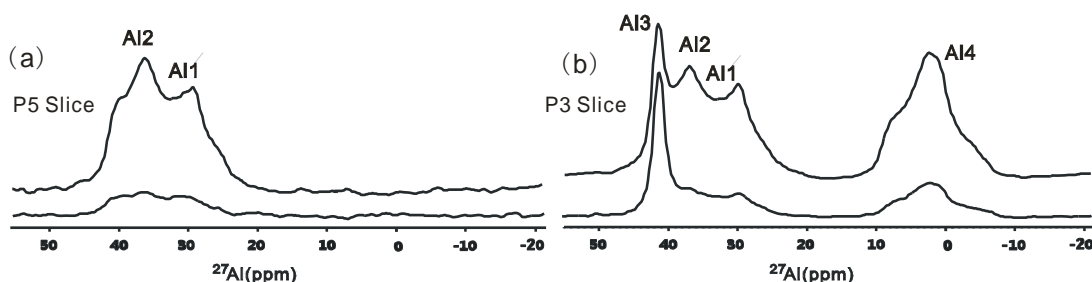
Fig.11 Representative slices along (a) P5 and (b) P3 sites from the ^{31}P-{^{27}Al} *J*-HETCOR spectra of Mu-4 sample along the F_1 dimension obtained by conventional *J*-HMQC (bottom) and PT-*J*-HMQC (top) experiments.

2.2.2.2 PT-*J*-HMQC for two half-integer quadrupolar species on Al₂O₃ sample

Although considerable progress has been made in the development of SSNMR methods, the investigation of connectivity or proximity between homo-[40-46] or hetero-[47-49] quadrupolar spins still remains a longstanding challenge. This is the case for two different half-integer quadrupolar isotopes, for which only very few 2D correlation experiments have been introduced. Nevertheless, it has already been demonstrated that *J*-HMQC could lead to an HETCOR spectrum correlating the CTs of ^{27}Al and ^{17}O, which were directly and indirectly observed, respectively[48,50].
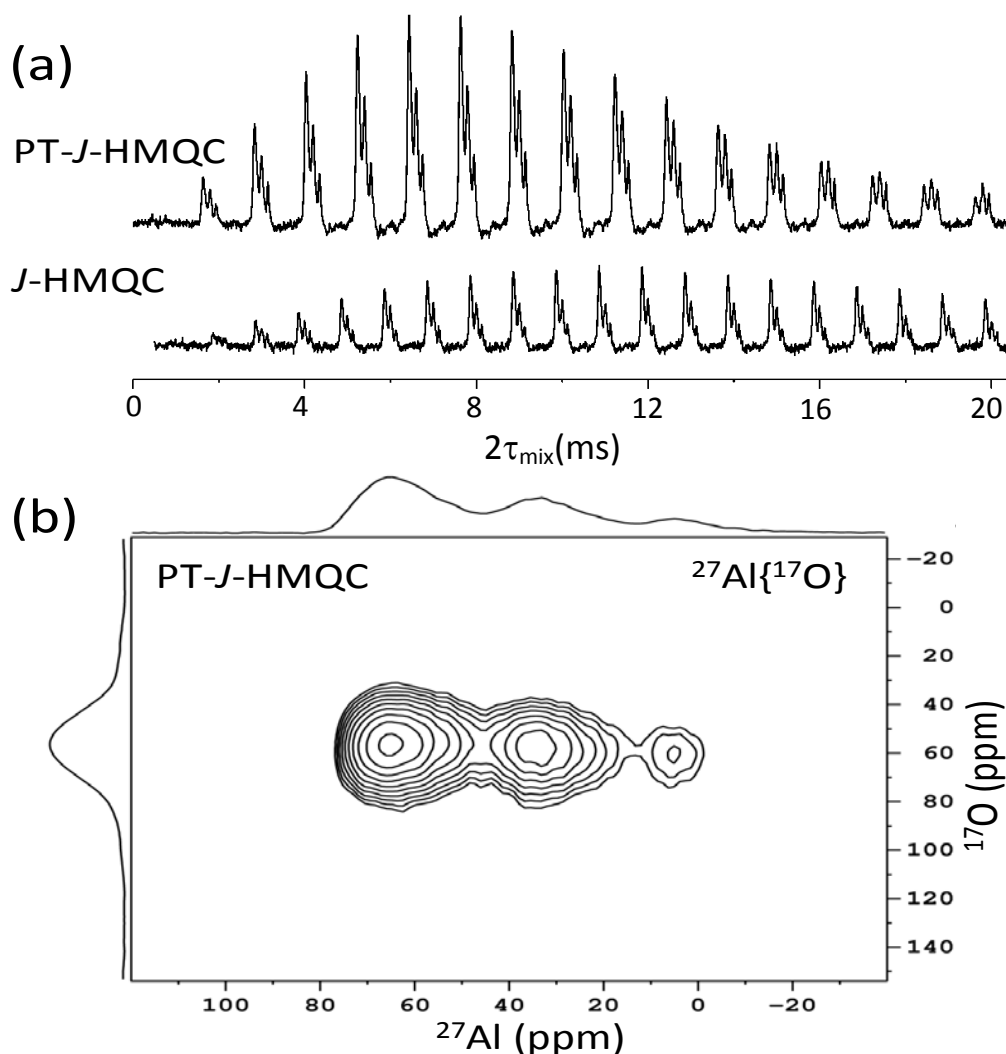
Fig.12 Experimental ^{27}Al-$\{^{17}$O$\}$ results on γ-Al₂O₃ with $B_0 = 18.8$ T, $\nu_R = 20$ kHz, and π/2 and π CT-selective pulses with $\nu_{27Al} = 9$ kHz and $\nu_{17O} = 8$ kHz. (a) ^{27}Al signal intensity versus the total mixing time, $2\tau_{mix}$, for conventional *J*-HMQC (bottom) and PT-*J*-HMQC with WURST pulses of 700 μs each and $\nu_{RF} = 9$ kHz (top) experiments by using the pulse sequence in Fig. 1c. (b) 2DPT-*J*-HMQC spectrum with $2\tau_{mix} = 7$ ms and skyline projections along F1 and F2. TD(F1) = 12, $\Delta t_1 = 50$ μs, NS = 4096, D1 = 0.5 s, experimental time = 6.5 h.

Here, we show that the population transfer strategy is also available for two half-integer quadrupolar isotopes, such as [27]Al and [17]O. Fig. 12a displays the [27]Al experimental signal intensities after a [27]Al $\rightarrow$ [17]O $\rightarrow$ [27]Al transfer versus the total mixing time, $2\tau_{mix}$, for [27]Al-{[17]O} J-HMQC (bottom) and PT-J-HMQC (top) using the sequence described in Fig. 1b. The Al_2O_3 sample, a pure ordered mesoporous alumina, was prepared as described in Ref. 51. Except for the WURST irradiations sent on the [17]O and [27]Al channels, all pulses selectively excited the CTs. The maximum transfer efficiency was significantly enhanced with a gain of 3 by PT-J-HMQC. Moreover, the optimal mixing time of PT-J-HMQC was shortened by a factor of ca. 2 compared to that of J-HMQC. The remarkable enhancement of efficiency and the decrease of optimal mixing time are both related to the relatively weak J coupling between [27]Al and [17]O spins, and the fast transverse relaxation rates of [27]Al. The 2D [27]Al-{[17]O} PT-J-HMQC spectrum of Al_2O_3 is shown in Fig. 12b, which demonstrates that PT-J-HMQC can also provide reliable structural information even between two half-integer quadrupolar isotopes.

2.2.2.3 [31]P-{[27]Al} PT-D-HMQC on APO4-14 sample

In fact, the strategy of population transfer of satellite transitions can also be employed on D-HMQC experiments by only adding a heteronuclear dipolar recoupling sequence on I spin-1/2 channel, as shown in Fig.1. Continuous saturation is applicable for D-HMQC experiment since the WURST pulses are applied on the S

Fig. 13a shows the experimental signal intensities of ^{31}P dimension versus the total mixing time, $2\tau_{mix}$, for [31]P-{[27]Al} D-HMQC (bottom) and PT-D-HMQC (top) experiments on APO_4-14 sample by using the pulse sequence in Fig. 1c with $SR4_1^2$ dipolar recoupling[5,6]. In this case, the optimum dipolar recoupling time is short compared to T_2', [31P] values that are in the range of 7-10 ms on this $AlPO_4$-14 sample. However, one still observes experimentally a 2-fold shortening of the optimum

mixing time. This accelerated recoupling transfer will be very useful for the investigation of either long-range distances, or difficult samples including paramagnetic materials that often exhibit very short T_{2I}' values. The ^{31}P-$\{^{27}Al\}$ PT-*D*-HMQC 2D spectrum is shown in Fig. 13b.
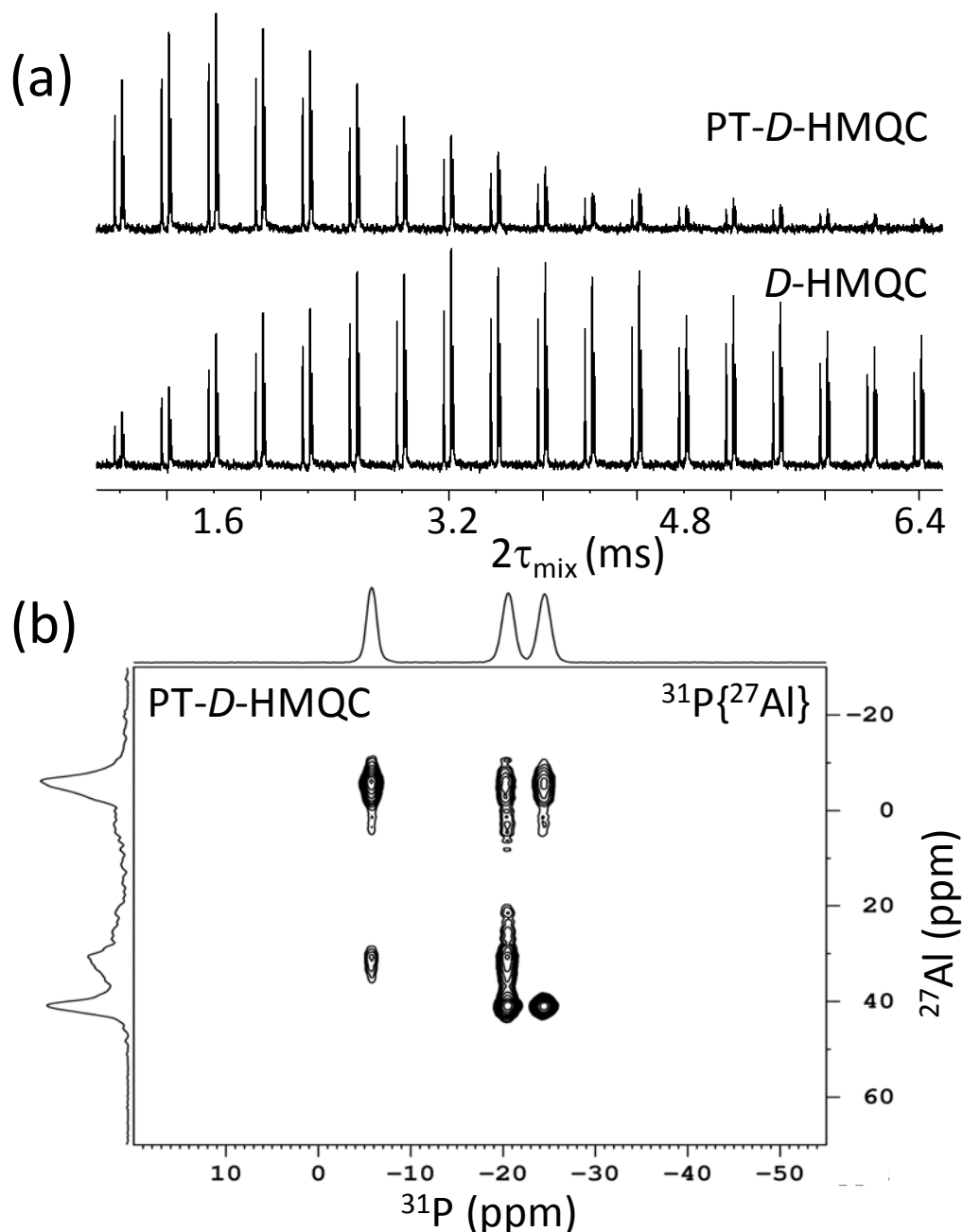
Fig.13 Experimental ^{31}P-$\{^{27}Al\}$ results on $AlPO_4$-14 with B_0 = 9.4 T, ν_R = 12.5 kHz, and $\pi/2$ CT-selective pulses with ν_{27Al} = 11 kHz. (a) ^{31}P signal intensity versus the total mixing time, $2\tau_{mix}$, for conventional *D*-HMQC (bottom) and PT-*D*-HMQC with WURST pulses of $2T_R$ each and ν_{RF} = 8 kHz (top) experiments by using the pulse sequence in Fig. 1c. (b) 2D PT-*D*-HMQC spectrum with $2\tau_{mix}$ = 1.6 ms, TD(F1) = 200, Δt_1 = 80 μs, NS = 64, D1 = 1 s, experimental time = 3.5 h.

2.3 Improve Methods of PT-*J*-HMQC

Fig. 14 shows the limitation of PT-*J*-HMQC using WURST shape pulse. This simulations were also performed for an isolated ^{27}Al-^{31}P (5/2-1/2) spin-pair with J = 100 Hz. The quadrupolar parameters of ^{27}Al were (C_Q, η_Q) = (3 MHz, 0) and this interaction was considered to the second order. The simulated efficiency for ^{31}P-{^{27}Al} PT-*J*-HMQC is displayed in Fig. 14a (red plot) versus the offset of WURST. This curve exhibits a profile analogue to that of ^{27}Al satellite transition MAS spectrum (Fig. 14a, bottom), except for the frequency region with small offset irradiation ($|\nu_{offset}| \leq$ 100 kHz) where there is a severe interference between the WURST irradiation and the CT population. Fig. 14b shows the optimization of offset value in small steps over a range of ν_R, with the center corresponding to the "horn" (the most intense region) of the ST envelope at +200kHz. The result indicates the efficiency of PT-*J*-HMQC is not identical when the offset value changes in a range of ν_R, from 0.55 to 1. It means it is impossible to enhance sites of different offset with the same factor in a sample. To solve this problem, we focus on the pulse with multiple sweeps.

(a)   (b)
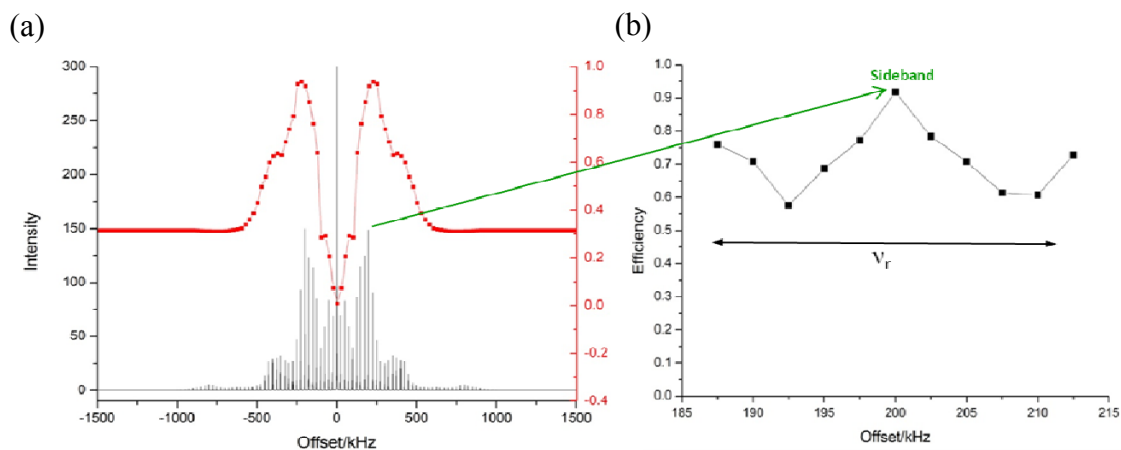
Fig.14 (a) Simulated PT-*J*-HMQC transfer efficiency of ^{31}P $\rightarrow$ ^{27}Al $\rightarrow$ ^{31}P obtained by applying several times the WURST pulse during τ_{mix} = 1/[2(S+1/2)J] = 1/6J = 1.67 ms, versus the offset of WURST irradiation with ν_{RF} = 10 kHz (top), and the corresponding ^{27}Al satellite transitions (ST1 + ST2) MAS spectrum at the bottom. C_Q = 3 MHz, η_Q = 0, B_0 = 9.4 T, ν_R = 25 kHz, J = 100 Hz. The efficiency has been normalized with respect to its maximum observed for $\nu_{RF} \approx$ 7 kHz. Each WURST pulse had duration of 2T_R. (b) Zoom around offset at 200 kHz, using small steps with ν_R /10 = 2.5 kHz

2.3.1 Simulations

2.3.1.1 Double sweeps pulse

The same as PT-J-HMQC using WURST, we have done simulations with DFS at first. Double Frequency Sweeps (DFS) is a shape pulse irradiating at two frequencies. As shown in Fig.15a, for a narrowband DFS, the two sweeps are symmetrical with sweep range of ν_R. In Fig. 16a, the ^{31}P-$\{^{27}Al\}$ PT-J-HMQC efficiency with DFS manipulations has been calculated versus τ_{mix} and offset. The duration of basic element is $2T_R$, the same as that in PT-J-HMQC with WURST. The coherence transfer rate of PT-J-HMQC is still accelerated by a factor of slightly less than three, but the optimal area is larger than that using WURST (Fig. 16a, square frame). We have also represented in Fig. 16b the efficiency versus rf-amplitude and offset ($\tau_{mix} = 2$ ms). It shows, to get the optimum efficiency, a small offset needs small rf-amplitude, and a large offset needs large rf-amplitude (two square frames).
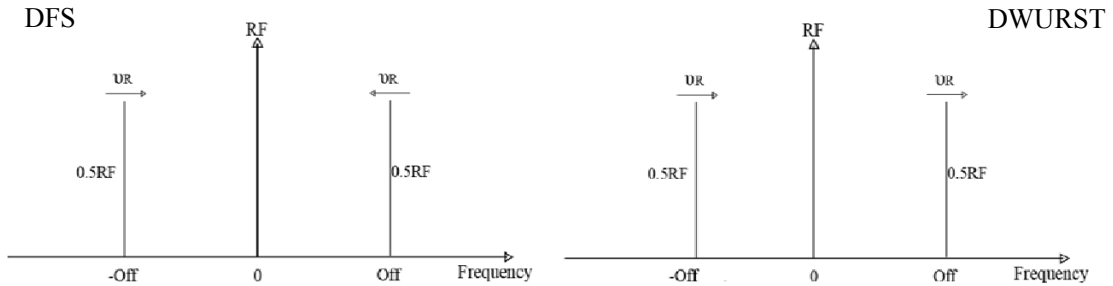
Fig.15 Schematic representation of double sweeps pulses irradiating at two symmetrical frequencies with the range of ν_R. (a) DFS : the directions of the two sweeps are opposite. (b) DWURST : the directions of the two sweeps are identical

Then we have introduced a new method, called DWURST (Double WURST), in Fig. 15b. The difference between DFS and DWURST is the directions of the sweeps. In DFS, the directions of the two sweeps are opposite, to ensure the symmetry of the pulse. However, in DWURST, the directions of the two sweeps are same. It means the sweep order of this pulse at two symmetrical offsets is identical, sweeping ST_1 first, ST_2 next (from the inner STs to the outer STs) or ST_2 first, ST1 next (from the outer

STs to the inner STs). The simulation results of efficiency versus τ_{mix} versus offset and efficiency versus offset versus rf-amplitude for PT-J-HMQC using DWURST are more or less the same with those using DFS, shown in Fig.16.

(a)   (b)

Fig.16 (a) Simulated ^{31}P-$\{^{27}$Al$\}$ PT-J-HMQC efficiency with double sweeps pulses with duration of 2T$_R$ each, versus τ_{mix} = 0 to 6 ms (1/2J = 5 ms) and offset, with B$_0$ = 9.4 T, ν_R = 25 kHz, J = 100 Hz, and η_Q = 0, C$_Q$ = 3 MHz. The square on the left displays the PT-J-HMQC regime. (b) Efficiency verus offset and rf-amplitude, during τ_{mix} = 1/[2(S+1/2)J] = 1/6J = 1.67 ms, The squares represent PT-J-HMQC regime.

2.3.1.2 Quadruple sweeps pulse

According to the previous results, a small offset needs small rf-amplitude, and a large offset needs large rf-amplitude, we have introduced new methods using quadruple sweeps. First QFS (quadruple frequency sweep) irradiates at four frequencies, represented in Fig. 17a. All of these four sweep directions are symmetrical, with sweep range of ν_R. When the offset is double, the rf-amplitude is 4 times. In Fig. 18a, the ^{31}P-$\{^{27}$Al$\}$ PT-J-HMQC efficiency with QFS manipulations has been calculated versus τ_{mix} and offset, with basic element duration of 2T$_R$. The coherence transfer rate of PT-J-HMQC is still accelerated by a factor of slightly less than three, but the optimal area (square frame) is much larger than those using previous methods (DFS, DWURST, WURST). The optimum offset range is from $\pm$ 200kHz to $\pm$900kHz. We have also represented in Fig. 18b the efficiency versus rf-amplitude and offset (τ_{mix} = 1.67 ms). It also shows a larger optimum area (circle frame).
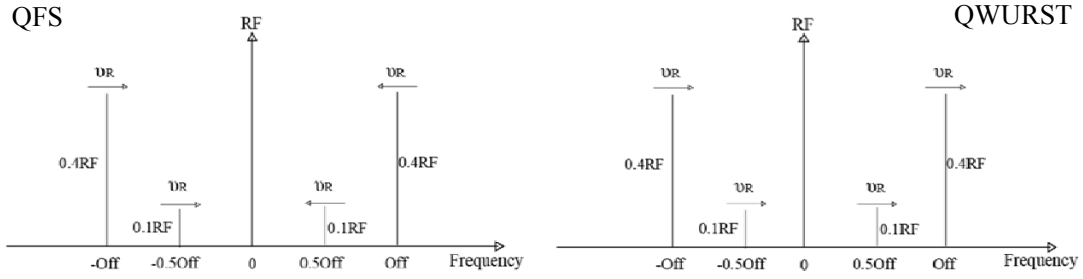
Fig.17 Schematic representation of quadruple sweeps pulses irradiating at four symmetrical frequencies with the range of ν_R. When the offset is double, the rf-amplitude is 4 times. (a) QFS : the directions of the four sweeps in the two sides are opposite. (b) QWURST : the directions of the four sweeps are identical

Then we have introduced a new method again, called QWURST (Quadruple WURST), in Fig. 17b. The difference between QFS and QWURST is the direction of the sweeps. In QWURST, the directions of the four sweeps are same to ensure the identical sweep order: ST_1 first, ST_2 next (from the inner STs to the outer STs) or ST_2 first, ST_1 next (from the outer STs to the inner STs). The simulation results of efficiency versus τ_{mix} versus offset and efficiency versus offset versus rf-amplitude for PT-J-HMQC using QWURST are more or less the same with those using QFS, as shown in Fig.18.
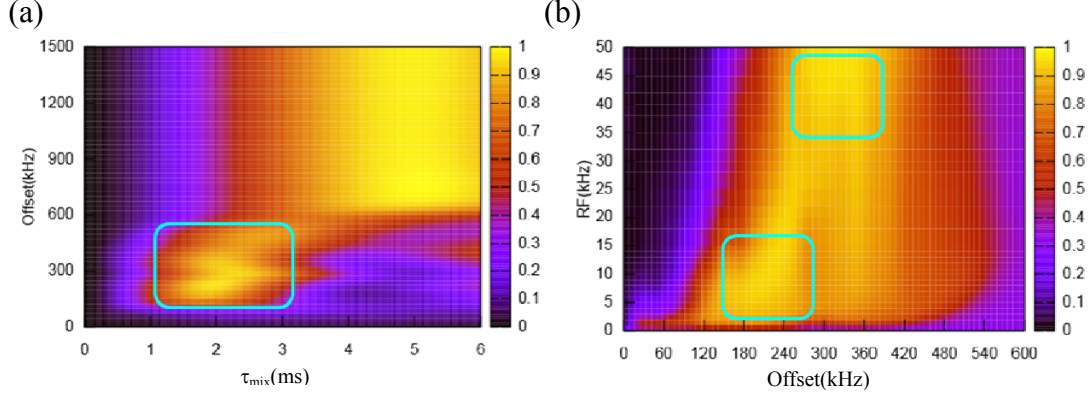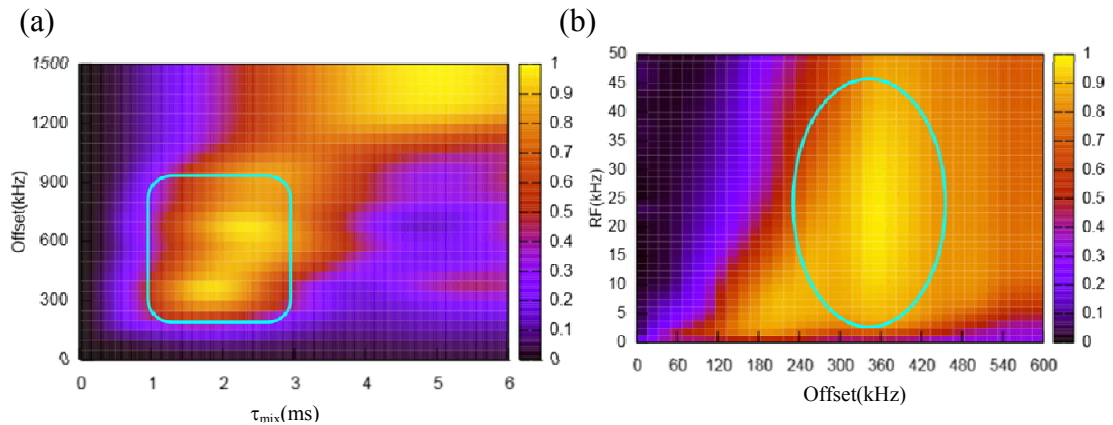

Fig.18 (a) Simulated ^{31}P-$\{^{27}$Al$\}$ PT-J-HMQC efficiency with quadruple sweeps pulses with duration of $2T_R$ each, versus $\tau_{mix} = 0$ to 6 ms ($1/2J = 5$ ms) and offset, with $B_0 = 9.4$ T, $\nu_R = 25$ kHz, J = 100 Hz, and $\eta_Q = 0$, $C_Q = 3$ MHz. The square on the left displays the PT-J-HMQC regime. (b) Efficiency verus offset and rf-amplitude, during $\tau_{mix} = 1/[2(S+1/2)J] = 1/6J = 1.67$ ms. The circle represent PT-J-HMQC regime.

The most important point is the dependence of offset for each method. As what we have done for PT-J-HMQC with WURST, Fig. 19 shows the optimization of offset value in small step over a range of ν_R. The efficiencies of quadruple sweeps pulses (QFS, QWURST) are more stable than those of double sweeps pulse (DFS, DWURST).
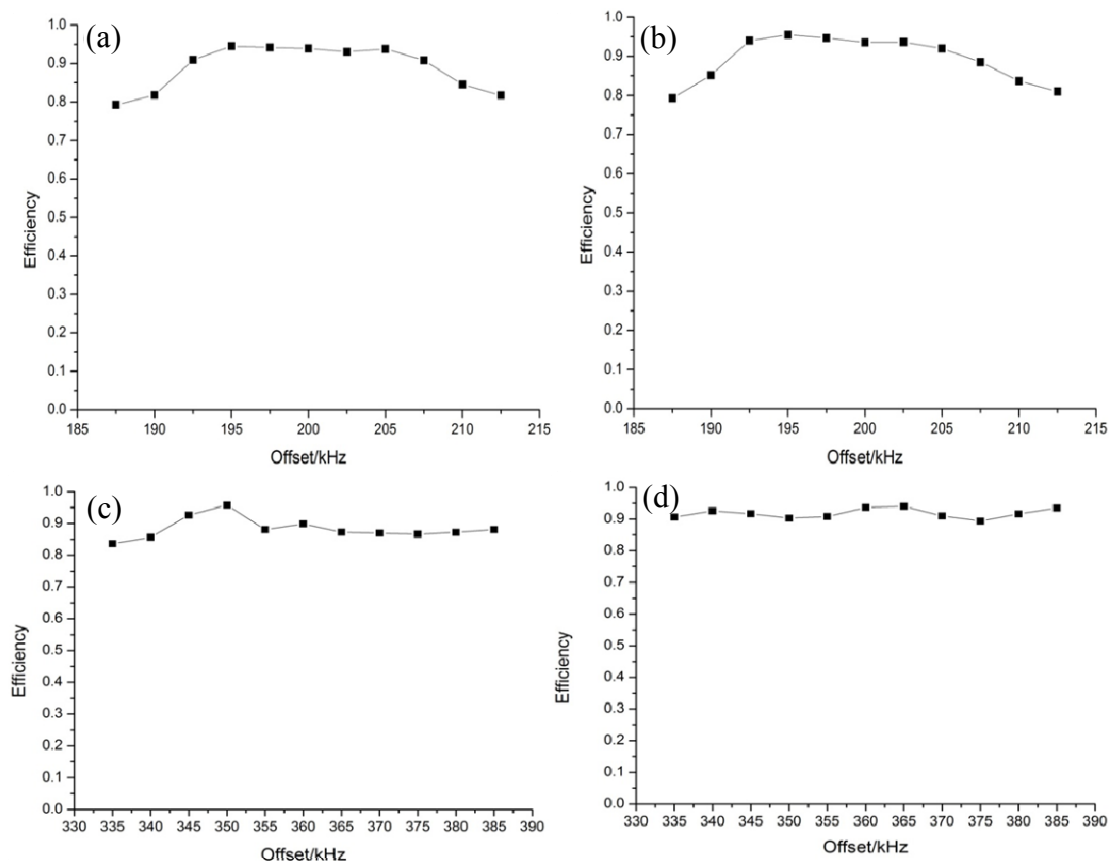
Fig.19 Simulated ^{31}P-$\{^{27}$Al$\}$ PT-J-HMQC efficiency versus offset with different pulses with duration of $2T_R$ each,, with $B_0 = 9.4$ T, $\nu_R = 25$ kHz, J = 100 Hz, and $\eta_Q = 0$, $C_Q = 3$ MHz, $\tau_{mix} = 1/[2(S+1/2)J] = 1/6J = 1.67$ ms, (a) DFS, (b) DWURST, (c) QFS,(d) QWURST.

2.3.2 Experiments

NMR experiments were carried out on a wide bore 9.4 T Bruker Avance-II spectrometer (^{31}P-$\{^{27}$Al$\}$). We used a 3.2 mm triple resonance MAS probe at the spinning speed of $\nu_R = 15$ kHz.

In the case of ^{31}P-$\{^{27}$Al$\}$ experiments on Berlinite and AlPO$_4$-14, The π pulse of HMQC used an rf-field of $\nu_{31P, \pi} \approx 52$ kHz, and the two CT selective $\pi/2$ pulse-lengths

on ^{27}Al channel were of 7.5 μs ($\nu_{27Al, \pi/2} \approx 11$ kHz). The ^{31}P resolution was enhanced by applying a simultaneous ^{27}Al decoupling sequence. During t_2 acquisition a ^{27}Al rotor-asynchronized multiple-pulse (RA-MP) decoupling, was applied. RA-MP decoupling consisted of ^{27}Al pulses with rf-field strength of 40 kHz, lasting 5 μs each, and separated by windows of 83 μs. The conventional *J*-HMQC experiment was obtained by setting the shape pulse amplitude to zero.

For Berlinite, we used the pulse in Fig. 1b. For AlPO$_4$-14, as shown in Fig. 1c, an initial ^{1}H $\rightarrow$ ^{31}P CP transfer was used with a contact time of 3 ms and rf-fields of $\nu_{31P,CP} \approx 40$ kHz and $\nu_{1H, CP} \approx 52.5$ kHz (ramped). A SPINAL-64 ^{1}H decoupling, with an rf field of 75 kHz was applied at the end of the CP transfer.

2.3.2.1 Experiments for Berlinite sample

At first, we performed a "(Shape Pulse) − ($\pi/2$)$_{sel}$ − Acquire" experiment, and obtained the 1D spectra, shown in Fig.20. Using the same pulse length, the offset and rf-amplitude for each mehod are shown in Table.3. These four methods have similar intensity enhancement at a factor of ca. 3. Then in Fig.21, we have optimized the offset with small steps. For double sweeps pulses (DFS and DWURST), we optimized offset from 170 to 200kHz with 1 kHz increment. For quadruple sweeps pulses (QFS and QWURST), we optimized offset from 340 to 400kHz with 2 kHz increment. The results show QFS is the most stable method, without offset dependence.

Table.3 Rf-amplitude and offset value of different pulse

Pulse	DFS	DWURST	QFS	QWURST
rf-amplitude/kHz	23.5	26.4	33	26.4
Offset/kHz	300	300	374	354
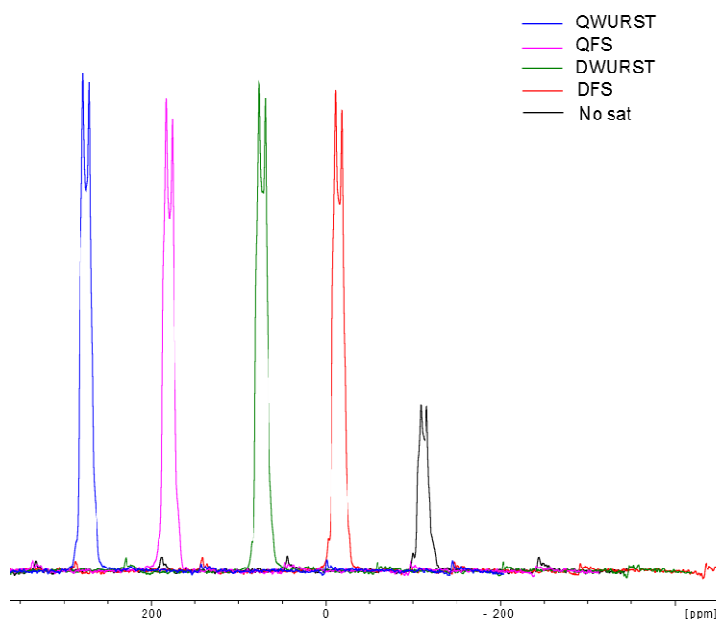
Fig.20 1D experimental results for ^{27}Al results on Berlinite with B_0 = 9.4 T, ν_R = 15 kHz, the shape pulse length is 500us, using DFS/DWURST/QFS/QWURST. "No sat" means conventional *J*-HMQC without STs saturation.

Fig.21 Offset dependence for ^{27}Al results on Berlinite with B_0 = 9.4 T, ν_R = 15 kHz, the shape pulse length is 500us, using DFS/DWURST/QFS/QWURST.

At last we represented in Fig. 22 the signal intensities of ^{31}P dimension versus the total mixing time, $2\tau_{mix}$, of the ^{31}P-$\{^{27}$Al$\}$ experiments. The parameters of shape pulses are from previous 1D experiments. The basic element of each pulse is 500 μs.

The optimum $2\tau_{mix}$ value for PT-*J*-HMQC is at about 5ms, while conventional J-HMQC is at 12ms, the coherence transfer speeds up 2-3 folds.
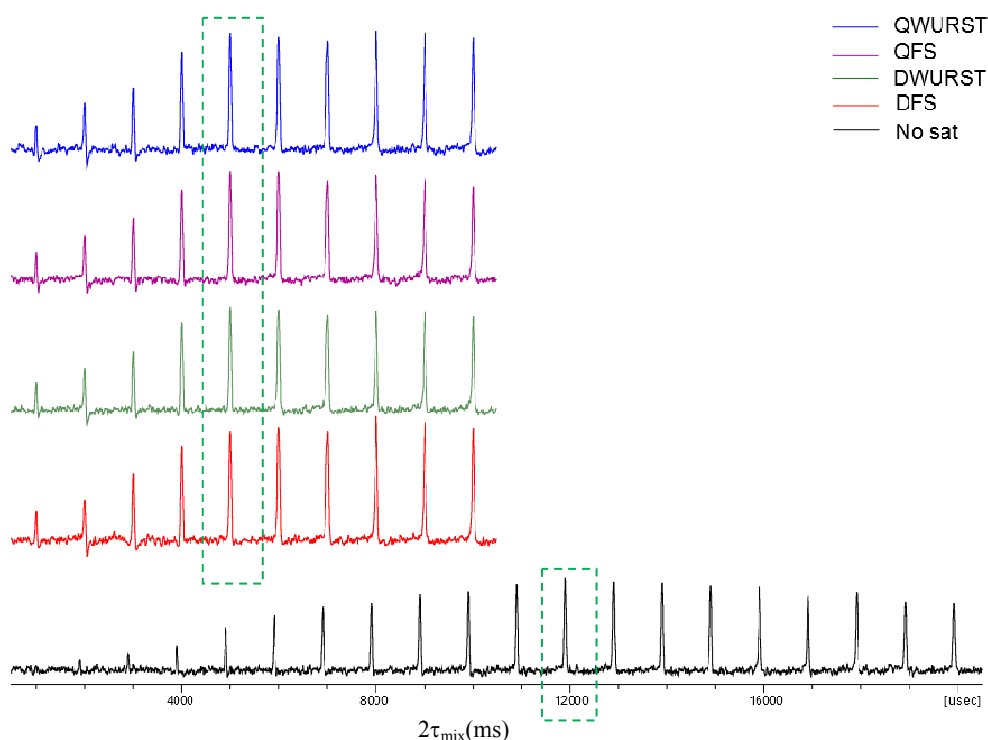
Fig.22 Experimental ^{31}P-$\{^{27}$Al$\}$ results on Berlinite with B_0 = 9.4 T and ν_R = 15 kHz. ^{31}P signal intensity versus the total mixing time, $2\tau_{mix}$, for conventional *J*-HMQC (bottom) and PT-*J*-HMQC with different pulse: DFS/DWURST/QFS/QWURST.

2.3.2.2 Experiments for AlPO₄-14 sample

Since there is only one ^{27}Al site in Berlinite, it is difficult to check the different effect between double sweeps and quadruple sweeps pulses. So we have used another sample: AlPO₄-14, containing four ^{27}Al sites with different C_Q, shown in Table.4.

Table 4. C_Q value of different ^{27}Al sites of AlPO₄-14

Site	Al(3)	Al(2)	Al(1)	Al(4)
δ/ppm	40.7	31.7	4.6	-5.9
C_Q/MHz	1.75	4.15	5.66	2.60

At first, we also performed a "(Shape Pulse) – $(\pi/2)_{sel}$ – Acquire" experiment, and obtained the 1D spectra, shown in Fig.23. The offset and rf-amplitude for each one are shown in Table.5. The Al3 site with the smallest C_Q can only be enhanced effectively by QFS and QWURST, while the other three sites with large C_Q can be enhanced by each method. It indicates quadruple sweeps are more efficient for sample with different sites of different C_Q value.

Table.5 Rf-amplitude and offset value of different pulse

Pulse	DFS	DWURST	QFS	QWURST
rf-amplitude/kHz	23.5	26.4	26.4	26.4
Offset/kHz	300	300	300	354
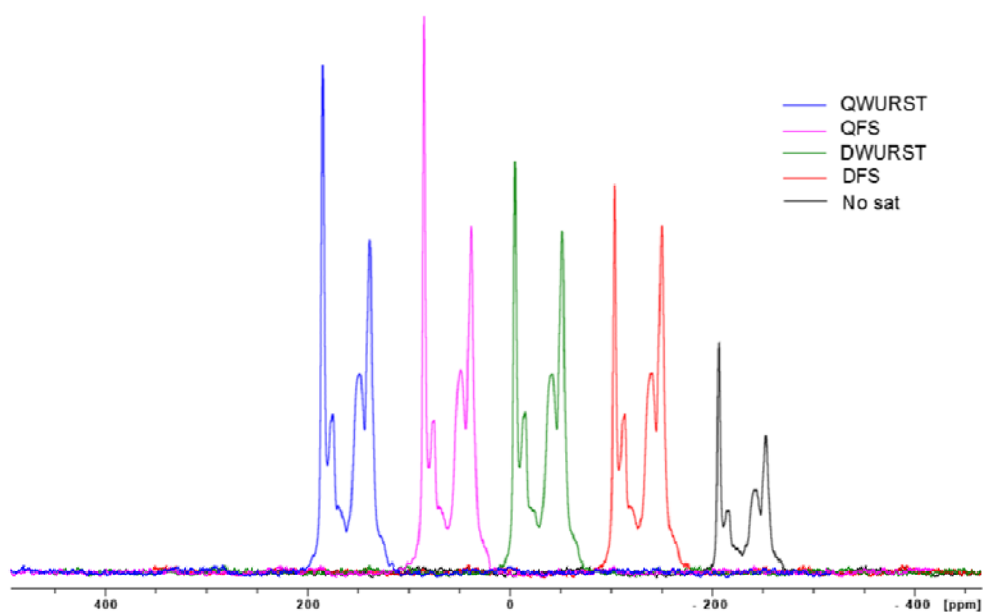
Fig.23 1D experimental results for ^{27}Al results on AlPO$_4$-14 with B$_0$ = 9.4 T, ν_R = 15 kHz, the shape pulse length is 500us, using DFS/DWURST/QFS/QWURST. "No sat" means conventional J-HMQC without STs saturation.

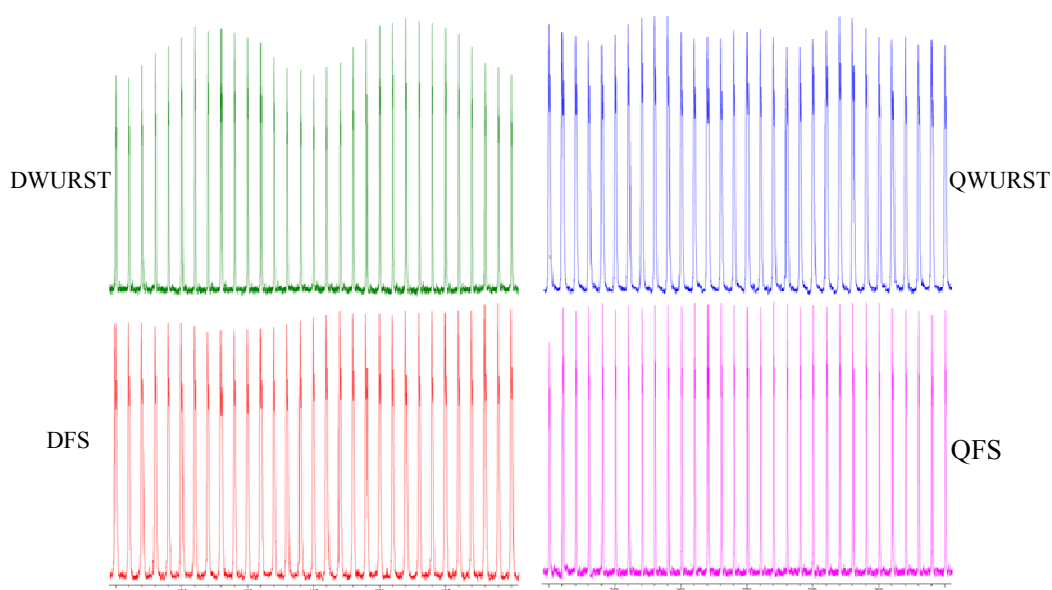Then we represented in Fig.24a the experimental signal intensities of ^{31}P dimension versus the total mixing time, $2\tau_{mix}$, of the ^{31}P-{^{27}Al} experiments. The optimum $2\tau_{mix}$ value for PT-J-HMQC with QFS is at about 6 ms, while conventional

J-HMQC is at 10 ms. All the shape pulse parameters are from the 1D experiments. Fig.24b shows the comparison of signal intensities between PT-*J*-HMQC and conventional *J*-HMQC. The enhancement factor is ca. 2.
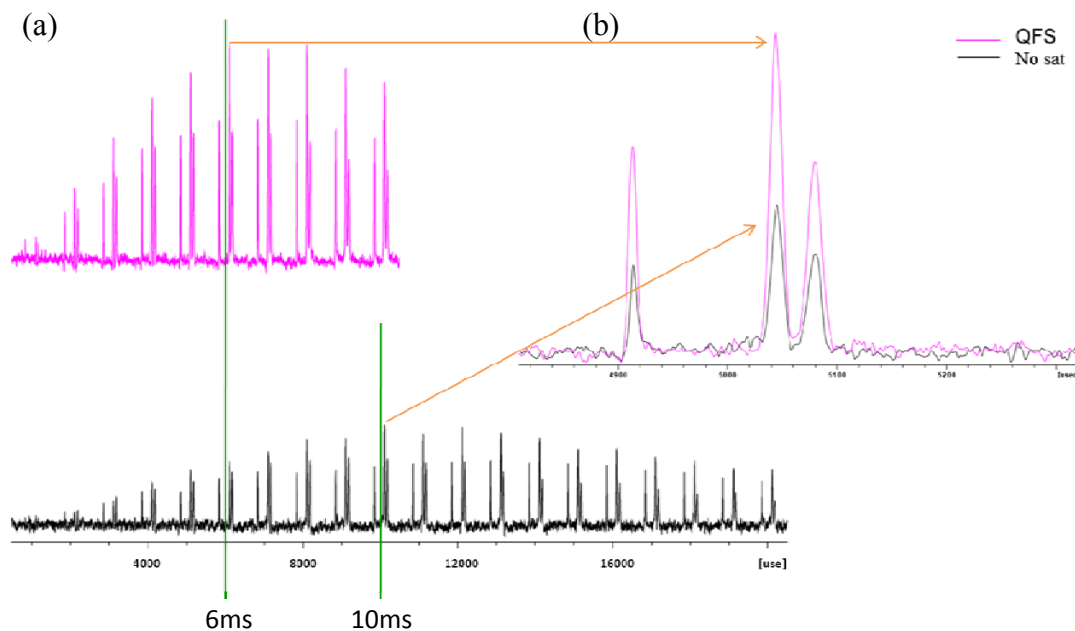
Fig.24 Experimental ^{31}P-$\{^{27}$Al$\}$ results on AlPO$_4$-14 with B$_0$ = 9.4 T and ν_R = 15 kHz. (a) ^{31}P signal intensity versus the total mixing time, $2\tau_{mix}$ for conventional *J*-HMQC (bottom) and PT-*J*-HMQC with QFS pulses of 500 µs for each basic element. (b) ^{31}P intensity comparison with conventional *J*-HMQC (bottom, $2\tau_{mix}$ = 10 ms) and PT-*J*-HMQC (top, $2\tau_{mix}$ = 6 ms).
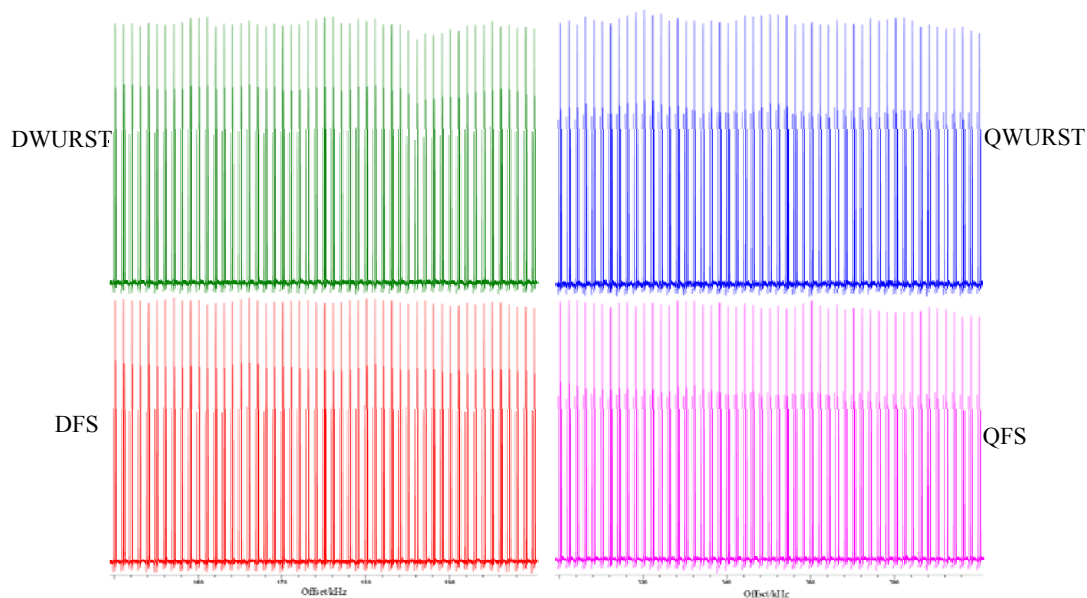
Fig.25 Offset dependence of ^{31}P-$\{^{27}$Al$\}$ experiments on AlPO$_4$-14 with B$_0$ = 9.4 T, ν_R = 15 kHz, using DFS/DWURST/QFS/QWURST. The basic element of each shape pulse length is 500 us, $2\tau_{mix}$ = 6 ms,

At last, we have optimized the offset with small steps for the four methods. For double sweeps pulses (DFS and DWURST), we optimized offset from 150 to 200kHz with 1 kHz increment. For quadruple sweeps pulses (QFS and QWURST), we optimized offset from 300 to 400kHz with 2 kHz increment. It is very interesting that with the mixture of different [27]Al with different offsets, there is no modulation for the mixture of ^{31}P signals for any method, as shown in Fig.25.

2.4 Conclusion

In summary, we have shown the advantages of PT-*J*/*D*-HMQC experiments for the indirect observation of half-integer quadrupolar nuclei in solids. We have shown by numerical simulations that the manipulation of the populations of satellite transitions efficiently accelerates the coherence transfer between the two isotopes. The continuous saturation strategy for population transfer can accelerate the coherence transfer rate by a factor of up to ca. (S+1/2). Experimentally, this acceleration decreases the losses, which improves the efficiency of the *J*-HMQC transfer when T_{2I}' ≤ 1/*J*. We also demonstrate that this strategy allows enhancing the sensitivity of *J*-HMQC experiments between two half-integer quadrupolar isotopes (e.g. [27]Al-[17]O). Moreover, we show that this concept can also be applied to dipolar-mediated experiments (*D*-HMQC). Indeed, although this concept does not lead to a [31]P-{[27]Al} signal gain on our $AlPO_4$-14 sample, a 2-fold shortening of the optimum mixing time was still observed. This time reduction will be very useful to analyze long-range distances, or paramagnetic materials.

We also improve the population transfer method, according to the DFS method, we introduce three new ones, double sweep (DWURST) and quadruple sweeps (QFS, QWURST). The quadruple sweeps are more robust for small C_Q, and above all, QFS is the most stable and efficient sequence.

We believe that these new approaches will be very beneficial for a wide range of

organic, inorganic and even biological materials containing half-integer quadrupolar nuclei, and will provide detailed insight into their structure-property relationship.

References

[1] E.O. Stejskal, J. Schaefer, J.S. Waugh, *J. Magn. Reson.*, **28** (1), 105-112 (1977).

[2] A.W. Hing, S. Vega, J. Schaefer, *J. Magn. Reson.,* **96** (1), 205-209 (1992).

[3] C.P. Jaroniec, "Dipolar recoupling: heteronuclear," in Encyclopedia of Magnetic Resonance, edited by R.K. Harris and R.E. Wasylishen (Wiley, Chichester, 2009).

[4] J.P. Amoureux, J. Trébosc, J. Wiench, M. Pruski, *J. Magn. Reson.*, **184** (1), 1-14 (2007).

[5] B. Hu, J. Trébosc, J.P. Amoureux, *J. Magn. Reson.*, **192** (1), 112-122 (2008).

[6] O. Lafon, Q. Wang, B. Hu, F. Vasconcelos, J. Trebosc, S. Cristol, F. Deng and J.-P. Amoureux, *J. Phys. Chem.A,* **113** (46), 12864-12878 (2009).

[7] T. Gullion, J. Schaefer, *J. Magn. Reson.*, **81** (1), 196-200 (1989).

[8] T.G. Oas, R.G. Griffin, M.H. Levitt, *J. Chem. Phys.*, **89** (2), 692-695 (1988).

[9] R.Q. Fu, S.A. Smith, G. Bodenhausen, *Chem. Phys. Lett.*, **272** (5-6), 361-369 (1997).

[10] X. Zhao, M. Eden, M.H. Levitt, *Chem. Phys. Lett.*, **342** (3-4), 353-361 (2001).

[11] A.Lesage, D.Sakellariou, S.Steuernagel, L.Emsley, *J. Am. Chem. Soc.*, **120** (50), 13194-13201 (1998).

[12] H.M. Kao, G.P. Grey, *J. Magn. Reson.*, **133** (2), 313-323 (1998).

[13] C. Martineau, F. Fayon, C. Legein, J.Y. Buzare, G. Silly, D. Massiot, *Chem. Comm.*, (**26**), 2720-2722 (2007).

[14] J.P. Amoureux, J. Trébosc, L. Delevoye, O. Lafon, B. Hu, Q. Wang, *Solid State N.M.R*, **35** (1), 12-18 (2009).

[15] C.A. Fyfe, K.C. Wongmoon, Y. Huang, H. Grondey, *J. Am. Chem. Soc.*, **117** (41), 10397-10398 (1995).

[16] D. Massiot, F. Fayon, B. Alonso, J. Trébosc, J.P. Amoureux, *J. Magn. Reson.*, **164** (1), 160-164 (2003).

[17] M. E. Smith and E. R. H. van Eck, *Prog. Nucl. Magn. Reson. Spectrosc.*, **34** (2), 159-201 (1999).

[18] S. E. Ashbrook and S. Wimperis, *J. Chem. Phys.*, **131** (19), 15 (2009).

[19] I. Hung, A.C. Uldry, J. Becker-Baldus, A.L. Webber, A. Wong, M.E. Smith, S.A. Joyce, J.R. Yates, C.J. Pickard, R. Dupree, S.P. Brown, *J. Am. Chem. Soc.*, **131** (5), 1820-1834 (2009).

[20] E. Mazoyer, J. Trébosc, A. Baudouin, O. Boyron, J. Pelletier, J.M. Basset, M.J. Vitorino, C.P. Nicholas, R.M. Gauvin, M. Taoufik, L. Delevoye, *Angew. Chem. Int. Edit.*, **49** (51), 9854-9858 (2010).

[21] N. Merle, J. Trébosc, A. Baudouin, I. Del Rosal, L. Maron, K. Szeto, M. Genelot, A. Mortreux, M. Taoufik, L. Delevoye, R.M. Gauvin, *J. Am. Chem. Soc.*, **134** (22), 9263-9275 (2012).

[22] F.H. Larsen, H.J. Jakobsen, P.D. Ellis, N.C. Nielsen, *J. Phys. Chem.*, A **101** (46), 8597-8606 (1997).

[23] J. Trebosc, O. Lafon, B. W. Hu and J. P. Amoureux, *Chem. Phys. Lett,* **496** (1-3), 201-207 (2010).

[24] S. Capuani, F. De Luca, B. Maraviglia, *J. Chem. Phys.*, **109** (16), 6564-6570 (1998).

[25] A. Tokatli, A. Gencten, M. Sahin, O. Tezel, S. Bahceli, *J. Mag. Reson.*, **169** (1), 68-72 (2004).

[26] A.P.M. Kentgens, R. Verhagen, *Chem. Phys. Lett.*, **300** (3-4), 435-443 (1999).

[27] R. Siegel, T.T. Nakashima, R.E. Wasylishen, *J. Magn. Reson.*, **184** (1), 85-100 (2007).

[28] K.K. Dey, S. Prasad, J.T. Ash, M. Deschamps, P.J. Grandinetti, *J. Magn. Reson.*, **185** (2), 326-330 (2007).

[29] M. Bak, J.T. Rasmussen, N.C. Nielsen, *J. Magn. Reson.*, **147** (2), 296-330 (2000).

[30] M. Bak, N.C. Nielsen, *J. Magn. Reson.*, **125** (1), 132-139 (1997).

[31] P.K. Madhu, A. Goldbourt, L. Frydman, S. Vega, *J. Chem. Phys.*, **112** (5), 2377-2391 (2000).

[32] Z. Yao, H.T. Kwak, D. Sakellariou, L. Emsley, P.J. Grandinetti, *Chem. Phys. Lett.*, **327** (1-2), 85-90 (2000).

[33] N. Sinha, C.V. Grant, C.H. Wu, A.A. De Angelis, S.C. Howell, S.J. Opella, *J. Magn. Reson.*, **177** (2), 197-202 (2005).

[34] L. Delevoye, J. Trébosc, Z. Gan, L. Montagne, J.P. Amoureux, *J. Magn. Reson.*, **186** (1), 94-99 (2007).

[35] J. Yu, K. Sugiyama, K. Hiraga, N. Togashi, O. Terasaki, Y. Tanaka, S. Nakata, S. Qiu, R. Xu, *Chem. Mat.*, **10** (11), 3636-3642 (1998).

[36] D. Zhou, J. Xu, J.H. Yu, L. Chen, F. Deng, R.R. Xu, *J. Phys. Chem. B*, **110** (5), 2131-2137 (2006).

[37] L. Vidal, V. Gramlich, J. Patarin, Z. Gabelica, *Eur. J. Solid State Inorg. Chem.*, **35**, 545-563 (1998).

[38] Marichal, L. Vidal, L. Delmotte, J. Patarin, *Microporous Mesoporous Mat.*, **34**, 149-156, (2000).

[39] L. Delevoye, J. Trébosc, Z. Gan, L. Montagne, J.P. Amoureux, *J. Magn. Reson.*, **186**, 94-99 (2007).

[40] M. Eden, L. Frydman, *J. Chem. Phys.*, **114** (9), 4116-4123 (2001).

[41] M. Eden, L. Frydman, *J. Phys. Chem. B*, **107** (51), 14598-14611 (2003).

[42] G. Mali, G. Fink, F. Taulelle, *J. Chem. Phys.*, **120** (6), 2835-2845 (2004).

[43] G. Mali, V. Kaucic, F. Taulelle, *J. Chem. Phys.*, **128** (20), 204503 (2008).

[44] Q. Wang, B. Hu, O. Lafon, J. Trébosc, F. Deng, J.P. Amoureux, *J. Magn. Reson.*, **200** (2), 251-260 (2009).

[45] Z.W. Yu, A.M. Zheng, Q.A. Wang, L. Chen, J. Xu, J.P. Amoureux, F. Deng, *Angew. Chem. Int. Edit.*, **49** (46), 8657-8661 (2010).

[46] M. Eden, *J. Magn. Reson.*, **204** (1), 99-110 (2010).

[47] M.A. Eastman, *J. Magn. Reson.*, **139** (1), 98-108 (1999).

[48] D. Iuga, C. Morais, Z.H. Gan, D.R. Neuville, L. Cormier, D. Massiot, *J. Am. Chem. Soc.*, **127** (33), 11540-11541 (2005).

[49] S.K. Lee, M. Deschamps, J. Hiet, D. Massiot, S.Y. Park, *J. Phys. Chem. B*, **113** (15), 5162-5167 (2009).

[50] H.T. Kwak, P. Srinivasan, J. Quine, D. Massiot, Z.H. Gan, *Chem. Phys. Lett.*, **376** (1-2), 75-82 (2003).

[51] J. Fonseca, S. Royer, N. Bion, L. Pirault-Roy, M. D. Rangel, D. Duprez and F. Epron, *Appl. Catal. B-Environ,.* **128**, 10-20 (2012).

Chapter 3: New data processing methods for homonuclear experiments

3.1 covariance spectroscopy with a non-uniform continuous acquisition scheme for signal enhancement

Fourier transformation two-dimensional (FT2D) NMR spectroscopy has been widely used to investigate the structural of proteins and various functional materials. FT2D NMR methods usually acquired all the indirect dimension (t_1) points consecutively and equidistantly with an identical number of scans per t_1 points, and thus it is referred as UCA-FT2D (Fourier Transformation 2D with Uniform and Consecutive Acquisition scheme). To enhance the signal-to-noise ratio (S/N), the tailored acquisition scheme was proposed[1-3], which uses a decreasing number of scans as a function of t_1, while keeping the maximum t_1 evolution time and the total acquisition time the same as the regular UCA-FT2D sampling scheme. The new scheme acquired all t_1 points consecutively and equidistantly but with varying numbers of scans per t_1 points, and thus is referred as NUCA-FT2D (Fourier Transformation 2D with Non-Uniform and Consecutive Acquisition scheme). This NUCA scheme is different from the method of non-uniform sampling (NUS)[3-5], which acquires the signals with non-consecutive time increments: selecting an exponentially weighted distribution of the t_1 points while each t_1 point is acquired with an identical number of scans.

Recently, it is demonstrated that NUCA-FT2D produces overall 40－50% increase in the cross-peak intensities[1]. However, it also introduces 20－40% broadening of the cross-peak linewidths with the so-called linear 50% (equivalent to L0.5 in this chapter, we will discusse later) and Gaussian 50 (equivalent to G50) acquisition scheme. The other scheme, such as Gaussian 30 (equivalent to G30), can obtain 150% increase of the cross-peak intensities but 160% broadening of the

cross-peak linewidths. Hence, it is not applicable in the real system.

It is well known that the covariance method[6-8] can be applied to the homonuclear correlation (HOMCOR) spectra acquired by UCA-FT2D method to generate the UCA-COV2D spectra. The spectral resolution of UCA-COV2D spectra along the indirect dimension is determined by that along the detection dimension (t_2), hence to largely reduce the time-consuming sampling requirement for the indirect dimension. This means that for HOMCOR spectra, the positions and line-shapes of all resonances along the indirect dimension (F_1) are deducible from those in the direct dimension (F_2). The acquisition of the 2D time-domain spectra for covariance treatment is fundamentally the same as that for the FT2D classical method. However, after performing the first FT along t_2, the 2D frequency spectrum is then obtained by multiplying the columns corresponding to all various F_2 values, instead of performing a FT with respect to t_1. This leads to considerable reduction of experimental time and optimal resolution along the indirect dimension, at least when a sufficient number of t_1 steps are acquired. Here we will show that the covariance method can also be effectively applied to the data acquired by NUCA-FT2D scheme, inducing up to 100% increase in the cross-peak intensities and 50% enhancement of signal to noise ratio (S/N) in both dimensions in the NUCA-COV2D spectra compared to those in UCA-COV2D spectra, without deteriorating the cross-peak resolutions. Meanwhile, NUCA-COV2D can save considerable experimental time while increasing the spectral resolution compared with corresponding NUCA-FT2D. It should be mentioned that in all covariance spectra, there is a strong diagonal line with constant amplitude and line shape, which is due to auto-correlated noise. This ridge can be easily removed with data treatment by subtracting its value defined at locations where there is no resonance a priori. It's also possible to eliminate this diagonal by regularization method, where the diagonal signals are reintroduced in the mixed time-frequency domain 2D signals and then subtracted later.

3.1.1 Background

3.1.1.1 Conventional UCA-FT2D spectroscopy

With the conventional UCA-FT2D method, (i) the t_1-increment is constant and equal to the inverse of the desired spectral-width in the indirect dimension:

$$\Delta t_1 = 1/SW_1 \tag{1}$$

and (ii) the optimum maximum evolution time, $t_{1max,FT}$, is ca. inversely proportional to the minimum line-width, χ_{min}, observed in the 1D spectrum[9]:

$$t_{1max,FT} \approx 2/(3\chi_{min}) \tag{2}$$

In case of large required spectral-width and narrow resonances, this leads to numerous t_1 steps, N, and hence to very long experimental time, mainly to obtain a sufficient resolution along F_1:

$$N = t_{1max}/\Delta t_1 \approx 2/(3\chi_{min}\cdot\Delta t_1) = 2\cdot SW_1/(3\chi_{min}) \tag{3}$$

With conventional UCA-FT2D experiments, the number M of scans accumulated for each of the N (Eq.3) t_1 values and the Δt_1-increment (Eq.1) are constant.

3.1.1.2 Profiles for Non-Uniform Continuous Acquisition schemes

To ensure that the total experimental time of NUCA scheme is the same as that of UCA scheme, linear profile (L_k) and normalized Gaussian profile (G_k) for NUCA scheme are respectively defined as:

Linear:

$$l_k = M(1 + q\frac{N-2k}{N})$$
$$L_k = \varepsilon_l l_k = \frac{M}{(\sum_{k=1}^{N} l_k)/N} l_k \tag{4}$$

Gaussian:

$$g_k = M\frac{2N}{\sqrt{2\pi}\sigma}\exp(-\frac{k^2}{2\sigma^2})$$
$$G_k = \varepsilon_g g_k = \frac{M}{(\sum_{k=1}^{N} g_k)/N} g_k \tag{5}$$

where k is the t_1 scan index, L_k and G_k are the number of scans for each k, M is the number of scans in UCA-FT2D experiments, N is the maximum t_1 points, q is the slope of the linear profile, σ is the standard deviation controlling the width of the Gaussian "bell", and ε_l and ε_g are the scaling factors because the profiles do not reach zero in some cases when k = N. The illustrative demonstration of profiles is shown in Fig. 1. In practice, the number of scans L_k and G_k are rounded to the nearest integer, which is the multiple of the minimum phase cycling number. In this chapter the minimum phase cycling number of 4 is used. In the following, the linear profile with the slope q will be represented as L_q and the Gaussian profile with standard deviation σ as $G\sigma$. For convenience, UCA scheme will be referred as the "square" profile. For the FT in the t_1 dimension, Gaussian window multiplication with the Gaussian broadening factor of 0.1 and exponential broadening factor of a Hz will be applied in UCA scheme, here referred as Sa profile. No scaling was applied to the data prior to the covariance processing.
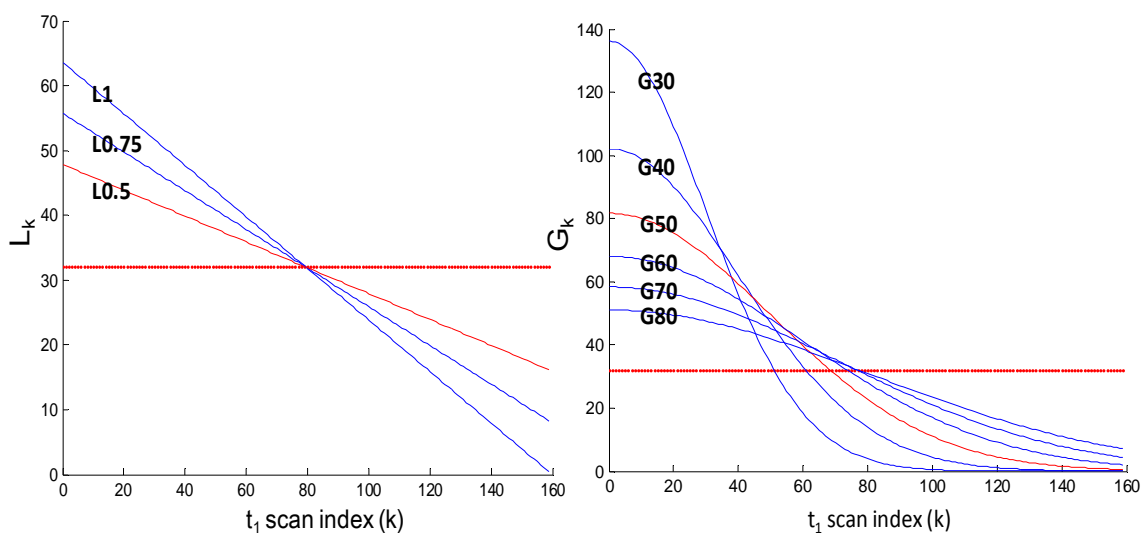

Fig.1 The linear (a) and Gaussian (b) profiles for the NUCA scheme according to the definition in Eq. (1) and Eq. (2), respectively. M=32, N=160.

3.1.2 Experimental section

Experiments were performed on model samples of L-[U-13C]- histidine HCl·H$_2$O with 99% ^{13}C purity, which were purchased from CortecNet and used

without further purification. The protein [U-13C]-GB1 microcrystal and lipid-reconstituted green [U-^{13}C, ^{15}N]- proteorhodopsin (PR, a bacterial light-driven proton pump)[10,11], were used to demonstrate general applicability of NUCA-COV2D.

Experimental verifications based on L-histidine were performed on Bruker AVANCE-III 600 MHz with B_0 = 14 T. Commercial Bruker double-resonance $\varnothing$ = 2.5 mm MAS probes were used. Typical 90° pulse lengths were 3.5 µs on both channels. The contact time for cross-polarization was 3 ms, and TPPM proton decoupling[12] of 85 kHz was used during evolution and detection periods. Recycle delays were 1.2 s for all experiments. The condition of ν_{1H} = 12.5 kHz with t_m = 224 ms was used for SHANGHAI irradiation[13] in ^{1}H channel spinning at ν_R = 25 kHz. The t_1 increment was set to 40 µs with 160 real and imaginary FIDs in the t_1 dimension. Additional experimental details are given in the figure captions.

The spectra of [U-^{13}C]-GB1 and [U-^{13}C, ^{15}N]-PR shown in this chapter have been acquired on Varian wide-bore 600 MHz with B_0 = 14 T, equipped with a $\varnothing$ = 4 mm triple-resonance T3-HXY MAS probe. Typical 90° pulse lengths were 3.45 µs on ^{1}H channel and 4.2 µs on ^{13}C channel respectively. The contact time for cross-polarization was 0.9 ms, and SPINAL-64 proton decoupling[14] was applied during evolution and detection periods with ν_{dec} = 70 kHz. The setting of ν_{1H} = 13.33 kHz was used for DARR irradiation[15,16] in 1H channel spinning at ν_R = 13.33 kHz. The t_1 increment was set to 25 µs. Recycle delays were 2 s. The sample temperature was around 6 ^{o}C controlled by a fluid cooling gas (-5 ^{o}C). Additional experimental details are given in the figure captions.

3.1.3 Results and discussion

Fig. 2 represent the comparison of square, linear, Gaussian profile in FT2D and COV2D with the model sample L-histidine and SHANGHAI recoupling sequences[13]. The SHANGHAI recoupling sequences was reported to be a broad-band excitation

sequences for ^{13}C-^{13}C correlations and can be a good alternative to DARR[15,16] and

PARIS$_{xy}$[17-20] sequences. Here SHANGHAI irradiation with 224 ms is used, to ensure

that all the cross-peaks showed up. The values in Fig. 2 were obtained by averaging the

corresponding information of all the cross-peaks statistically. The S/N values were

calculated by selecting the column along ω_1 at maximum peak intensity of each peak

with the noises averaged from 250 ppm to 180 ppm along this column.Basically,

Gaussian-FT2D profile introduces larger increments in both signals and linewidths than

the linear-FT2D. Here we also examine the S/N, which is not discussed in Wei's paper.

To evaluate the enhancements, it is more reasonable to measure S/N, rather than the

signal intensity.   Apparently, the increase in S/N of NUCA-FT2D is lower than that in

signals, because the NUCA profile will introduce noise at the tail of t_1 domains.
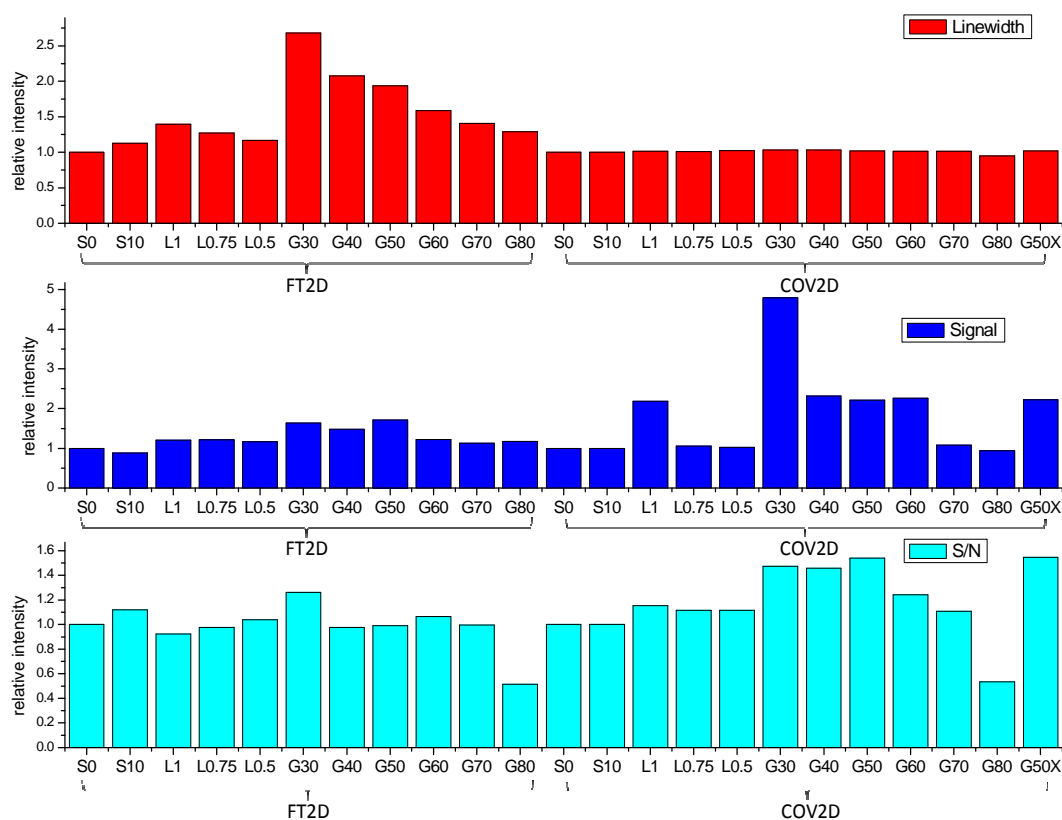
Fig.2 Plots of the increment in linewidth (top), signal (middle) and S/N (bottom) in indirect
dimension with different acquisition profiles in FT2D and COV2D with the sample
L-[U-^{13}C]-histidine HCl·H$_2$O. For FT2D and COV2D data, all elements are normalized with
respect to S0 profile. The values here were obtained by averaging the corresponding
information of all the cross-peaks statistically in the 2D SHANGHAI spectra. 160 real and
image t_1 points were used for all the cases, except that only 80 real and image t_1 points were
used for G50X-COV2D.

On the other hand, most COV2D schemes generate a relatively large enhancement in S/N without any broadening in the line-widths or the generation of any ripples. Generally, the G50-profile achieves the best S/N. It should be noted that although G30-COV2D achieves an increment in signal as large as 4.8 times compared with S0-COV2D, it only introduces an enhancement of 43% in S/N. This difference is possibly due to the fact that G30 profile introduced the large signal because of the large number of scans in the beginning of the t_1 domains, in which the signal is always the strongest even in the UCA-FT2D, but it also introduces more noises along this column[21]. Generally, the G50-profile achieves the best S/N, which suggests that to obtain the best S/N, the Gaussian profile should smoothly approach zero at k=N.
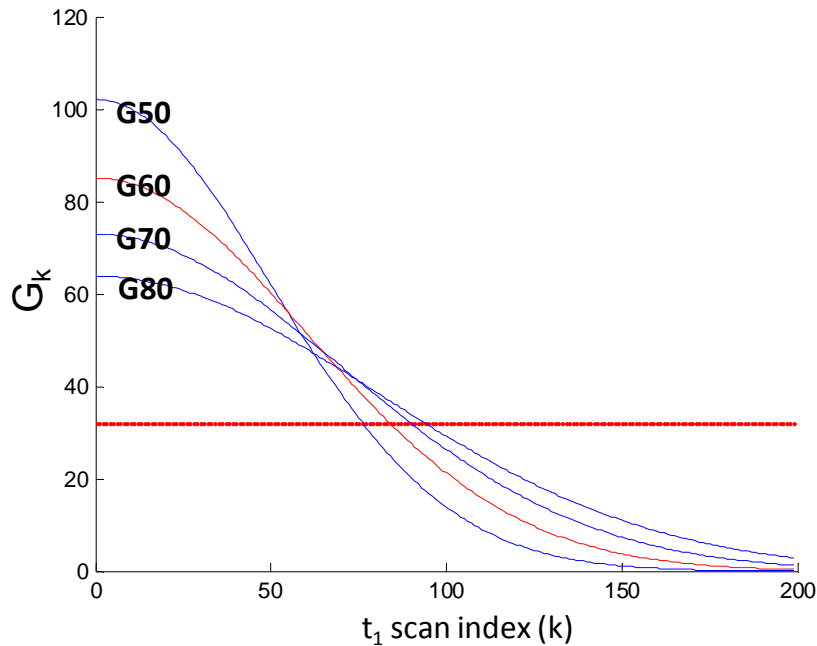
Fig.3 The Gaussian profiles for the NUCA scheme. M=32, N=200. The optimum G60 scheme is shown in red color.

It was previously reported that COV2D could save much experimental time compared to FT2D[8]. However, indiscriminate decrease in the t_1 acquisition points will greatly lower the spectral resolution and S/N[8,22]. Thus it is of great importance to determine the safety regions of t_1 points for each experiment. It was found out that the optimum number of t_1 points depends on the minimum linewidth in the FT1D spectrum

and the dwell time (dw_1) of t_1 domain[9,22]. This dependence also suggests the dependence of optimum number of t_1 points on the signal decay rate $1/T_2^*$, in which T_2^* is governed by the relaxation processes and inhomogeneity of the static field. Suppose the minimum linewidth in the FT1D spectrum is χ Hz, and then the optimum t_1 time for FT2D is $t_{1FT} = 2/3\chi$[9], and the optimum t_1 time for COV2D treatment, according to our previous experience, to select the optimum t_1 time of $1/3\chi$ is a better choice[22]. In the case of L-histidine with $\chi = 104$ Hz and the t_1 dwell time $dw_1 = 40$ μs, the optimum t_1 points for FT2D and COV2D can be calculated as 160 and 80, respectively. Thus, the 160 t_1 points used for G50-COV2D can be further truncated to 80, resulting in G50X-COV2D. Apparently, G50X-COV2D did not deteriorate the resolution and S/N.
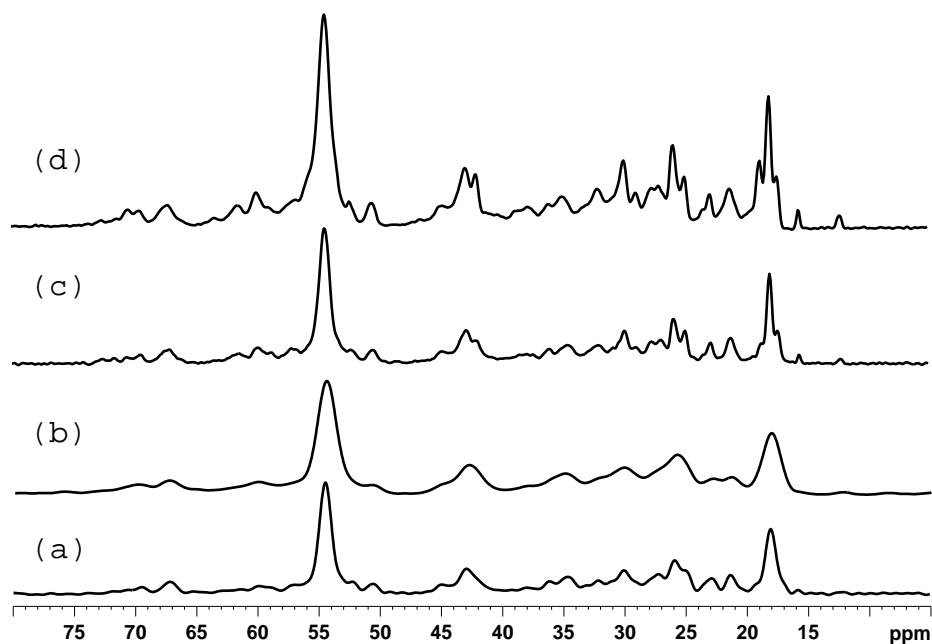
Fig.4 Plots of the selected 1D slice from 54.4 ppm along indirect dimension in ^{13}C 2D DARR spectra of [U-^{13}C]-GB1 with different approaches: (a) S10-FT2D, (b) G60-FT2D, (c) S10-COV2D; (d) G60-COV2D. The average scan number of each t_1 point was 32, the DARR mixing time t_m=100 ms and 200 real and image FIDs in the t_1 dimension were used.

To further demonstrate the improvement of NUCA-COV2D, the [U-^{13}C]-GB1 sample was tested with two schemes: the traditional square scheme and the G60 scheme which is anticipated to be able to achieve the best S/N for the 200 t_1 points (dwell time dw_1=25 μs) (Fig. 3). Clearly, as shown in Fig. 4, G60-FT2D generated large

broadening of the peaks, which is not desirable for analyzing the real samples. The S/N enhancement of G60-COV2D compared to S10-COV2D was around 51% in both dimensions, which is consistent with above results. Furthermore, with the limited t_1 points of 200, while 400 points is demanded by FT2D experiments, the COV2D spectra can enhance the spectral resolution compared to traditional FT2D in F_1 dimension, which is also reported before[9,23].
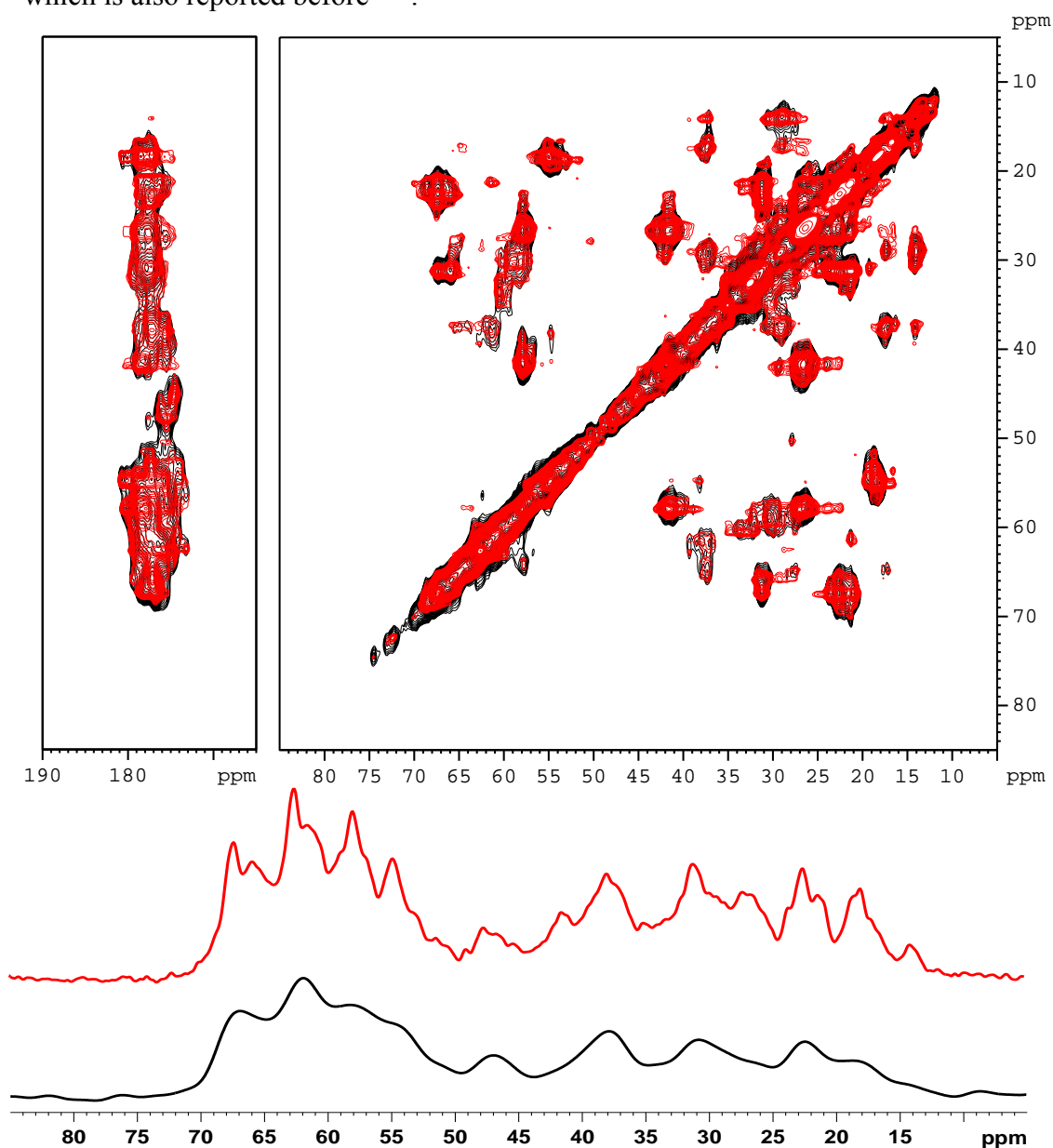
Fig.5 2D Comparison (top) and 1D slice comparison (bottom) of ^{13}C DARR spectra of [U-^{13}C,^{15}N]-PR with G40-FT2D (black) and G40-COV2D (red). The slices are selected from 176.5 ppm along indirect dimension. The average scan number of each t_1 point was 128, the DARR mixing time t_m=30 ms was used for short-distance correlations and 96 real and image FIDs were used in the t_1 dimension.

Lastly, we show the comparison of G40-FT2D (black) and G40-COV2D (red) in the sample [U-^{13}C, ^{15}N]-PR, with 96 t_1 points and dwell time dw_1=25 μs (Fig. 5). 2D spectra (Fig. 5a) and 1D slices (Fig. 5b) along 176.5 ppm along F_1 dimension demonstrated the clear advantages of NUCA-COV2D in resolution. However, it should also be mentioned that, COV2D will produce a few weak 'relayed' cross peaks which correspond to long-range correlations, which cannot be observed in FT2D spectra with short mixing time[8]. These 'relayed' cross-peaks, which correspond to long-range correlations, can be observed in FT2D DARR spectra with long mixing time[13,15,16].

3.1.4 Conclusion

In conclusion, NUCA-COV2D (covariance processing with a non-uniform continuous acquisition scheme) is beneficial for producing ^{13}C-^{13}C correlation spectra of model samples and the microcrystalline proteins with both good resolution and S/N. UCA-COV2D scheme will generate the spectra with lower S/N, and NUCA-FT2D scheme will produce those with lower resolution. With the Gaussian profile and COV2D method, we were able to reduce the number of increments in t_1 by a factor of 1.5~3. The S/N was also increased by another factor of 1.5, which further saves experimental time by a factor of 2, without sacrificing any resolution in the indirect dimension. Furthermore, for amplitude-modulated spectra, the total experimental time of COV2D is also reduced by an additional factor of 2, since COV2D data treatment does not require States or TPPI acquisition to obtain the correct resonance frequencies along F_1 dimension. Covariance NMR has been shown to work for 4D spectra for resolution enhancement. As solid state NMR is nowadays applied to biomolecules of ever-increasing size, such advances might become especially vital to analyze higher-dimensional NMR spectra.

3.2 Comparison of various sampling schemes and accumulation profiles in covariance spectroscopy with exponentially decaying 2D signals

Recently, a host of methods have been proposed to reduce the experimental time of these 2D NMR experiments treated with two FTs, referred as FT2D, without broadening too much the line-widths along F_1. These methods include reduced dimensionality[24], G-matrix FT[25], back-projection reconstruction[26], filter diagonalization[27], maximum entropy (MaxEnt) reconstruction[28,29], Bayesian[30] and maximum likelihood[31] methods, multi-way decomposition[32,33], and covariance[34-36]. Most of these methods employ the general scheme of non-uniform sampling (NUS). A typical NUS scheme uses Δt_1 values increasing exponentially with t_1, that is densely and sparsely sampling for short and long evolution times, respectively, which is referred in the following as exponentially decreasing NUS[28] scheme. However, such NUS 2D temporal data-sets cannot be converted to the frequency domain with the conventional FT2D method. Therefore, different data-treatments have been proposed to reconstruct the 2D spectrum, such as MaxEnt[28,29] reconstruction, discrete FT[37,38], and multi-way decomposition[32,33]. Another simple way to decrease the experimental time is to utilize a uniform sampling with a t_1 cut-off (CUO) to only acquire the signals for short t_1 values, and then reconstruct the 2D NMR spectrum with MaxEnt methods[28,29]. However, this reconstruction is only feasible if the number of sampled t_1 points is not too limited. It has been shown that for the same reduced number of selected t_1 points, the NUS-MaxEnt scheme works better than the CUO-MaxEnt method, due to large resolution decrease along F_1 in the second case[28,29]. However, under some circumstances with sine/cosine modulated experiments or constant-time experiments with no decay, random NUS sampling with MaxEnt reconstruction provided high-resolution spectra with dramatic reduction in experimental time[39,40]. Although there are many other proposed NUS sampling schemes[41], to the best of our

knowledge, exponentially decreasing sampling scheme is still the most widely used method, since exponentially decaying 2D signals are the most widely encountered in practice. Thus, the NUS scheme used in this work will be that of an exponentially decreasing sampling, and it will be applied to exponentially decaying 2D signals.

The COV2D approach can be applied with at least two different reduced sampling schemes along t_1 to decrease the protracted experimental time. It can either be combined with NUS t_1 sampling[42], or simply use a limited number of t_1 points with CUO sampling[36,43,44]. Both sampling methods have the benefit of saving time, while keeping the quality of NMR spectra. Furthermore, both methods do not need any post-acquisition operation before data processing. However, to the best of our knowledge, no detailed comparison of COV2D with these two reduced sampling methods has been made.

In this section, we show that for the same experimental time, COV2D with CUO sampling (CUO-COV2D) is always more sensitive than NUS-COV2D. In addition, we demonstrate that with COV2D, Gaussian accumulation profile presents better performance than constant square profile. It must be reminded here that all methods compared in this article use the same FT, apodization, and phasing along the F_2 dimension. In the following, we will call: (i) US-FT2D the conventional method with two FTs and uniform sampling of the N t_1 points; (ii) CUO-MaxEnt and NUS-MaxEnt the methods with CUO or NUS restricted ($n \leq N$) sampling and MaxEnt reconstruction of 2D frequency data-set; (iii) CUO-COV2D and NUS-COV2D the covariance methods with CUO and NUS restricted ($n \leq N$) sampling. When relevant, these acronyms will be concatenated with the different accumulation profiles, e.g. SQ-CUO-COV2D is referred to the covariance treatment with CUO sampling and square (SQ) accumulation profile.

3.2.1 Background

3.2.1.1 Conventional US-FT2D spectroscopy

In the conventional US-FT2D method, (i) the t_1-increment, (ii) the optimum maximum evolution time, $t_{1max,FT}$, and (iii) the number of st_1 steps, N, have already been defined in Eq.1, Eq.2 and Eq.3.

With conventional US-FT2D experiments, the number M of scans accumulated for each of the N t_1 values and the Δt_1-increment are constant. This constant number of scans, which will be hereafter referred as a square (SQ) accumulation profile, thus leads to the SQ-US-FT2D full acronym.

To obtain better S/N and/or resolution, it is possible to optimize (i) the number of scans accumulated on each t_1 step (e.g. Gaussian accumulation profile), (ii) the number of sampled t_1 values (e.g. CUO sampling), and (iii) the Δt_1 sampling increment (e.g. NUS sampling).

3.2.1.2 Gaussian accumulation profile

Gaussian profile, G_k, is defined in Eq.5. N is the number of t_1 points that should be used with SQ-US-FT2D to obtain the desired spectral-width and keep a sufficient resolution. M is the constant number of accumulations performed on each t_1 step with SQ-US-FT2D. Thanks to the ε_g scaling factor, the same total number of scans, $Z = M \cdot N$, is accumulated with both profiles. This scaling factor is close to unity if $g_N \approx 0$, and larger than one in other cases. $k = 1, 2, \ldots, N$ is the t_1 scan index, G_k is the number of scans for each k value, and σ is the standard deviation controlling the width of the Gaussian "bell". In practice, for each t_1 step, the number of scans G_k is rounded to the closest multiple of the minimum phase cycling number (4 in this section).

In the following, the Gaussian accumulation scheme with a standard deviation of σ will be called profile Gσ. The illustration of SQ and Gσ profiles is shown for $N = 160$ and $\sigma = 50$, as red lines in Figs.6a,c and 6b,d respectively. It should be mentioned that the choice of σ depends on the N value. For example, $\sigma \approx 50$ leads to the best S/N

when $N = 160$ (Fig.8b), whereas it should be $\sigma \approx 100$ for $N = 320$.

Actually, any window function used for 2D NMR, such as linear, Gaussian, sine-bell and squared sine-bell, can be used as accumulation profile to potentially improve the *S/N*. However, in this section, only the Gaussian accumulation profile will be considered, since it has been demonstrated that it can provide better *S/N* than linear and square profiles in the last section. Nevertheless, other window-function profiles might achieve better *S/N* compared to Gaussian profile.
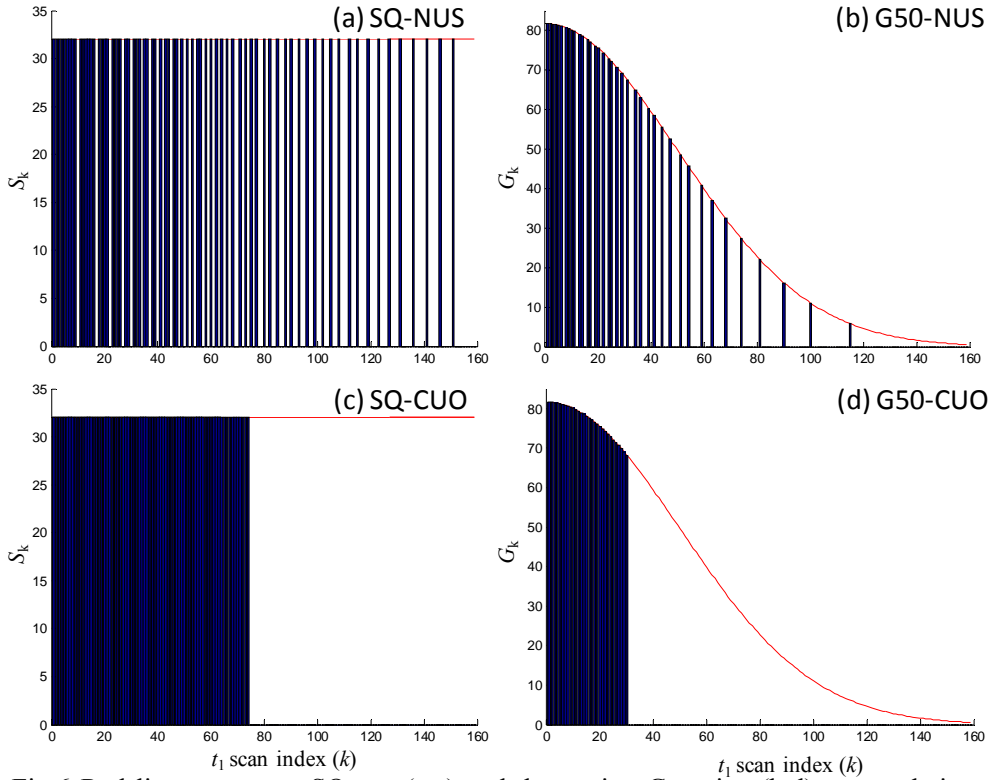
Fig.6 Red lines: constant SQuare (a,c) and decreasing Gaussian (b,d) accumulation profiles. Vertical blue bars denote either NUS (a,b) or CUO (c,d) restricted sampling of the t_1 points. $M = 32$, $N = 160$, $\sigma = 50$, $\xi = 0.47$; $n = 75$ (c) or 32 (d).

3.2.1.3 CUO and NUS restricted sampling schemes

The principle of CUO and NUS restricted sampling schemes is to only use less t_1 points. The procedure for CUO is to just acquire the first $n \leq N$ points with Δt_1-increment given by Eq.1.

The procedure for exponentially decreasing NUS scheme, used to find n exponentially sampled points out of N uniformly sampled points ($n < N$), is describe

as follows. First we define a continuous sampling density function

$$D(x) = \exp(-kx), \qquad x > 0 \qquad (6)$$

Where k is calculated to make $\int_0^N D(x)dx = n-1$. From $D(x)$ we then calculate the successive rounded integrals

$$I_j = \text{integer part } (\int_0^N D(x)dx) \quad \text{for} \quad j = 1,\ldots,N \qquad (7)$$

For each integer $l = 0, 1, \ldots, n-1$ we sample at the first data point j which satisfies $I_j = 1$. In this way we sample more points when the density, $D(x)$, is large and less often when it is small, producing an exponentially sampled data set[45].

The illustrative demonstration of NUS and CUO sampling schemes applied to SQ accumulation profile is shown with vertical bars in Fig.6a and 6c respectively, and in Fig.6b and 6d when applied to $G\sigma$ profile.

Table.1 Relationship between n and ξ for different profiles, with $N = 160$. As example, a global sampling-saving factor $\xi = 0.47$ is obtained with the $n = 32$ first t_1 points or 40 NUS t_1 points, according to which scheme (G50-CUO or G50-NUS) is used. The same sampling-saving factor is obtained for square (SQ) profile with the $n = 75$ first t_1 points. On each line, the total number of scans is constant and equal to $Z' = \xi \cdot M \cdot N = 160 \cdot \xi \cdot M$. For other N values, the n value should be scaled accordingly.

ξ	SQ n	G70-NUS n	G70-CUO n	G50-NUS n	G50-CUO n	G30-NUS n	G30-CUO n
1.00	160	160	160	160	160	160	160
0.92	147	142	115	136	87	120	51
0.84	134	121	96	112	71	89	41
0.74	118	102	77	88	57	64	33
0.62	100	78	60	64	44	41	26
0.55	88	65	51	51	38	32	23
0.47	75	52	43	40	32	24	19
0.36	57	36	32	27	23	16	14
0.23	36	20	20	16	15	9	9

If all N t_1 points are sampled with the SQ accumulation profile, the total number of scans is $Z = M \cdot N$. To save the experimental time, $n \leq N$ t_1 points are sampled with CUO or NUS schemes leading to only $Z' \leq Z$ total number of scans. This corresponds to the global sampling-saving factor of $\xi = Z'/Z \leq 1$. In addition to the N and σ values used in Eq.5, the Gaussian accumulation profile must also take into account the n value. In order to obtain the same ξ value for easy comparison of the methods, the number n of sampled t_1 values is different for $G\sigma$ and SQ accumulation profiles, as shown in Table 1.

3.2.1.4 Covariance spectroscopy

We have mentioned in Chapter 1, the evolution and detection times of a HOMCOR signal lead to a $s(t_1, t_2)$ 2D matrix. After the first FT with respect to t_2, the signal is phased and apodized with respect to ω_2, which then leads to a mixed 2D matrix $S(t_1, \omega_2)$. With the conventional US-FT2D method, a second FT is then usually performed with respect to t_1, leading to $S(\omega_1, \omega_2)$.

With the COV2D method, $S(t_1, \omega_2)$ is then used to compute the real and symmetric covariance (C) and cross-correlation (F) spectra:

$$C(\omega_1, \omega_2) = C(\omega_2, \omega2) = S(t_1, \omega_2)^T S(t_1, \omega_2) \tag{8}$$

$$F(\omega_1, \omega_2) = \sqrt{C(\omega_1, \omega_2)} \tag{9}$$

where $S(t_1, \omega_1)^T$ is the transpose matrix of $S(t_1, \omega_1)$. It must be noted that Eq.9 corresponds to the square-root of a square matrix, not of a scalar number. COV2D treatment must be combined with TPPI or States acquisition methods, to avoid false peaks due to the fact that $\int\cos(\omega_i t_1)\cdot\cos(\omega_j t_1)\mathrm{d}t_1$[34,35,46] is equal to $\int\cos(\omega_i t_1)\cdot\cos(-\omega_j t_1)\mathrm{d}t_1$. Furthermore, COV2D treatment introduces a non-informative diagonal line due to auto-correlated noise. However, this ridge can easily be removed by data treatment[47], or regularization method[42].

$F(\omega_1, \omega_2)$ is similar to the classical FT2D spectrum $S(\omega_1, \omega_2)$, whereas $C(\omega_1, \omega_2)$

is close to the power spectrum of $S(\omega_1, \omega_2)$. The correlation information in the two $C(\omega_1, \omega_2)$ and $F(\omega_1, \omega_2)$ covariance spectra is identical. It should be pointed out that $F(\omega_1, \omega_2)$ was proved to cover all the correlation information in FT2D spectrum $S(\omega_1, \omega_2)$, however, covariance spectra $F(\omega_1, \omega_2)$ have been shown to contain some "relayed" peaks which do not exist in $S(\omega_1, \omega_2)$, as shown in Fig.7. This behavior may impose some limitations to the application of COV2D. In practice, covariance has been used
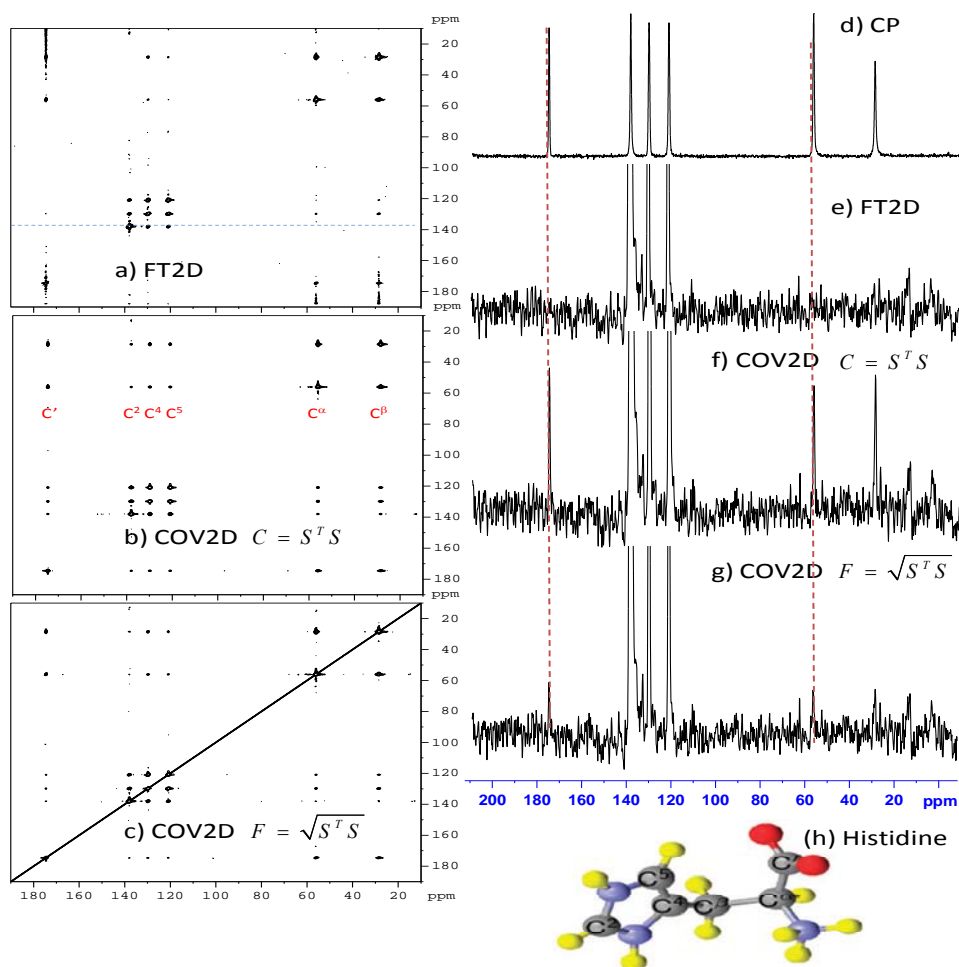

Figure.7 Comparison of the relayed-peaks observed in the 2D spectra treated with FT2D (a), or COV2D:$C(\omega_1,\omega_2)$ (b) and $F(\omega_1,\omega_2)$ (c). The same low contour level has been used for all spectra. Both the cosine and sine parts required by the States acquisition were used in (a,b,c). The data have been obtained on histidine sample (h) with the PARIS$_{xy,m=2}$ sequence using: $\nu_R = 40$ kHz, $\nu_1 = 10$ kHz, $B_0 = 21.1$ T and $\tau_{mix} = 250$ ms. Due to the use of low ^{1}H irradiation power, $\nu_1 = 0.25\nu_R$, several cross-peaks are not revealed in (a). (e,f,g): Comparison of the selected 1D slices along $C^2 = 138$ ppm. The CPMAS spectrum is shown in (d) for comparison. Clearly, two "relayed-peaks" at ($C^2 = 138$ ppm, $C' = 180$ ppm) and ($C^2 = 138$ ppm, $C^\alpha = 56$ ppm) show up in the two COV2D spectra, while they do not appear in FT2D spectrum. The lost of these peaks in FT2D spectrum arises from the narrow-band nature of PARIS$_{xy,m=2}$.

for some SQ–SQ (single quantum–single quantum) NMR experiments, such as NOESY, ROESY and TOCSY in the liquid-state[23], and SHANGHAI[13] in the solid-state. However, in those experiments, "relayed" peaks actually correspond to long-range correlations, and thus can also be observed in FT2D spectra with a long mixing time. In this section, only the cross-correlation spectra $F(\omega_1, \omega_2)$ will be analyzed.

3.2.1.5 Noise with covariance treatment

Covariance processing is a non-linear method for spectral analysis, and thus the 2D noise 'floor' generated by covariance is non-uniform. There are three different types of noise observable in COV2D spectra[49] (Fig.8b). The first one, referred as $N_{peak-free}$, is the noise observed away from the diagonal and from the ridges along the columns and rows with peaks[49]. This white noise is Gaussian-distributed and identical everywhere (Fig.8e). The second noise, referred as $N_{peak-ridge}$, is that observed on the ridges along the columns and rows with peaks. The amplitude of $N_{peak-ridge}$ increases with the peak amplitude and is approximately constant along the ridges (Fig.8d). It arises from the multiplication of the column along the white noise with the column along the peaks in covariance data treatment[49]. The third diagonal noise, referred as N_{diag}, is related to the covariance auto-correlation of the white noise, and it is thus mainly a positive signal (Fig.8c). Its position is identified, and thus this constant noise can be taken off by data treatment. Generally, we have $N_{peak-free} < N_{peak-ridge} < N_{diag}$ (Fig.8c-e).
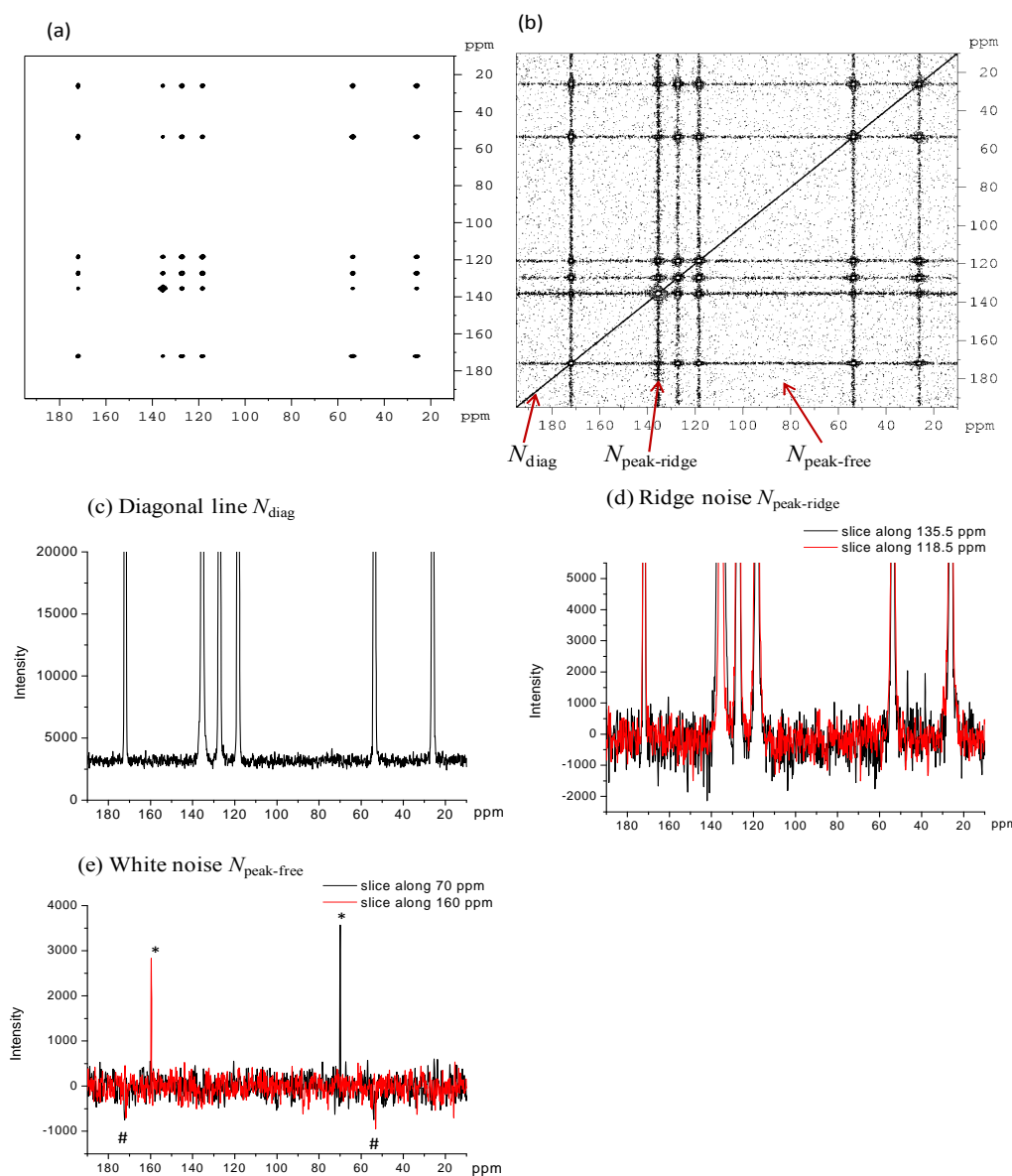
Fig.8 ^{13}C-^{13}C SHANGHAI 2D spectra of L-[U-^{13}C]-histidine·HCl·H$_2$O treated with COV2D, either with a high (a) or low (b) level of representation. The three types of noises: $N_{\text{peak-free}}$, $N_{\text{peak-ridge}}$, and N_{diag} are indicated in (b). They are also shown in the 1D slices; (c) N_{diag}: constant value of ca. +3000, (d) $N_{\text{peak-ridge}}$ along the horizontal ridges at 118.5 and 135.5 ppm showing two different noise levels in between ca. ±1000, (e) $N_{\text{peak-free}}$ along the horizontal ridges at 70 and 160 ppm showing the same level of ca. ±300. The asterisks point out the N_{diag} signals, which are ca. 10 times larger than $N_{\text{peak-free}}$. The pound signs # mark the $N_{\text{peak-ridge}}$ signals.

3.2.2 Results and discussion

3.2.2.1 Comparison of various $S/N_{\text{peak-ridge}}$ and $S/N_{\text{peak-free}}$

Owing to the fact that $N_{\text{peak-free}} < N_{\text{peak-ridge}}$ and that the diagonal noise can be taken off,[31] in a conservative analysis one may assume that the ability to distinguish

the signal from the noise mainly depends on $N_{\text{peak-ridge}}$. Therefore, in a first analysis, we have used this ridge noise to define the signal to noise ratio ($S/N_{\text{peak-ridge}}$) in Fig.9 and Fig.11. Here, it should be pointed out that, even though using this ridge noise may not define perfectly the sensitivity, this is a simple method to analyze the apparent sensitivity.

All the experimental details in this section are the same as those in the last section. Fig.9 illustrates the comparison of CUO and NUS sampling schemes applied with covariance treatment, versus the ξ sampling-saving factor, with SQ, G70, G50 and G30 accumulation profiles. We have used the model sample L-[U-^{13}C]-histidine HCl·H_2O and the SHANGHAI ^{13}C-^{13}C recoupling sequence with mixing time of 224 ms, to ensure that all cross-peaks show up[13] (Fig.8a).
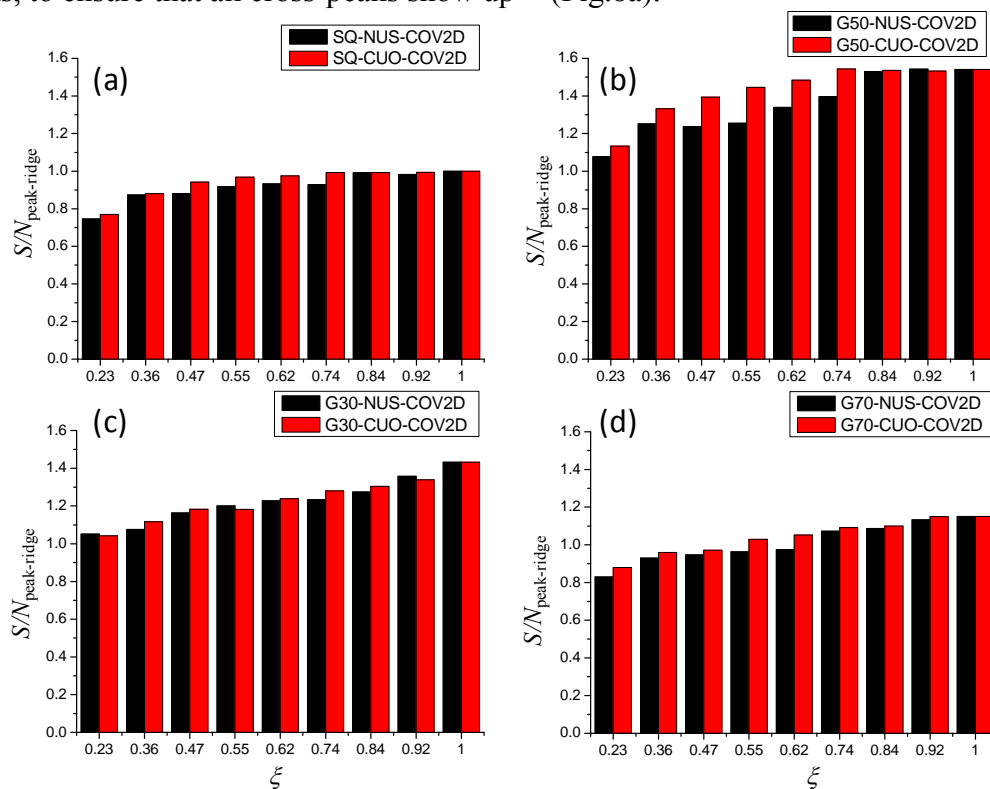

Fig.9 Experimental L-[U-^{13}C]-histidine HCl·H_2O covariance $S/N_{\text{peak-ridge}}$ ratio of ^{13}C-^{13}C 2D spectra, versus the ξ sampling-saving factor, for four different accumulation profiles: SQuare (a), G70 (d), G50 (b), and G30 (c), with $M = 32$ and $N = 160$. For each accumulation profile, $S/N_{\text{peak-ridge}}$ ratios observed for CUO and NUS sampling schemes are compared. They are obtained by averaging statistically the $S/N_{\text{peak-ridge}}$ ratios of all cross-peaks. For each of them, the $S/N_{\text{peak-ridge}}$ value is the ratio between the maximum intensity of the peak and the noise averaged along F_1 in between 180-250 ppm for the column corresponding to this peak. All values are normalized with respect to that observed with full sampling with constant SQ profile ($\xi = 1$ in (a)).

As a general rule, reduced CUO sampling scheme always provides identical or better $S/N_{\text{peak-ridge}}$ ratios than NUS, except slightly for $\xi = 0.23$ and 0.55 with the G30 profile, due to statistical errors. This observation demonstrates that the data points for short t_1 values are the most informative for covariance processing[31]. Globally, for identical experimental time and hence for equal ξ value, G50-CUO-COV2D method always yields the best $S/N_{\text{peak-ridge}}$ ratio among the eight accumulation and sampling profiles (Fig.9b).
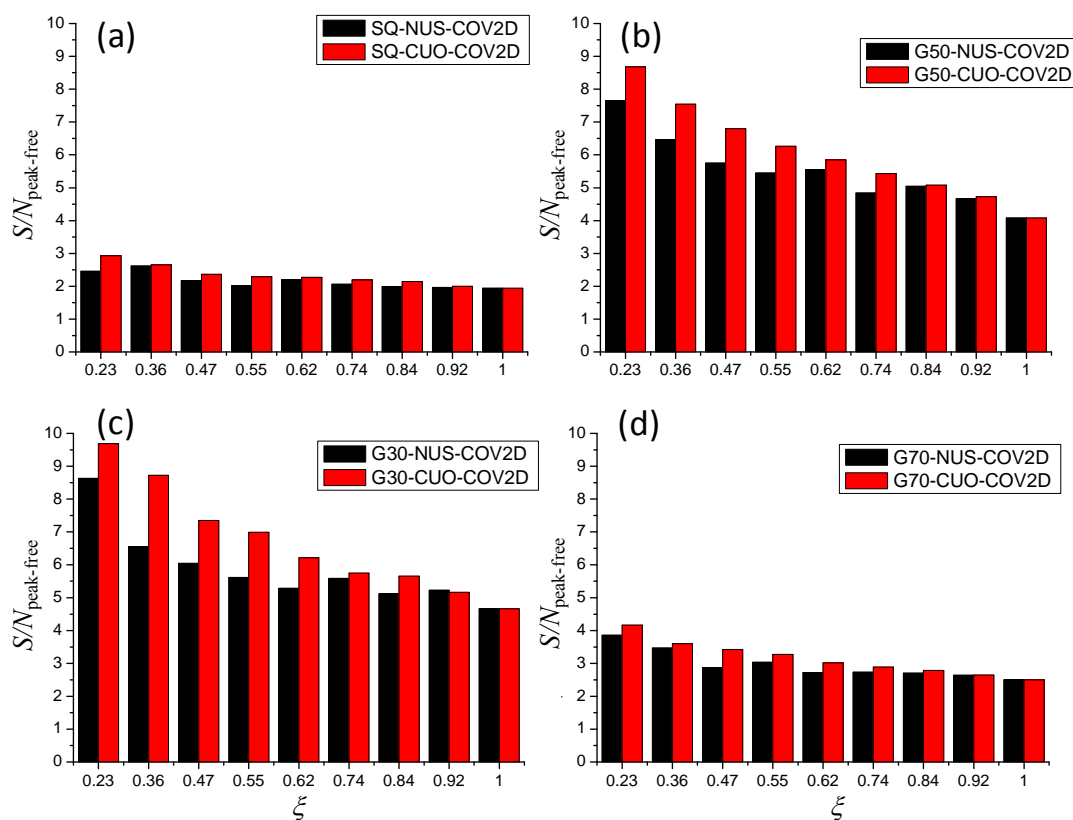

Fig.10 Experimental L-[U-^{13}C]-histidine·HCl·H$_2$O covariance $S/N_{\text{peak-free}}$ ratio of ^{13}C-^{13}C 2D spectra, versus the ξ sampling-saving factor, for four different accumulation profiles: SQuare (a), G70 (d), G50 (b), and G30 (c), with $M = 32$ and $N = 160$. For each accumulation profile, $S/N_{\text{peak-free}}$ ratios observed for CUO and NUS sampling schemes are compared. They are obtained by averaging statistically the $S/N_{\text{peak-free}}$ ratios of all cross-peaks. For each of them, the $S/N_{\text{peak-free}}$ value is the ratio between the maximum intensity of the peak and the noise in the peak-free region. All values are normalized with respect to that observed with full sampling and constant SQ profile ($\xi = 1$ in Fig.9a).

When the discrimination between the signal and the noise is not performed along

the ridges, but from another direction, the noise level is equal to $N_{peak-free}$. This leads to $S/N_{peak-free}$ ratios that can be easily compared to those observed with US-FT2D experiments. In Fig.10 we have represented the covariance $S/N_{peak-free}$ ratios versus the ξ sampling-saving factor. It is interesting to observe that the CUO reduced sampling again always provides identical or better $S/N_{peak-free}$ ratios than NUS sampling. However, these ratios decrease with increasing ξ value, contrary to that observed with $S/N_{peak-ridge}$ (Fig.9). It should also be noted that G30 and G50 accumulation profiles lead to best $S/N_{peak-free}$ ratios. Another important point is that $S/N_{peak-free}$ is much larger than $S/N_{peak-ridge}$.

3.2.2.2 Constant time $S/N_{peak-ridge}$ and $S/N_{peak-free}$
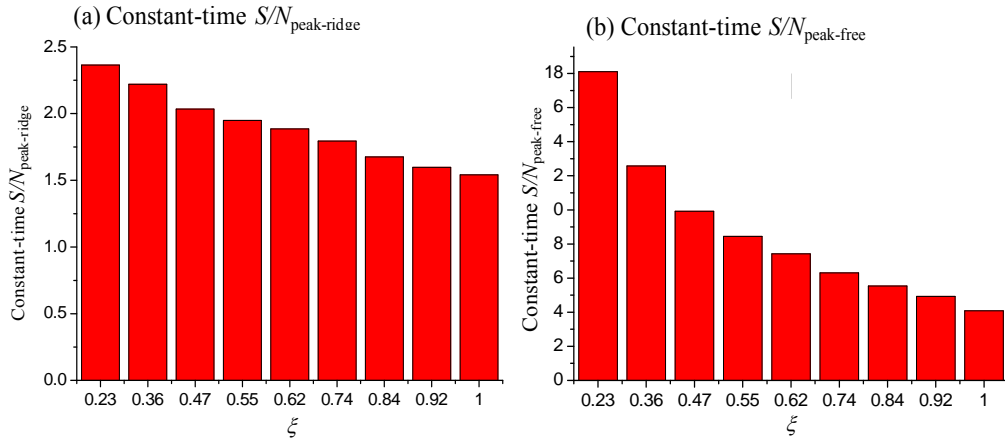
Fig.11 Constant-time $S/N_{peak-ridge}$ (a) and $S/N_{peak-free}$ (b) values of G50-CUO-COV2D, versus ξ sampling-saving factor. These values are equal to the previous $S/N_{peak-ridge}$ ratios in Fig. 9b or $S/N_{peak-free}$ in Fig.10b, divided by $\sqrt{\xi}$.

The covariance with CUO and NUS restricted sampling allows decreasing the experimental time, while keeping nearly the same resolution and increasing the $S/N_{peak-ridge}$ ratio (Fig.9). When possible, this gain in time can be used to accumulate more scans for each t_1 step, while keeping the same global experimental time. This constant-time $S/N_{peak-ridge}$ ratio, normalized with respect to that observed with unrestricted sampling and constant accumulation profile, $\xi = 1$ in Fig.9a, is equal to

the previous $S/N_{peak-ridge}$ ratio obtained for a fixed ξ value, divided by $\sqrt{\xi}$. It is represented in Fig.11a versus ξ in the case of the G50-CUO-COV2D data shown in Fig.9b. In Fig.11b, we have also represented the covariance $S/N_{peak-free}$ ratio versus the ξ sampling saving factor, observed in constant time experiments. One can observe in Fig. 11a that a sampling-saving factor as small as $\xi = 0.23$, gives a sensitivity enhancement of ca. 2.35, with only a very small broadening factor of 3%. This $S/N_{peak-ridge}$ enhancement, which leads to the reduction of experimental time by a factor of 5.5, is much more difficult to obtain with restricted sampled FT2D experiments, even with MaxEnt reconstruction. However, a too small sampling-saving factor may lead to a deteriorative resolution along F_1 in a COV2D spectrum. The sampling-factor effect on the resolution has already been discussed for the square profile, that is, with the decrease of ξ, the resolution deteriorates[36]. In Fig.12 we show a demonstrative example of such an effect for the G60 profile applied to [U-^{13}C]-GB1 protein. The resolution increases with the ξ value, but becomes constant when ca. $\xi \geq 0.5$, as observable along the dashed line (Fig.12).
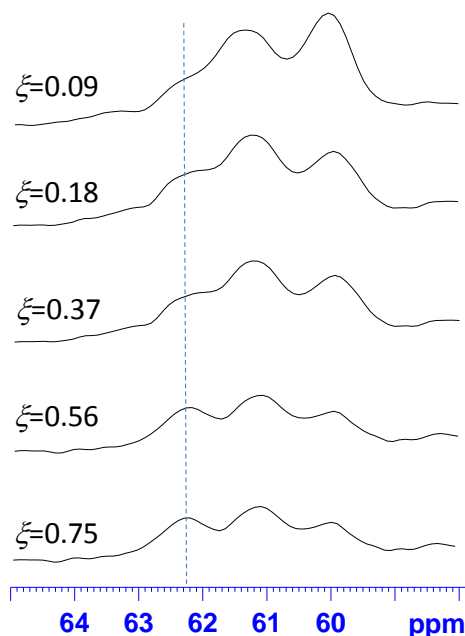

Fig.12 Slices taken at 71.7 ppm in F_2, represented only in between 58-65 ppm along F_1, of ^{13}C 2D DARR spectra of [U-^{13}C]-GB1 protein accumulated and treated with G60-CUO-COV2D, versus the ξ sampling-saving factor. The resolution increases with ξ, but becomes constant when ca. $\xi \geq 0.5$, as observable along the dashed line.

3.2.2.3 Set up of the covariance acquisition

As mentioned before, when increasing ξ, the resolution enhances, but the $S/N_{\text{peak-free}}$ and $S/N_{\text{peak-ridge}}$ ratios of constant-time experiments decrease. Therefore, the experimental optimization mainly consists in determining the sampling-saving factor that gives the best compromise between S/N and the resolution.

Experimentally, the t_1 step value is fixed by the desired spectral-width, $\Delta t_1 = 1/SW_1$, and the maximum number N of t_1 steps by Eq.3. Thus, the acquisition can start with one $G\sigma$ accumulation profile which approaches zero when $k = N$ (e.g. G50 for $N = 160$ and G100 for $N = 320$).

When the sampling-saving factor ξ becomes larger than e.g. 0.2, a covariance treatment is performed after each t_1 step, and this t_1 value can be increased until the resolution along F_1 becomes sufficient. Then, when the S/N ratio is not sufficient, an additional acquisition with the same parameters can be performed. In the case of numerous resonances, such as ^{13}C-^{13}C spectra of proteins, the desired resolution is close to that observed in the 1D spectrum, and a sampling-saving factor of $\xi = 0.3$-0.5 may be required (Fig.12). In the case of a small molecule with resolved resonances, the main purpose of COV2D treatment may be to maximize the S/N, especially in the case of nuclei with very long longitudinal relaxation time, small natural abundance, and/or low gyromagnetic ratio. In this case, a smaller sampling-saving factor may be used (Fig.9-11), and its value depends on the spectral resolution.

3.2.2.4 Application of covariance to [U-^{13}C,^{15}N]-proteo-rhodopsin

Lastly, we show in Fig.13 the comparison of the different covariance schemes applied to [U-^{13}C,^{15}N]-proteo-rhodopsin. According to the required spectral width ($SW_1 = 40$ kHz) and minimum line-width ($\chi_{\text{min}} \approx 280$ Hz), we have used $\Delta t_1 = 25$ µs (Eq.1) and $N = 96$ (Eq.3, $t_{1\text{max,FT}} = 2.4$ ms). The fully-sampled 2D spectra (Fig.13a and d) recorded with these values, show that the Gaussian accumulation profile (Fig.13d),

which emphasizes the small evolution times, leads to much larger signal than uniform square profile (Fig.13a: SQ-COV2D). A sampling-saving factor of $\xi = 0.5$ with $n = 48$ points, was used for other covariance spectra (Figs.13b,c,e,f).
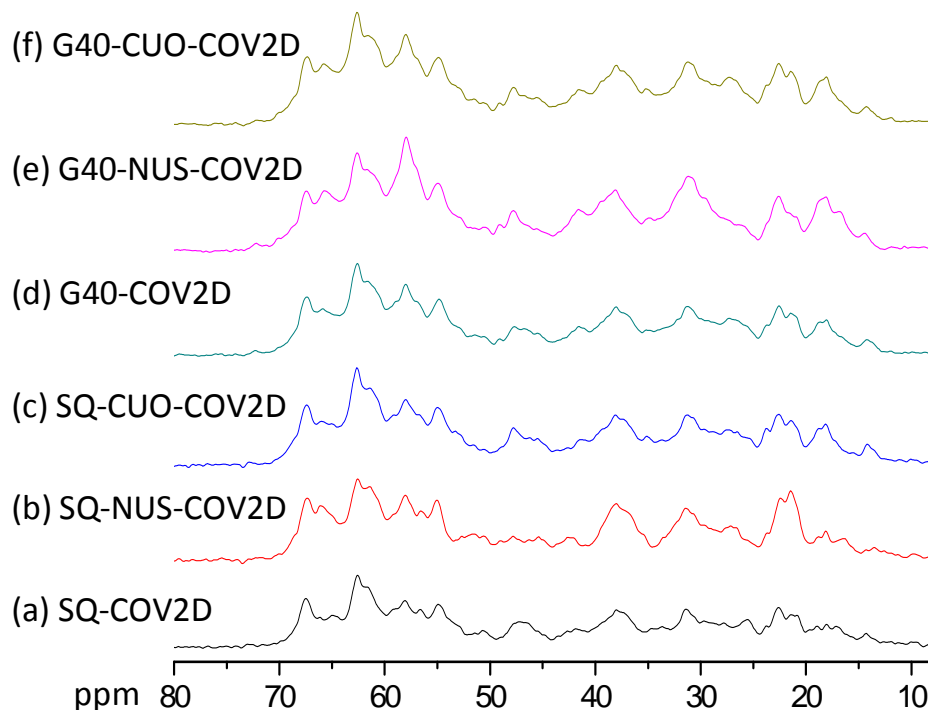

Fig.13 Comparison of 1D slices along $F_2 = 176.5$ ppm of ^{13}C 2D DARR COV2D spectra of [U-^{13}C,^{15}N]-proteo-rhodopsin, with $\tau_{mix} = 30$ ms for short-distance correlations with $M = 128$ and $N = 96$. (a,d) Full sampling ($\xi = 1$), with (a) SQ $\approx$ US-FT2D or (d) G40 profile. (b,c,e,f) Restricted sampling ($n = 48$, $\xi = 0.5$) and thus half experimental time with respect to (a,d), with (b) SQ-NUS, (c) SQ-CUO, (e) G40-NUS, (f) G40-CUO.

It must be first observed that resolutions and signal amplitudes are roughly the same as those observed in Fig. 13a,d, in spite of a decrease of two in experimental time ($\xi = 0.5$). The S/N of G40-CUO-COV2D (Fig. 13f) is roughly 1.12 times of that of G40-NUS-COV2D (Fig.13e), and that of SQ-CUO-COV2D (Fig.13c), roughly 1.18 times of that of SQ-NUS-COV2D (Fig.13b), which is consistent with previous observations. Furthermore, by comparing G40-CUO-COV2D (Fig.13f) with G40-NUS-COV2D (Fig.13e), it is obvious that G40-CUO-COV2D, which uses Gaussian accumulation profile and reduced uniform sampling, and which yields best resolution and S/N, is the best choice. Here it should be pointed out that the peak at 47

ppm of SQ-NUS-COV2D (Fig.13b) is attenuated, which is possibly due to the fact that the NUS sampling rate leads to the cancellation of the signals in covariance treatment, since this peak can be recovered with different sampling-saving factors $\xi = 0.4$ and 0.6. The shoulder of the peak at 47 ppm of G40-NUS-COV2D (Fig.13e) is also attenuated.

3.2.3 Conclusion

A host of methods, such as MaxEnt reconstruction and COV2D, have been proposed to reduce the experimental time of the 2D NMR experiments with reduced number of t_1 points, acquired by NUS or CUO schemes. It is an obvious fact that the early evolution time has more intense signal, however, it is also well known that the most popular method MaxEnt achieves a better S/N with NUS scheme than that with CUO scheme, because MaxEnt method needs some points in the middle and the tail in the t_1 dimension to facilitate the reconstruction of the 2D spectrum. In contrast, we have found that COV2D with CUO sampling presents a better sensitivity than with NUS, implying that the signal corresponding to short evolution times is the most sensitive when introduced in the covariance treatment, without loss of resolution. CUO sampling makes the covariance easy to use in practice, since the number of t_1 points can easily be optimized 'on the fly' to obtain the desired resolution along F_1. This resolution must be the best in the case of very crowded 1D spectrum (e.g. proteins), whereas it can be decreased to maximize the S/N ratio in the case of resolved 1D spectrum.

We demonstrate that these two restricted sampling schemes can also be combined in covariance spectroscopy with weighted acquisition strategy with different accumulation profiles to further enhance the S/N of NMR spectra. We show that, with respect to the constant accumulation profile, a better S/N ratio is obtained with the Gaussian accumulation profile.

We also demonstrate that the CUO sampling with sampling-saving factor of $\xi \approx$ 0.3, simultaneously with the Gaussian-50 accumulation profile, leads to good S/N, enhanced by a factor of 2.3 with respect to the conventional FT2D method, together with good resolution. We have demonstrated these results on ^{13}C-^{13}C correlation experiments of U-^{13}C labeled bio-molecules of L-histidine·HCl·H$_2$O model samples and the proteo-rhodopsin membrane protein. Therefore, with the Gaussian profile and CUO-COV2D method, we were able to reduce the number of increments in t_1 by a factor of ca. 6~12. Here we should emphasize that this argument is only valid with exponentially decaying 2D signals, and not in the case of sine/cosine modulated or constant-time signals. Overall, this combination of Gaussian accumulation profile and CUO sampling in covariance spectroscopy should become valuable in applications for the sensitivity-limited solid state NMR experiments.

References

[1] W. Qiang, *J. Magn.Reson.*, **213,** 171–175 (2011).

[2] A. Kumar, S.C. Brown, M.E. Donlan, B.U. Meier, P.W. Jeffs, *J. Magn. Reson.*, **95**, 1–9 (1991).

[3] D. Rovnyak, M. Sarcone, Z. Jiang, *Magn. Reson. Chem.*, 49, 483–491 (2011).

[4] J.C.J. Barna, E.D. Laue, M.R. Mayger, J. Skilling, S.J.P. Worrall, *J. Magn. Reson.*, **73**, 69–77 (1987) (1969).

[5] K. Kazimierczuk, A. Zawadzka, W. Koz′min′ ski, I. Zhukov, *J. Magn. Reson.*, **188**, 344–356 (2007).

[6] R. Bruschweiler, F. Zhang, *J. Chem. Phys.*, **120**, 5253‑5260 (2004).

[7] R. Bruschweiler, *J. Chem. Phys.*, **121**, 409 (2004).

[8] B.W. Hu, P. Zhou, I. Noda, G.Z. Zhao, *Anal. Chem.*, **77**, 7534 (2005).

[9] M. Weingarth, P. Tekely, R. Brüschweiler, G. Bodenhausen, *Chem. Commun.*, **46**, 952‑954 (2010).

[10] J. Yang, L. Aslimovska, C. Glaubitz, *J. Am. Chem. Soc.*, **133**, 4874-4881 (2011).

[11] J.M. Walter, D. Greenfield, C. Bustamante, J. Liphardt, *Proc. Natl. Acad. Sci. USA,* **104**, 2408‑2412 (2007).

[12] A.E. Bennett, C.M. Rienstra, M. Auger, K.V. Lakshmi, R.G. Griffin, *J. Chem. Phys.*, **103**, 6951‑6958 (1995).

[13] B. Hu, O. Lafon, J. Trébos, Q. Chen, J.-P. Amoureux, *J. Magn. Reson.*, **212**, 320‑329 (2011).

[14] B.M. Fung, A.K. Khitrin, K. Ermolaev, *J. Magn. Reson.*, **142**, 97‑101 (2000).

[15] K. Takegoshi, S. Nakamura, T. Terao, *Chem. Phys. Lett.*, **344**, 631‑637 (2001).

[16] K. Takegoshi, S. Nakamura, T. Terao, *J.Chem. Phys.* **118**, 2325‑2341 (2003).

[17] L. Duma, D. Abergel, F. Ferrage, P. Pelupessy, P. Tekely, G. Bodenhausen, *Chem. Phys. Chem.*, **9**, 1104‑1106 (2008).

[18] M. Weingarth, G. Bodenhausen, P. Tekely, *Chem. Phys. Lett.*, **488**, 10‑16 (2010).

[19] M. Weingarth, D.E. Demco, G. Bodenhausen, P. Tekely, *Chem. Phys. Lett.*, **469**, 342‑348 (2009).

[20] M. Weingarth, G. Bodenhausen, P. Tekely, *J. Am. Chem.Soc.*, **131**, 13937‑13939 (2009).

[21] D.A. Snyder, A. Ghosh, F. Zhang, T. Szyperski, R. Brüschweiler, *J. Chem. Phys.*, **129**, 104511 (2008).

[22] B. Hu, J.P. Amoureux, J. Trébosc, M. Deschamps, G. Tricot, *J. Chem Phys.*, **128**, 134502 (2008).

[23] Y. Chen, F. Zhang, W. Bermel, R. Brüschweiler, *J. Am. Chem. Soc.*, **128**, 15564‑15565 (2006).

[24] T. Szyperski, G. Wider, J. Bushweller and K. Wuthrich, *J. Am. Chem. Soc.*, **115**, 9307–9308 (1993).

[25] S. Kim and T. Szyperski, *J. Am. Chem. Soc*, **125**, 1385–1393 (2003).

[26] E. Kupce and R. Freeman, *J. Am. Chem. Soc*, **125**, 13958–13959 (2003).

[27] H. Hu, A. De Angelis, V. Mandelshtam and A. Shaka, *J. Magn. Reson.*, **144**, 357–366 (2000).

[28] J. C. J. Barna, E. D. Laue, M. R. Mayger, J. Skilling and S. J. P. Worrall, *J. Magn. Reson.*, **73**, 69–77 (1969) (1987).

[29] J. Hoch and A. Stern, *Methods Enzymol.*, **338**, 159–178 (2002).

[30] G. Bretthorst, *J. Magn. Reson.*, **88**, 533–551 (1990).

[31] R. Chylla and J. Markley, *J. Biomol. NMR*, **5**, 245–258 (1995).

[32] V. Y. Orekhov, I. Ibraghimov and M. Billeter, *J. Biomol. NMR*, **27**, 165-173 (2003).

[33] T. Luan, V. Jaravine, A. Yee, C. H. Arrowsmith and V. Y. Orekhov, *J. Biomol. NMR*, **33**, 1-14 (2005).

[34] R. Bruschweiler and F. Zhang, *Journal of Chemical Physics*, **120**, 5253-5260 (2004).

[35] R. Bruschweiler, *Journal of Chemical Physics*, **121**, 409 (2004).

[36] B. W. Hu, P. Zhou, I. Noda and G. Z. Zhao, *Analytical Chemistry*, **77**, 7534   (2005).

[37] K. Kazimierczuk, W. Kozminski and I. Zhukov, *J. Magn. Reson.*, **179**, 323–328 (2006).

[38] J. Stanek and W. Kozminski, *J. Biomol. NMR*, **47**, 65-77 (2010).

[39] P. Schmieder, A. Stern, G. Wagner and J. Hoch, *J. Biomol. NMR*, **3**, 569–576 (1993).

[40] P. Schmieder, A. Stern, G. Wagner and J. Hoch, *J. Biomol. NMR*, **4**, 483–490 (1994).

[41] M. W. Maciejewski, M. Mobli, A. D. Schuyler, Alan S. Stern and J. C. Hoch, *Top. Curr. Chem.* , **316**, 49–78 (2012).

[42] O. Lafon, B. Hu, J.-P. Amoureux and P. Lesot, *Chem. Eur. J.*, **17** 6716 – 6724 (2011).

[43] B. Hu, J. P. Amoureux, J. Trébosc, M. Deschamps and G. Tricot, *J. Chem. Phys.*, **128**, 134502 (2008).

[44] M. Weingarth, P. Tekely, R. Brüschweiler and G. Bodenhausen, *Chem. Commun.*, **46**, 952-954 (2010).

[45] J.C.J.Barna, E.D.Laue, M.R.Mayger, *J. Magn. Reson.*, **73**, 69–77 (1987)

[46] N. Trbovic, S. Smirnov, F. Zhang and R. Bruschweiler, *J. Magn. Reson.*, **171**, 277 (2004).

[47] B. Hu, J. P. Amoureux and J. Trébosc, *Solid State Nuclear Magnetic Resonance*, **31**, 163 (2007).

[48] R. R. Ernst, G. Bodenhausen and A. Wokaun, *Principles of Nuclear Magnetic Resonance in One and Two Dimensions*, Oxford University Press, 1990.

[49] D. A. Snyder, A. Ghosh, F. Zhang, T. Szyperski and R. Brüschweiler, *J. Chem. Phys.*, **129**, 104511 (2008)

Resume

My Ph.D. researches focus on the development of novel Solid-State Nuclear Magnetic Resonance (SS-NMR) methods. The proposed methods are compatible with high magnetic fields and fast MAS. Main achievements comprise:

(1) the new pulse sequence (PT-HMQC) for heteronucler experiments. The major limitation of HMQC experiments is their lack of sensitivity, especially involving quadrupolar nuclei with short T_2 values. We propose a simple and robust strategy by manipulating the populations of the satellite transitions (ST) during the mixing time, to accelerate the rate of coherence transfer, and enhance the sensitivity of *J*-HMQC experiments with indirect detection of the quadrupolar nucleus. With the introduction of new shape pulses (quadruple sweeps pulses), we find the best method, PT-*J*-HMQC with QFS (Quadruple Frequency Sweep), which is more robust to samples with different sites with different C_Q value.

(2) the new data processing methods for homonuclear experiments. We combine covariance (COV2D) spectroscopy with non-uniform continuous acquisition (NUCA) scheme, such as linear profile (L_k) and Gaussian profile (G_k). Furthermore, we add various sampling schemes, such as NUS (non-uniform sampling) and CUO (t_1 cut-off). We find that covariance treatment, combined with the CUO sampling and Gaussian accumulation profile provides better gain in experimental time, better *S/N*, without loss of resolution.

Paper List

Yixuan LI was born in Jilin, China. She has received her BSc degree in physics at East China Normal University in 2010. She joined Shanghai Key Laboratory of Magnetic Resonance at the same university in the same year，and Unit of Catalysis and Chemistry of Solids at University of Lille 1 in 2012. Her research aims on new methods for Solid State NMR

[1] Y. Li, Q. Wang[*], Z. Zhang, J. Yang, B. Hu[*], Q. Chen, I. Noda, F. Deng[*], Covariance spectroscopy with a non-uniform and consecutive acquisition scheme for signal enhancement of the NMR experiments, Journal of Magnetic Resonance, 217 (2012) 106–111.

[2] Y. Li, B. Hu[*], Q. Chen, Q. Wang[*], Z. Zhang, J. Yang, I. Noda, J. Trébosc, Oliver Lafon, J. Amoureux and F. Deng[*], Comparison of various sampling schemes and accumulation profiles in covariance spectroscopy with exponentially decaying 2D signals, Analyst, 138 (2013), 2411-2419.

[3] Q. Wang, J. Trébosc, Y. Li, J. Xu, B. Hu, N. Feng, Q. Chen, O. Lafon, J. Amoureux and F. Deng[*], Signal enhancement of J-HMQC experiments in solid-state NMR involving half-integer quadrupolar nuclei, Chem. Commun, 49 (2013) 6653-6655.

[4] Q. Wang, Y. Li, J. Trébosc, O. Lafon, J. Xu, B. Hu, N. Feng, Q. Chen, J. Amoureux[*], and F. Deng[*], Population Transfer HMQC for quadrupolar nucle, Journal of Chemical Physics, 142(2015), 094201.

Resumé

Mon travail de thèse a porté sur le développement de nouvelles méthodes de Résonance Magnétique Nucléaire pour l'étude des solides. Les méthodes développées sont compatibles avec des champs magnétiques élevés et une rotation rapide de l'échantillon autour de l'angle magique. Nous avons notamment développé une nouvelle méthode pour observer les proximités hétéronucléaires dans les solides. Cette méthode, baptisée PT-HMQC, consiste à manipuler les populations des transitions satellites des noyaux quadripolaires pendant les temps de défocalisation et de refocalisation. Cette manipulation permet d'accélérer le transfert de cohérence hétéronucléaire et ainsi d'augmenter la sensibilité des méthodes HMQC permettant l'observation indirecte d'isotope quadripolaire. Pour manipuler les transitions satellite, nous avons introduit de nouvelles impulsions radiofréquence modulées en amplitude et en fréquence. Ces impulsions, qui réalisent un quadruple balayage en fréquence, sont plus robustes dans le cas d'échantillon contenant des sites soumis à des interactions quadripolaires différentes. Nous avons aussi introduit une nouvelle méthode pour l'acquisition et le traitement des expériences RMN bidimensionnelles. Nous avons montré que la covariance permet de traiter des expériences enregistrées avec une acquisition continue non-uniforme. Ces méthodes permettent de réduire le temps d'expérience et d'améliorer la sensibilité sans affecter la résolution.

This thesis focuses on the development of novel Solid-State Nuclear Magnetic Resonance (SS-NMR) methods. The proposed methods are compatible with high magnetic fields and fast MAS. Main achievements comprise:

(1) the new pulse sequence (PT-HMQC) for heteronucler experiments. The major limitation of HMQC experiments is their lack of sensitivity, especially involving quadrupolar nuclei with short T2 values. We propose a simple and robust strategy by manipulating the populations of the satellite transitions (ST) during the mixing time, to accelerate the rate of coherence transfer, and enhance the sensitivity of J-HMQC experiments with indirect detection of the quadrupolar nucleus. With the introduction of new shape pulses (quadruple sweeps pulses), we find the best method, PT-J-HMQC with QFS (Quadruple Frequency Sweep), which is more robust to samples with different sites with different C_Q value.

(2) the new data processing methods for homonuclear experiments. We combine covariance (COV2D) spectroscopy with non-uniform continuous acquisition (NUCA) scheme, such as linear profile (L_k) and Gaussian profile (G_k). Furthermore, we add various sampling schemes, such as NUS (non-uniform sampling) and CUO (t_1 cut-off). We find that covariance treatment, combined with the CUO sampling and Gaussian accumulation profile provides better gain in experimental time, better S/N, without loss of resolution.